ISSN 1854-0171

ACTA GEOTECHNICA SLOVENICA

2016/1
VOL. 13

ISSN: 1854-0171

ACTA GEOTECHNICA SLOVENICA

Ustanovitelji | Founders

Univerza v Mariboru, Fakulteta za gradbeništvo, prometno inženirstvo in arhitekturo
University of Maribor, Faculty of Civil Engineering, Transportation Engineering and Architecture

Univerza v Ljubljani, Fakulteta za gradbeništvo in geodezijo
University of Ljubljana, Faculty of Civil and Geodetic Engineering

Univerza v Ljubljani, Naravoslovnotehniška fakulteta
University of Ljubljana, Faculty of Natural Sciences and Engineering

Slovensko geotehniško društvo
Slovenian Geotechnical Society

Društvo za podzemne in geotehniške konstrukcije
Society for Underground and Geotechnical Constructions

Izdajatelj | Publisher

Univerza v Mariboru, Fakulteta za gradbeništvo, prometno inženirstvo in arhitekturo
Faculty of Civil Engineering, Transportation Engineering and Architecture

Odgovorni urednik | Editor–in–Chief

Bojana Dolinar — University of Maribor

Uredniki | Co–Editors

Jakob Likar	University of Ljubljana
Janko Logar	University of Ljubljana
Borut Macuh	University of Maribor
Stanislav Škrabl	University of Maribor
Bojan Žlender	University of Maribor

Posvetovalni uredniki | Advisory Editors

Heinz Brandl	Vienna University of Technology
Chandrakant. S. Desai	University of Arizona
Pedro Seco e Pinto	National Laboratory of Civil Eng.

Lektor | Proof–Reader

Paul McGuiness

Naklada | Circulation

200 izvodov - issues

Cena | Price

25 EUR/letnik - 25 EUR/vol.; (50 EUR for institutions/za institucije)

Tisk | Print

Rolgraf d.o.o.

Revija redno izhaja dvakrat letno. Članki v reviji so recenzirani s strani priznanih mednarodnih strokovnjakov. Baze podatkov v katerih je revija indeksirana: SCIE - Science Citation Index Expanded, JCR – Journal Citation Reports / Science Edition, ICONDA - The international Construction database, GeoRef. Izid publikacije je finančno podprla Javna agencija za raziskovalno dejavnost Republike Slovenije iz naslova razpisa za sofinanciranje domačih periodičnih publikacij.

Naslov uredništva | Address

ACTA GEOTECHNICA SLOVENICA
Univerza v Mariboru, Fakulteta za gradbeništvo, prometno inženirstvo in arhitekturo
Smetanova ulica 17, 2000 Maribor, Slovenija
Telefon / Telephone: +386 (0)2 22 94 300
Faks / Fax: +386 (0)2 25 24 179
E-pošta / E-mail: ags@uni-mb.si

Spletni naslov | web Address

http://www.fg.uni-mb.si/journal-ags/

The journal is published twice a year. Papers are peer reviewed by renowned international experts. Indexation data bases of the journal: SCIE - Science Citation Index Expanded, JCR – Journal Citation Reports / Science Edition, ICONDA- The international Construction database, GeoRef. The publication was financially supported by Slovenian Research Agency according to the Tender for co-financing of domestic periodicals.

EMPIRIČNA KORELACIJA MED HITROSTJO STRIŽNEGA VALOVANJA IN DINAMIČNIM PENETRACIJSKEM PREIZKUSOM: ŠTUDIJA PRIMERA, VARAŽDIN, HRVAŠKA

Stjepan Strelec *(vodilni avtor)*
University of Zagreb,
Faculty of Geotechnical Engineering
Hallerova aleja 7, HR - 42000, Varaždin, Hrvaška
E-pošta: stjepan.strelec@gmail.com

Davor Stanko
University of Zagreb,
Faculty of Geotechnical Engineering
Hallerova aleja 7, HR - 42000, Varaždin, Hrvaška
E-pošta: stankodavor@gmail.com

Mario Gazdek
University of Zagreb,
Faculty of Geotechnical Engineering
Hallerova aleja 7, HR - 42000, Varaždin, Hrvaška
E-pošta: mario.gazdek@gmail.com

Ključne besede

hitrost strižnega valovanja, MASW, DPH, empirične korelacije, dinamični elastični moduli, dinamične lastnosti tal

Izvleček

Varaždin se nahaja v severozahodnem delu Hrvaške na mestu plitvih kvartarnih aluvialnih sedimentov reke Drave. Aluvialni mehki sedimenti lahko igrajo ključno vlogo pri ojačanju gibanja potresnih valov v tleh. Hitrost strižnega valovanja (V_S) je eden izmed najbolj pomembnih parametrov za določanje dinamičnih lastnosti tal in analizo odziva tal.

Metoda seizmičnega površinskega valovanja (MASW) je najenostavnejši in zelo učinkovit način za merjenje hitrosti strižnega valovanja na terenu. Dinamični penetracijski preizkus (DPH) je primeren za določanje parametrov trdnosti in deformacijskih lastnosti tal. V literaturi manjkajo korelacije med hitrostmi strižnega valovanja in preizkusi DPH (V_S - N_{DPH}). V tem prispevku predstavljamo empirične korelacije med hitrostmi strižnega valovanja V_S in penetracijskim odporom N_{DPH} za: a) neobdelane (originalne) N_{DPH} podatke: $V_S = 97.839 \cdot N_{DPH}^{0.395}$, ($R^2 = 0.723$); b) podatke N_{DPH} s korekcijo za talno vodo: $V_S = 92.998 \cdot N_{DPH}^{0.363}$ ($R^2 = 0.815$). Iz izmerjenih podatkov DPH so bili ocenjeni hitrost strižnega valovanja (VS), strižni modul (Go) in Youngova modula (Eo in Er). Primerjali smo dva različna pristopa (za majhno in veliko deformacijo), iz rezultatov pa smo ugotovili, da se dobro ujemajo, ko je relativna razlika med hitrostmi majhna in gladka.

Dinamični penetracijski preizkusi so dobri za preučevanje točno določene točke v velikem polju območja, ki temelji na predhodnih seizmičnih preizkusih. Predlagana korelacija V_S - N_{DPH} se lahko uporablja za grobo oceno V_S iz N_{DPH} (vrednosti so specifične za prikazano lokacijo, zato se ne morejo uporabljati splošno). Na ta način so lahko pridobljene koristne informacije o dinamičnih lastnostih tal za analizo odziva tal in študij lokalnih vplivov.

EMPIRICAL CORRELATION BETWEEN THE SHEAR-WAVE VELOCITY AND THE DYNAMIC PROBING HEAVY TEST: CASE STUDY, VARAŽDIN, CROATIA

Stjepan Strelec *(corresponding author)*
University of Zagreb,
Faculty of Geotechnical Engineering
Hallerova aleja 7, HR - 42000, Varaždin, Croatia
E-mail: stjepan.strelec@gmail.com

Davor Stanko
University of Zagreb,
Faculty of Geotechnical Engineering
Hallerova aleja 7, HR - 42000, Varaždin, Croatia
E-mail: stankodavor@gmail.com

Mario Gazdek
University of Zagreb,
Faculty of Geotechnical Engineering
Hallerova aleja 7, HR - 42000, Varaždin, Croatia
E-mail: mario.gazdek@gmail.com

Keywords

shear-wave velocity, MASW, DPH, empirical correlations, dynamic elastic moduli, dynamic soil properties

Abstract

Varaždin is located in the north-western part of Croatia in shallow quaternary alluvial sediments of the Drava River basin. Local site effects due to the alluvial soft sediments can play a crucial role in the amplification of seismic-wave ground motions. The shear-wave velocity (V_S) is one of the most important parameters for determining dynamic soil properties and ground-response analyses.

The seismic surface wave method (MASW) is the simplest and a very efficient way of measuring the shear-wave velocity in the field. The Dynamic Probing Heavy (DPH) test is suited to determining the soil strength and the soil deformation properties. However, there are a lack of correlations between the shear-wave velocity and the DPH tests (V_S - N_{DPH}) in the literature. In this paper we present empirical correlations between the shear-wave velocity V_S and the soil penetration resistance N_{DPH} with: a) raw (original) N_{DPH} data: $V_S = 97.839 \cdot N_{DPH}^{0.395}$, ($R^2 = 0.723$); b) a groundwater correction N_{DPH} data: $V_S = 92.998 \cdot N_{DPH}^{0.363}$ ($R^2 = 0.815$). From the measured DPH data, the shear-wave velocity (V_S), the shear modulus (Go) and the Young's modulus (Eo and Er) were estimated. Two different approaches (low vs. high strain) were compared, and the results were found to be in good agreement when the relative difference between the velocities is small and smooth.

Dynamic probing tests are good for studying a discrete point of interest in a large field area based on preliminary seismic tests. The suggested correlation V_S - N_{DPH} can be used for a rough estimation of V_S from N_{DPH} (they are site-specific, and so not applicable worldwide). In this way valuable information about dynamic soil properties can be extracted for ground-response analyses and the study of local site effects.

1 INTRODUCTION

The influence of local geological and soil conditions on the intensity of ground shaking and earthquake damage has been known for many years. Local site effects play an important role in earthquake-resistant design and must be accounted for case by case. Ground-response analyses are used to predict ground-surface motions for the development of design spectra, and to evaluate dynamic stresses and strains for the determination of earthquake-induced forces. For many important problems, particularly those dominated by wave-propagation effects, low-level strains are induced into the soil, but when concerned with the stability of masses of soil, large strains are induced in the soil [1, 2, 3].

There are many V_S - N_{SPT} correlations in the literature, as shown by Hanumantharao and Ramana [4], Marto, Soon and Kasim [5], Jafari et al. [6], Uma Maheswari et al. [7], Kuo et al. [8], Akin et al. [9] and Anbahzgan et al. [10]. However, there is a lack of information regarding the existence of correlations when taking a combined approach to the shear-wave velocity and Dynamic Probing Heavy tests (V_S - N_{DPH}). Iyisan [11] presented correlations between the shear-wave velocity and different in-situ probing tests (Standard Penetration Test - SPT, Dynamic Probe Heavy - DPH, Cone Penetration Test - CPT). In his research, he mentioned V_S - N_{DPH} correlations for all soils according to the empirical equation: V_S=86.4·$N_{DPH}^{0.367}$, with R^2=0.7. It was stated that such correlations, although developed for particular types of soil, could be applicable worldwide, but were actually found to be site-specific due to a number of factors pertaining to local soils (particle distribution, plasticity, soil texture, etc.) and thus should be used with caution. Given V_S - N_{DPH} correlations should not be thought of as a substitute for seismic (geophysical) measurements, they can be useful for verifying the measured values of the shear-wave velocity V_S or in supplementing seismic (geophysical) testing due to some impossibilities (space constraints, structure of terrain, environmental noise, etc.).

In this paper we present statistical empirical correlations between the shear-wave velocity V_S (geophysical seismic surface MASW method at low strains γ_S~10^{-6}, Fig. 1) and the soil penetration resistance N_{DPH} (Dynamic Probing Heavy test DPH at high strains γ_S~10^{-1}, Fig. 1), in shallow quaternary alluvial sediments for a local geological site-specific case study at four locations in Varaždin using the power-law relation:

$$V_S = A \cdot N_{DPH}^{\ B} \qquad (1)$$

From measured DPH data, the shear-wave velocity (V_S), the shear modulus (G_{MAX} or *Go*) and the Young's modulus (*Eo* and *Er*) were estimated.

The main aim of this paper is not to give an empirical correlation between V_S - N_{DPH} as a substitute for seismic measurements, but to show a reliable way of comparing two different experimental approaches at low strain vs. high strain for the determination of site-specific dynamic soil properties. The suggested correlation between V_S and N_{DPH} can be used to make rough estimates of V_S from N_{DPH} (they are site-specific, and so not applicable worldwide), particularly for preliminary studies and/or non-critical projects that are under consideration.

2 DYNAMIC SOIL PROPERTIES

A medium is said to be elastic if it possesses a natural state (strains and stresses are at zero) to which it will revert to when applied forces are removed. Under the influence of applied loads, the stress and strain will change together, and the relation between them, known as the constitutive relation, is an important characteristic of the medium [13].

A determination of the dynamic soil properties is a critical task in any solution of geotechnical earthquake-engineering problems. The selection of testing techniques for the measurement of dynamic soil properties requires a careful consideration and understanding of the specific

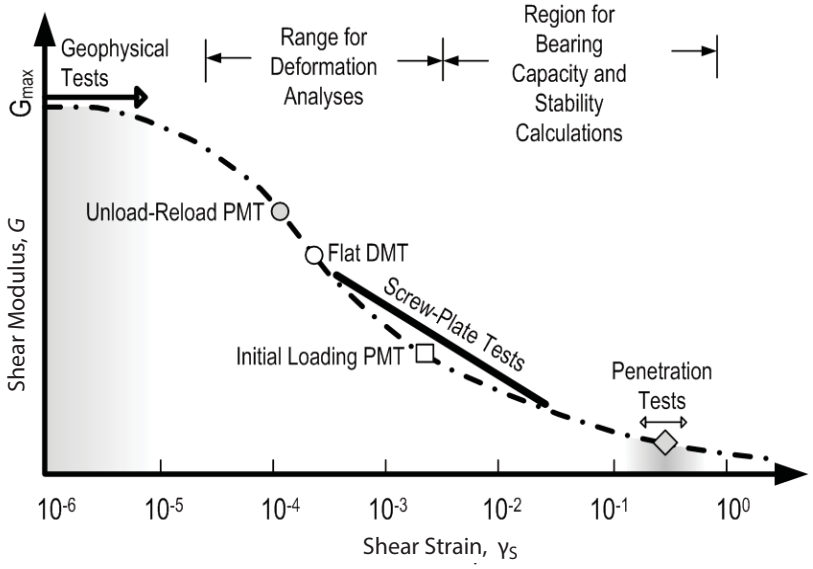

Figure 1. The starting point of the stress-strain curve (at low strain γ_S~10^{-6}) can be accurately established from seismic tests and its end point (at high strain γ_S~10^{-1}) by dynamic tests [12].

problem at hand. Low strain tests generally operate at strain levels that are not large enough to induce significant nonlinear stress-strain behaviour in the soil (below $\gamma_S<10^{-3}$) and are based on the theory of wave propagation in the material. High-strain tests are used to measure the high-strain characteristics of soils (elastoplastic behavior), such as soil strength and soil deformation during irrecoverable deformations in the soil [1].

The dynamic modulus is the ratio of stress to strain under vibratory conditions (calculated from data obtained from either free- or forced-vibration tests, in shear, compression or elongation), the so-called low-strain modulus. The shear modulus describes the material's response to shear stress. Most seismic geophysical tests induce low shear strains and the measured shear-wave velocity V_S can be used to compute the maximum dynamic shear modulus or stiffness of the soil G_{MAX} or *Go* with a knowledge of the soil density ρ [1, 13, 14, 15]:

$$Go = \rho \cdot V_S^2 \qquad (2)$$

The soil density ρ can be evaluated from the measured shear-wave velocity V_S and the depth h [12]:

$$\rho = 0.85 \cdot \log(V_S) - 0.16 \cdot \log(h) \qquad (3)$$

A small strain shear modulus is the key benchmark and establishes the highest, achievable soil stiffness that other moduli can be compared to on a relative basis.

The Young's modulus *Eo* describes the material's response to linear stress. Its relation to the shear modulus *Go* is defined as:

$$Eo = 2 \cdot Go(1+\upsilon) \qquad (4)$$

where υ is the Poisson's coefficient.

With *Go* and *Eo* being operable at non-destructive small strains and a shear strength τ_{MAX} at failure strains, it is possible to relate small - high strain modulus (two opposite ends of the strain spectrum). For monotonic static loading a modified degradation hyperbola (Fig. 1) relates the normalized shear modulus *G*/*Go* and the normalized Young's modulus *E*/*Eo* to the mobilized shear stress τ/τ_{MAX} in the form [12]:

$$\frac{G}{Go} = 1 - f\left(\frac{\tau}{\tau_{MAX}}\right)^q \qquad (5)$$

or for the Young's modulus:

$$\frac{E}{Eo} = 1 - f\left(\frac{\tau}{\tau_{MAX}}\right)^q \qquad (6)$$

where *f* and *q* are empirical parameters controlling the rate of modulus decay (Fig. 1). For practical problems, the mobilized shear stress can be considered as the reciprocal of FS (factor of safety). Burns and Mayne [16] found that $f = 1$ and $q = 0.3$ provide reasonable first-guess values for the degradation parameters in non-structured and non-cemented soils. The Young's modulus *E* in Eq.6 is used in deformation analyses as a reference modulus of elasticity ($E = Er$) because it is directly dependent on the implemented stress and failure stress.

The shear-wave velocity V_S is one of the most important parameters for the determination of the dynamic soil properties and ground-response analyses. Seismic geophysical methods are effective in preliminary field tests since they can cover large volumes of soil at low strains. To induce soil deformation similar to that induced by an earthquake, dynamic probing tests are suited to studying a discrete point of interest in a large field area based on preliminary seismic tests. In this way very useful information about dynamic soil properties can be extracted for further ground-response analyses and the study of local site effects.

The measured dynamic soil properties (V_S, *Go*, *Eo*, *Er*) can be used for the seismic design of structures based on Eurocode 8 - EC8 [17, 18, 19], site response studies [2] and settlement analyses. In a liquefaction assessment, V_S is also widely used [1].

3 FIELD MEASUREMENTS

Field measurements were carried out at four test locations in and nearby Varaždin (Fig. 2, marked with a black circle). The geophysical seismic surface method MASW (Multichannel Analysis of Surface Waves) was used to obtain the shear-wave velocity (V_S) and in-situ dynamic probing tests DPH (Dynamic Probe Heavy) were used to obtain the penetration resistance of the soil (N_{DPH}).

3.1 Geological setting

Varaždin is a baroque city located in the NW part of Croatia in shallow quaternary alluvial sediments of the Drava River basin. In this seismic zone there have been a couple of strong earthquakes in the past. The archives mention a strong earthquake in 1459, with its epicentre near Varaždin ($I_0 = IX^o$ *MCS*). The largest earthquake in modern times occurred in 1982 beneath the Ivančica Mt. ($M_L = 4.7$, $I_0 = VII^o$ *MCS*), and there were also a number of smaller-intensity events in the past according to [20].

The geological characteristics of the Varaždin area are quaternary alluvial soft sediments of the Drava river basin (Fig. 2). It was formed during the Pleistocene and

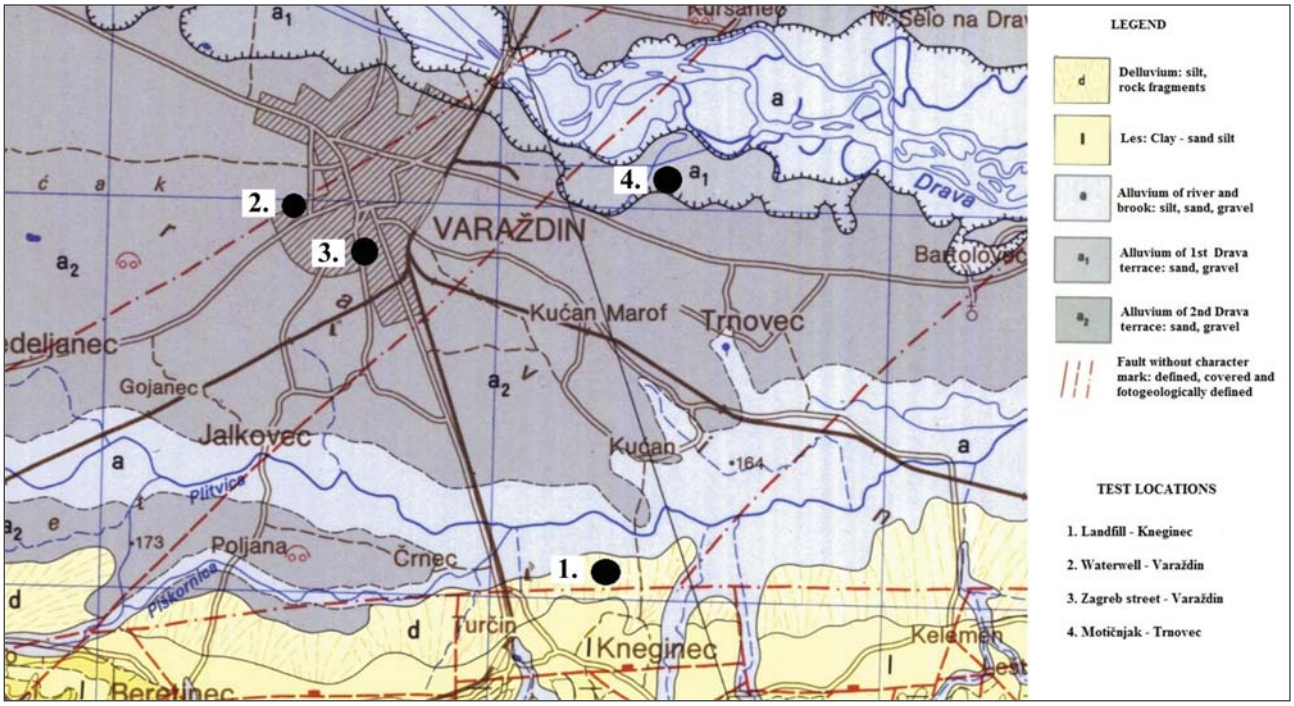

Figure 2. Geology (Quaternary: Pleistocene and Holocene) of Varaždin region at four test locations (1. Landfill - Kneginec, 2. Water well - Varaždin, 3. Zagreb street - Varaždin, 4. Biogas facility Motičnjak - Trnovec)[21].

Holocene as a result of the accumulation processes of the Drava river, as mentioned by Prelogović [21]. It is composed of gravel and sand with variable portions of silt and clay [22, 23, 24]. The thickness of the sand-gravel deposits in the NW area are less than 5 metres, gradually increasing in the downstream direction (WE) to reach more than 60 metres thick in the eastern part. The water table is relatively high at 2–6 m. The general groundwater flow direction is NW–SE and is parallel to the Drava river. The basin is cut by several faults in an SW direction towards the Ivančica Mt. and a WE direction parallel to the Drava River.

3.2 Multichannel analysis of surface waves

Spectral Analysis of Surface Waves (SASW) was introduced in the early 1980s by Nazarian and Stokoe [25, 26, 27] to make use of the spectral analysis of surface waves generated from an impact source like a hammer on a surface. It is used for shallow, shear-wave velocity characterization in which only two receivers (geophone) are used and the spacing between the receiver and the source is changed many times to cover the desired range of the investigation depth. Since this repetition takes several hours, the Multichannel Analysis of Surface Waves by Park et al. [28] and Xia et al. [29] was introduced.

The Multichannel Analysis of Surface Waves (MASW) is a non-destructive seismic method used to evaluate the material layer thickness, the shear-wave velocity V_S (1D or 2D profile with depth), the Poisson's ratio and the soil density [28, 29, 30, 31, 32, 33, 34]. This method is fast and simple because of the strong nature of the surface wave (Rayleigh waves) energy that can be generated by a simple impact source (e.g., a sledgehammer) and the entire range of the investigation depth can be covered with multiple receivers (geophones) without the need to change the receiver's configuration [28, 29, 30, 31, 32, 33, 34]. A schematic diagram of an active MASW field survey is shown in Fig. 3. The MASW profile consist of 24 geophones with a natural frequency of 4.5 Hz in a linear array (69 m spread length, 3 m spacing and 6 m offset), a sledgehammer of 10 kg, a hammer metal plate, and a 24-channel Geode seismograph with supporting software for the data acquisition. The maximum investigation depth (z_{max}) depends on the length of the geophone spread (D) and the source impact energy, while the resolution depends on the minimum geophone spacing (dx).

The data analysis of the captured surface waves (Rayleigh waves) created by the sledgehammer impact on the metal plate was analysed using SeisImager (OYO Corp.) and SurfSeis (Kansas Geological Survey) software packages to obtain a 1D and 2D shear-wave velocity profile with depth. The data analysis consisted of three

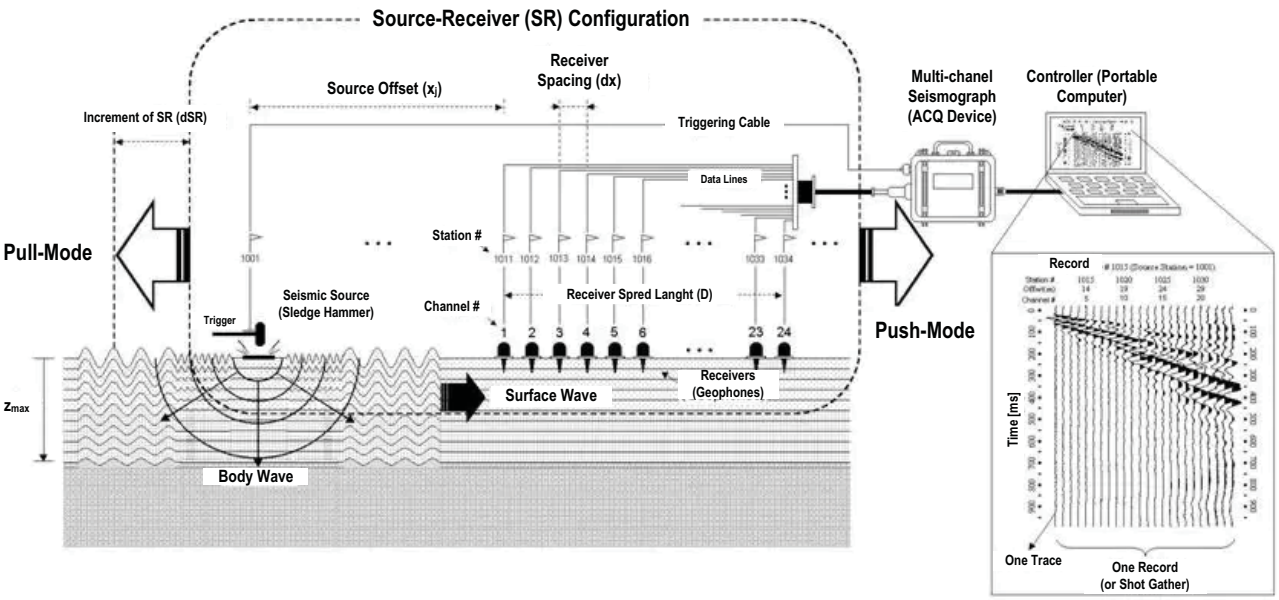

Figure 3. Schematic diagram of active MASW field survey data acquisition [34].

steps: 1) preparation of a MASW record (field file or shot gather), 2) dispersion analysis of Rayleigh waves - fundamental mode and 3) inversion for V_S profiles [28, 29, 30, 31, 32, 33, 34].

The 1D soil profiles for all the test locations obtained from the MASW are shown in Fig. 4., and the 2D profiles are shown in Fig. 5 for the test locations 2.Water well - Varaždin and 4. Motičnjak - Trnovec. The top first layer in all four locations consists of clay having a V_S range of 110–170 m/s from 0 up to 4 m in depth. The second layer consists of sand having a V_S range of 190–260 m/s from 0 up to 9 m depth. The third layer consists of gravel having a V_S range of 270–400 m/s from 5 up to 20 m and above depth. The maximum investigation depth was cut to 20 m for the V_S - N_{DPH} correlation analysis.

Based on the EC8 classification of subsoil classes according to Table 3.1 [17, 18, 19] all the investigated area can be classified as ground type C ($V_{S,30}$ = 180-360 m/s) (Fig. 4).

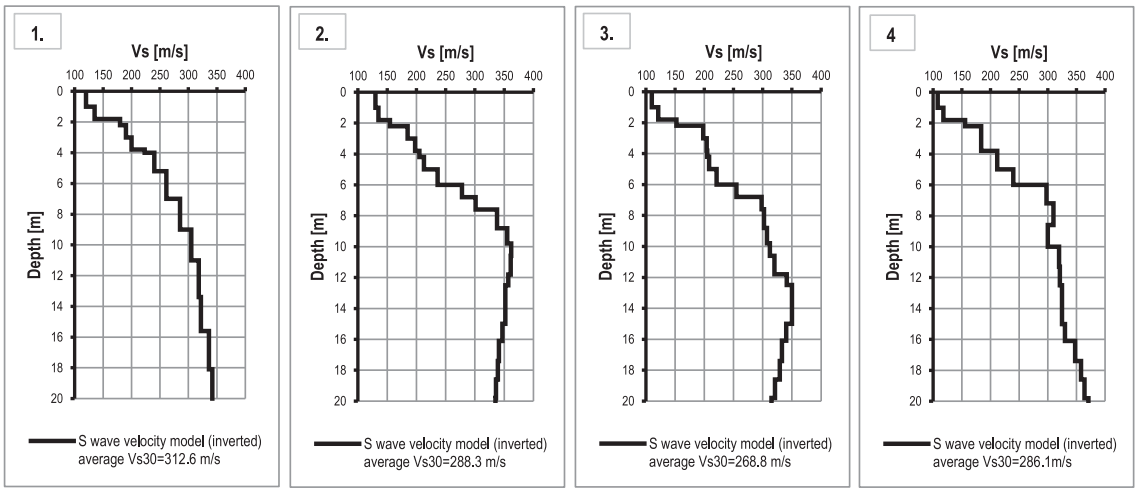

Figure 4. 1D V_S profile vs. depth. Location: 1) Landfill - Kneginec, 2) Water well - Varaždin, 3) Zagreb street - Varaždin, 4) Motičnjak - Trnovec.

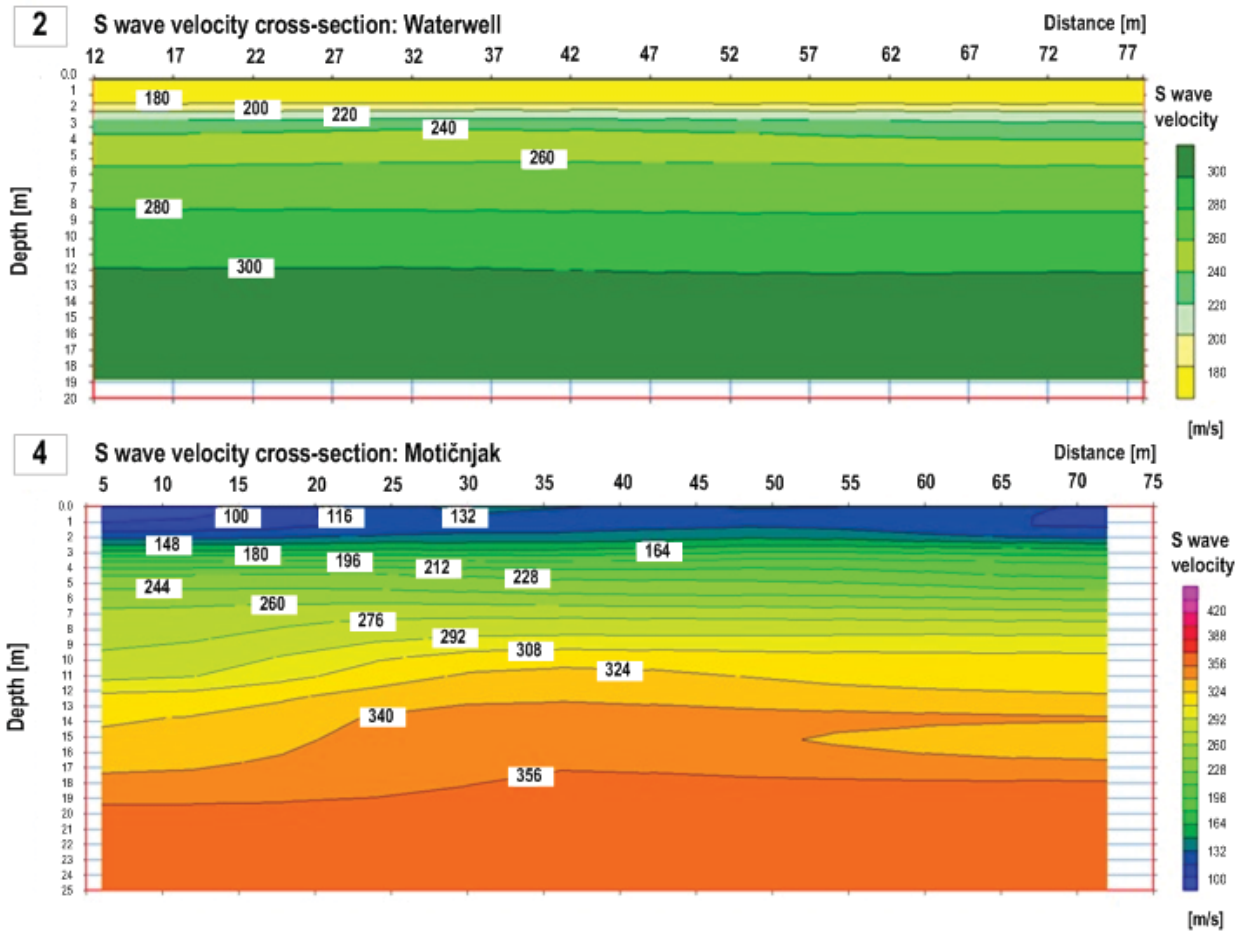

Figure 5. 2D V_S profile vs. depth. Location: 2) Water well - Varaždin, 4) Motičnjak - Trnovec.

3.3 Dynamic probing heavy (DPH) test

The purpose of an in-situ dynamic probing test is to determine the resistance of soils and semi-rocks in-situ via the dynamic penetration of a cone in order to characterize the soil layers by their depth, position, nature, density or thickness [35, 36]. It can be used to determine the strength and deformation properties of soils or to distinguish non-cohesive soils from cohesive soils [37]. In our study we used one type of dynamic penetrometer, Dynamic Probe Heavy (DPH - Fig. 6), which is more economically efficient and faster than SPT (borehole is needed), in line with EN ISO 22476 - 2 [38] and the European German DIN 4094 - 2 standards [39].

DPH is performed so that the cone (base area of cone point 20 cm^2) is driven into the soil (no borehole needed) by free-fall hammer strokes with a specified mass (50 kg) and height of the drop (50 cm). The numbers of strokes required for a 100-mm penetration of the cone N_{DPH} are recorded.

The penetration resistance is defined as the number of strokes N_{DPH} per 100 mm of penetration. A continuous record is collected in accordance with the length of sinking (depth). The test does not allow for soil sampling. The results from the DPH test are presented as the number of strokes N_{DPH} against the depth from the direct field record and are in the range of standardized values (usually 3 up to 50) (see Fig. 7). The "harsh" spikes that appear occur when encountering obstructions such as a boulder or very hard, dense soil. When the test is carried out in granular soils below the water table, the soil may become loosened, and the number of strokes N_{DPH} can decrease. Groundwater influence (loosening) on the number of strokes N_{DPH} is significant, and corrections have to be made according to EN ISO22476 - 2 and DIN 4094 - 3 [38, 39].

A groundwater-level correction was made for sand: $N_{DPH}{}^{CORR} = 1.3 \cdot N_{DPH}{}^{ORIG} + 2$ and for gravel: $N_{DPH}{}^{CORR} = 1.2 \cdot N_{DPH}{}^{ORIG} + 4.5$ [40, 41, 42], but was not necessary for clay, which was above the groundwater level. Remov-

Figure 6. Geotool dynamic probing rig (Dynamic Sampling Ltd, UK). The rig is capable of dynamic probing (DPL-light, DPM-medium, DPH-heavy and DPSH-super heavy) in accordance with DIN 4094. Specification: Width 78 cm, Length 78.5 cm, Height 23.4 cm, Drop Height 50 cm, Rod/Tool Length 120 cm (max) and Basic Weight 125 kg. Reference penetration every 100 mm. Base area of cone 20 cm^2. Cone diameter 43.7 mm. Rods diameter 32 mm. Hammer mass 50 kg. Drop height 50 cm. Angle of the cone point 90º. Torque wrench for impact of rod skin friction.

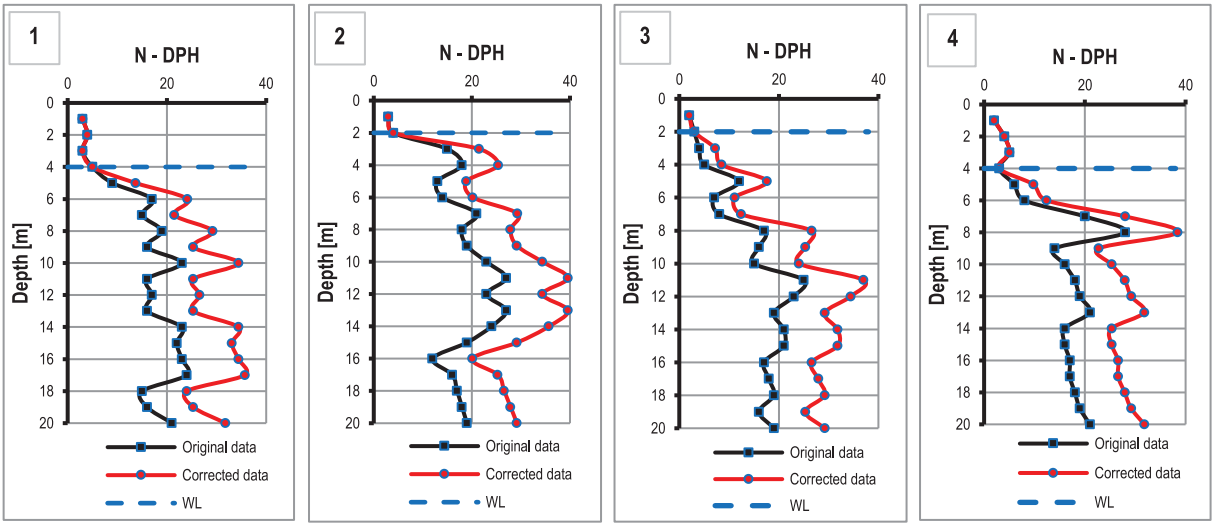

Figure 7. N_{DPH} profile vs. depth.Location: 1) Landfill - Kneginec, 2) Water well - Varaždin, 3) Zagreb street - Varaždin, 4) Motičnjak - Trnovec (depth to 15 m). WL - water level mark.

ing the effect of water increases the number of recorded strokes (Fig. 7). Fig. 7 shows how the numbers of strokes N_{DPH} are changing with depth. The top first layer is clay with a N_{DPH} range from 1 to 5 (without groundwater correction), the second layer sand with N_{DPH} range from 4 to 25 (corrected 7–38), while the third layer is classified as gravel with N_{DPH} from 12 to 27 (corrected 20–40).

4. EMPIRICAL CORRELATION BETWEEN THE SHEAR-WAVE VELOCITY AND THE DYNAMIC PROBING HEAVY TEST

In this section we present an empirical correlation between the shear-wave velocity V_S and the dynamic probing test DPH in shallow quaternary alluvial sediments for a local geological site-specific case study at four locations in Varaždin using the power law given by Eq. 1.

From the V_S and N_{DPH} profiles we extracted good data for the statistical correlations with depth. The following example (location 3 - Zagreb street) of the measured data shown in Fig. 4 and 7 depicts the development of the V_S - N_{DPH} empirical correlations. Example: for a depth of 10 m, the measured shear-wave velocity is V_S = 320 m/s and the number of blows N_{DPH} = 17 are taken as a mean value between depths of 9–10 m. Since at this depth the soil is classified as gravel below the water table, we performed a groundwater-level correction:

$N_{DPH}{}^{CORR} = 1.2 \cdot N_{DPH}{}^{ORIG} + 4.5 = 25$. In this way we extracted more than 200 points from all the measurements at all four locations with two different field methods (MASW and DPH).

In Fig. 8 empirical V_S - N_{DPH} correlations shown for a particular test location are presented. V_S - N_{DPH} correlations for the original (black) and corrected (red) N_{DPH} data are shown on all four graphs. It is evident that the data correction due to the groundwater effect on N_{DPH} causes the curve to shift down on the V_S axis (red vs. black) and that in all four cases R^2 (determination coefficient) is higher than in the original N_{DPH} data.

The V_S - N_{DPH} correlation is statistically better for a groundwater-level correction on N_{DPH}. It can also be seen that R^2 is above 0.85 at two locations, i.e., 1. Landfill and 3. Zagreb street, irrespective of the groundwater correction (WL = 4 m and 2 m of depth). For the other two locations, i.e., 2. Water well and 4. Motičnjak, R^2 is comparatively low and shows a significant change from the groundwater correction. Since all the field measurements were performed in shallow quaternary alluvial sediments, the main aim of this study is to propose a site-specific V_S - N_{DPH} correlation, rather than more general correlations. Fig. 9 presents empirical V_S - N_{DPH} correlations for the site-specific region of Varaždin compared to a few previously published empirical V_S – N_{SPT} correlations for all soils [5]:

Original N_{DPH}: $V_S = 97.839 \cdot N_{DPH}{}^{0.395}$; $R^2 = 0.723$

Corrected N_{DPH}: $V_S = 92.998 \cdot N_{DPH}{}^{0.363}$; $R^2 = 0.815$.

5 DISCUSSION

From the empirical V_S - N_{DPH} correlation (Fig. 9) it can be seen how corrections for the groundwater effect on DPH measurements can "enhance" the correlation (R^2 is higher).

But, to see real meaning in this correction, we compared the MASW measured $V_{S,meas}$ with the estimated $V_{S,orig}$ and $V_{S,corr}$ from the original $N_{DPH}{}^{ORIG}$ and the corrected $N_{DPH}{}^{CORR}$ data (Fig. 10). There is a small difference between the MASW measured $V_{S,meas}$ and the estimated $V_{S,orig}$ and $V_{S,corr}$ from the V_S - N_{DPH} correlation. The residuals are from 0 to 50 m/s, and this difference falls

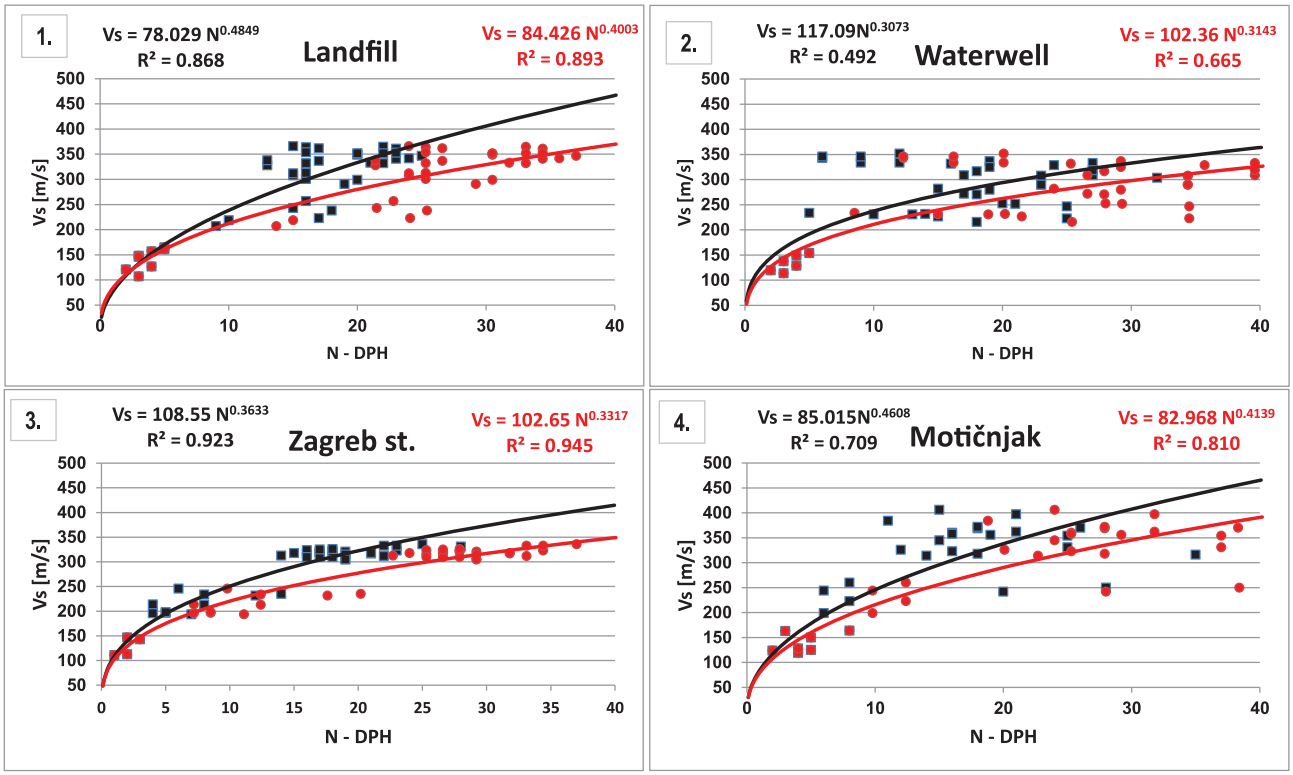

Figure 8. V_S - N_{DPH} correlations by test location: 1) Landfill - Kneginec, 2) Water well - Varaždin, 3) Zagreb Street - Varaždin, 4) Motičnjak - Trnovec. Black - original N_{DPH} data. Red - corrected N_{DPH} data.

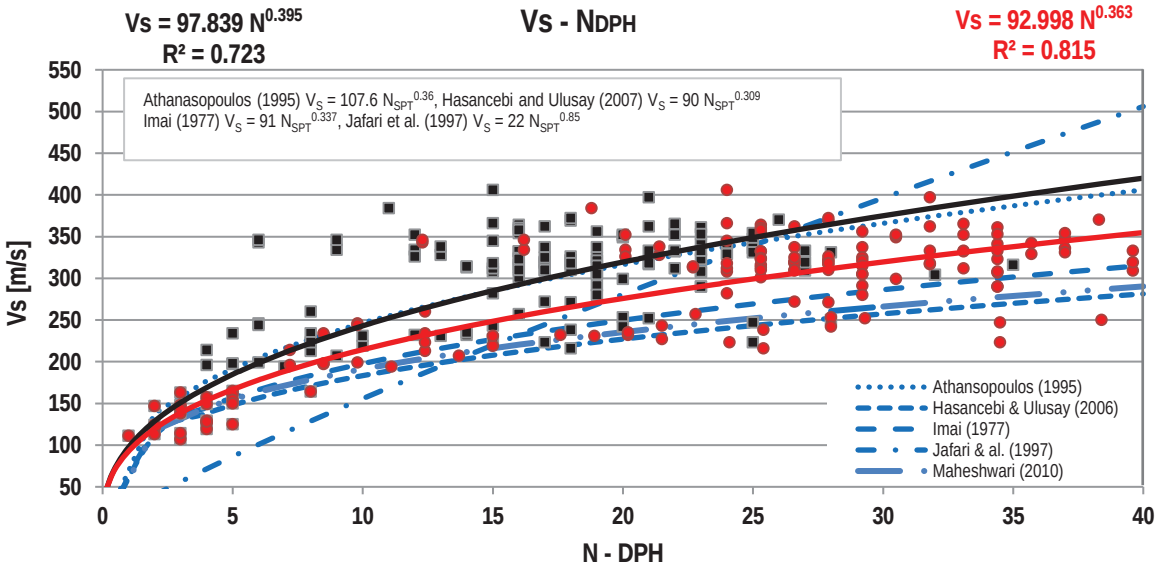

Figure 9. V_S - N_{DPH} correlations for site-specific region of Varaždin (all locations, all soils; black line: original N_{DPH}, red line: corrected N_{DPH}). Also presented are a few previously published V_S - N_{SPT} correlations for all soils [5]: blue dotted and dashed lines).

within statistical error bounds and so the given results can be used as a rough estimation of V_S from N_{DPH}. A groundwater-level correction is a good way to "statistically enhance" an empirical correlation, but as seen in Fig. 10 there is a very small difference between the $V_{S,orig}$ estimated from N_{DPH}^{ORIG} and the $V_{S,corr}$ estimated from N_{DPH}^{CORR}. Both empirical correlations are sufficient for a rough estimation of V_S from N_{DPH} and the groundwater-level correction can be applied to lower the statistical error, but the correlation with raw (original) data can also be effective in estimating V_S from N_{DPH}.

From the field measurements and empirical correlations, the shear-wave velocity V_S was estimated and dynamic elastic moduli (*Go*, *Eo* and *Er*) based on that velocity were calculated, Fig. 11, 12, 13. In the calculation of the shear modulus *Go* (Eq. 2), the Young's modulus *Eo* (Eq. 4) and the reference Young's modulus *Er* (Eq. 6), the

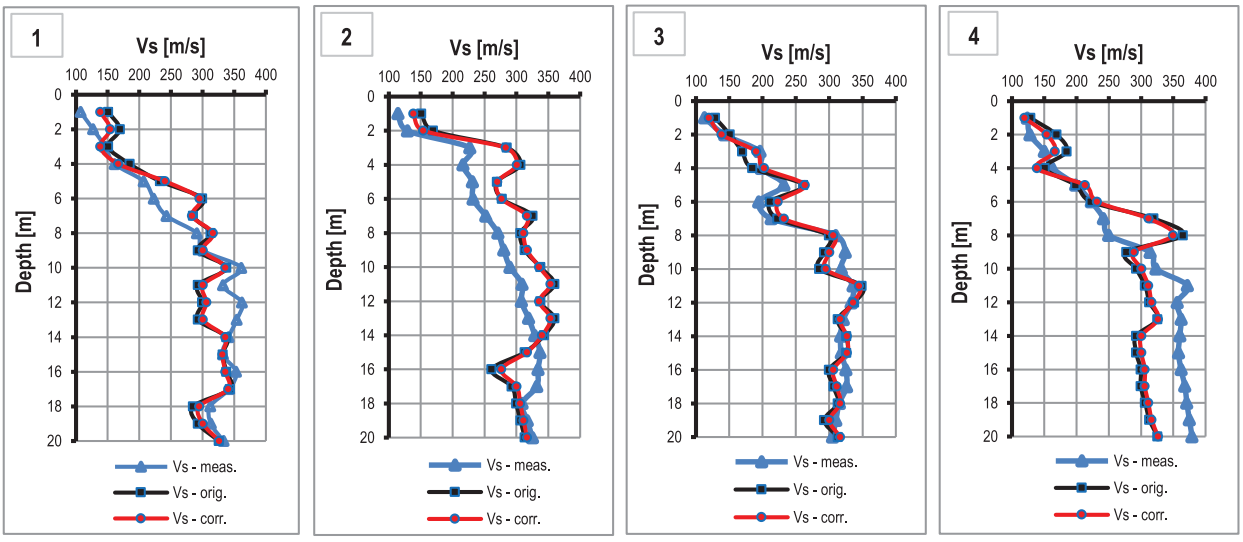

Figure 10. Comparison between measured V_S (blue: $V_{S,meas}$), V_S estimated from N_{DPH}^{ORIG} (black: $V_{S,orig}$) and V_S estimated from N_{DPH}^{CORR} (red: $V_{S,corr}$).

soil density was evaluated using Eq. 3, while Poisson's ratio with values of $\upsilon = 0.20$ and $\upsilon = 0.45$ for dry and soil under the water table was used. From Fig. 11, 12 and 13 the shear modulus *Go* varies from 20 MPa (MN/m^2) to 292 MPa, the Young's modulus *Eo* varies from 49 MPa to 846 MPa, and reference Young's modulus *Er* varies from 9 MPa to 158 MPa for the Varaždin region.

The estimated elastic moduli *Go*, *Eo* and *Er* were cross-checked at low (MASW) and high (DPH) strains and they made a good match (especially for test location 3. Zagreb street). High deviated results (test locations 1. Landfill, 2. Water well and 4. Motičnjak) can be explained by a number of factors pertaining to local soils, such as the particle distribution, plasticity, soil texture, loose soil, sticking cone into the boulder, etc., and thus the V_S - N_{DPH} correlation should be used with caution.

Two different approaches (low vs. high strain) were compared, and the results found to be in good agree-

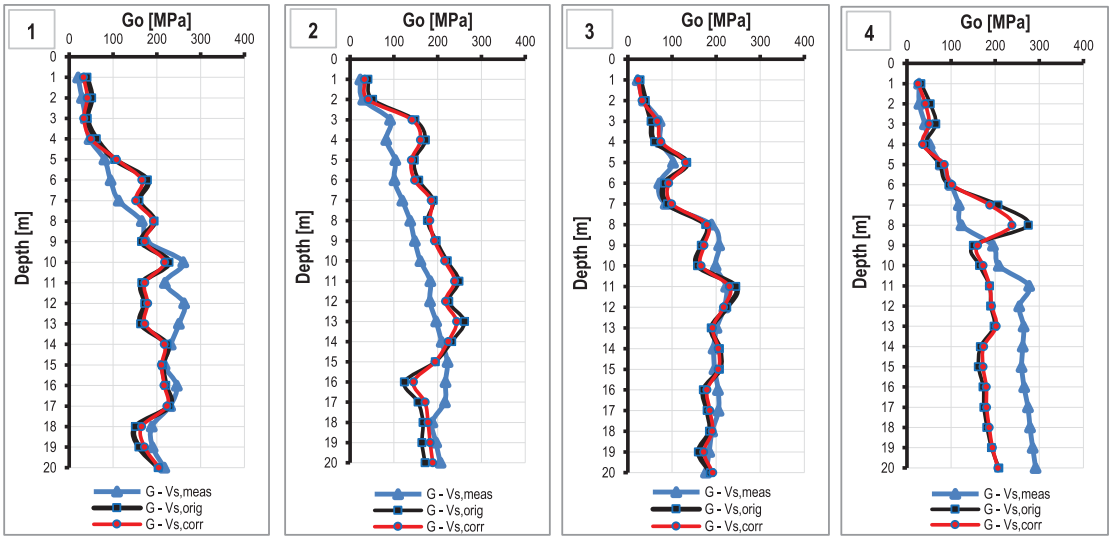

Figure 11. Shear modulus *Go* (low strain) calculated from measured V_S (blue: $V_{S,meas}$), V_S estimated from $N_{DPH}{}^{ORIG}$ (black: $V_{S,orig}$) and V_S estimated from $N_{DPH}{}^{CORR}$ (red: $V_{S,corr}$).

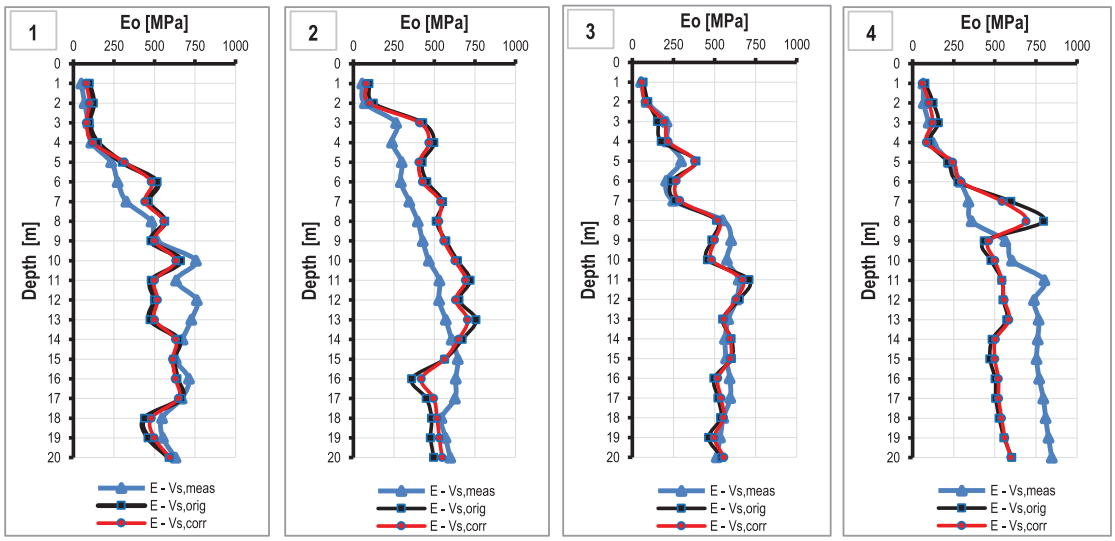

Figure 12. Young's modulus *Eo* (low strain) calculated from measured V_S (blue: $V_{S,meas}$), V_S estimated from $N_{DPH}{}^{ORIG}$ (black: $V_{S,orig}$) and V_S estimated from $N_{DPH}{}^{CORR}$ (red: $V_{S,corr}$).

ment when the relative difference between the velocities is small and smooth, Fig 14.

The relative difference of velocities (RD(o/m) or RD(c/m)) is defined as the ratio of the absolute difference between the measured and estimated velocity and the measured velocity for some depth:

$$RD = \frac{abs\left(1 - V_{S,estimated}\right)}{V_{S,measured}} \qquad (7)$$

One can find that the local extremes of the RD curves, Fig. 14, match the local extremes of the *N - DPH* curves, Fig. 7. Moreover, if the relative difference of the velocities is small and the curve is smooth, Fig. 14 location 3, then the local RD maximum indicates a local *N - DPH* minimum, and vice versa. When there is a significant spike in the *N - DPH* data we can expect a significant dispersion of the V_S - N_{DPH} data, Fig. 14 location 4.

Regardless of the field measurements, at low (MASW) or high (DPH) strains, it is necessary to evaluate the

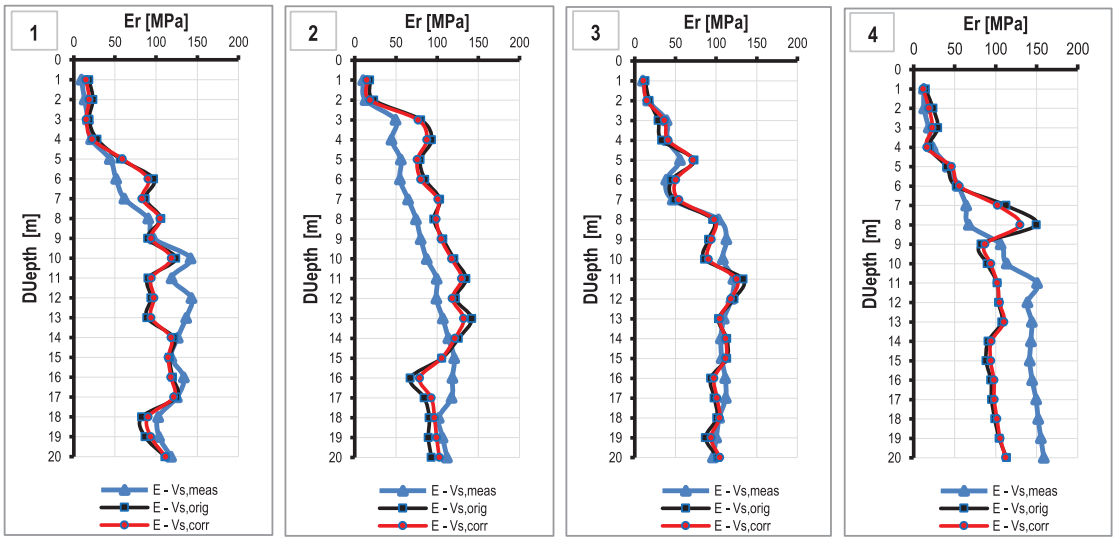

Figure 13. Young's modulus *Er* (high strain) calculated from measured V_S (blue), V_S estimated from N_{DPH}^{ORIG} (black) and V_S estimated from N_{DPH}^{CORR} (red).

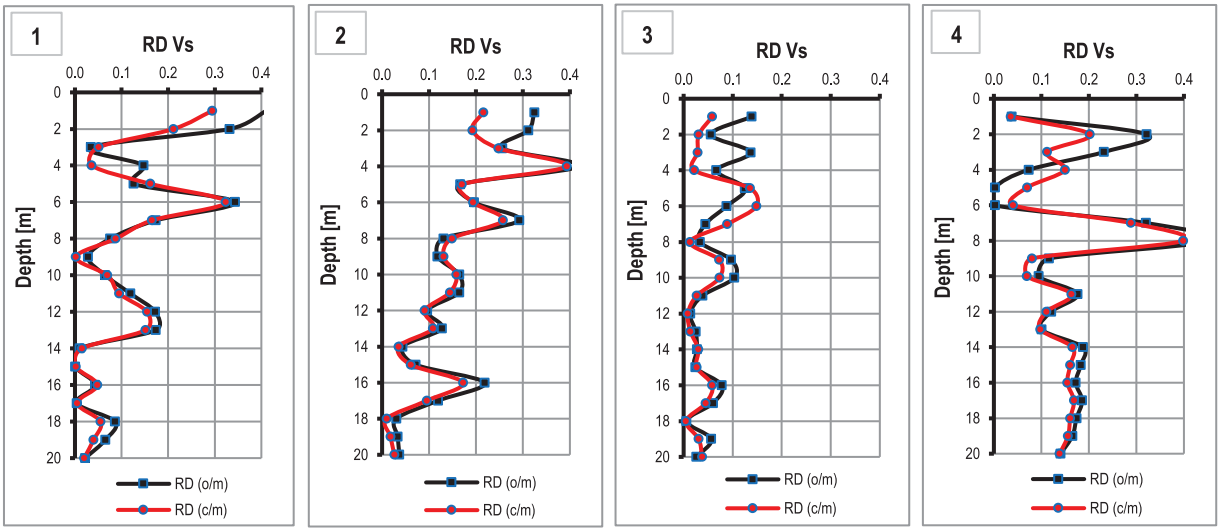

Figure 14. Relative difference between the estimated and measured velocities. RD(o/m or c/m) is a relative difference of V_S estimated from N_{DPH}^{ORIG} or V_S estimated from N_{DPH}^{CORR} and measured MASW velocity V_S (black and red line respectively).

appropriate dynamic properties of the materials in the soil deposit. A precise determination of the dynamic soil properties is a somewhat difficult task when solving geotechnical engineering problems. It is clear that the choice of technique depends on the problem to be solved. Dynamic properties play a vital role in the design of earthquake-resistant structures or structures subjected to dynamic loads.

6 CONCLUSION

In this paper we present empirical correlations between the shear-wave velocity V_S and the dynamic probing test (DPH) for s case study in a site-specific region of Varaždin. The geological characteristics of Varaždin are quaternary alluvial soft sediments of the Drava river basin (Fig. 2). Field measurements (low strain - MASW, high strain - DPH) were carried out at four different test locations inside and outside the city of Varaždin. Since Varaždin sits on alluvial soft sediments, the penetration resistance of the N_{DPH} groundwater-level correction was taken into consideration. An empirical correlation was developed between the measured shear-wave velocity V_S and the raw (original) $N_{DPH}{}^{ORIG}$ and groundwater-level-corrected $N_{DPH}{}^{CORR}$ data. The results of the developed empirical correlation (Fig. 9) for $N_{DPH}{}^{ORIG}$ and for $N_{DPH}{}^{CORR}$ were:

$$V_S = 97.839 \cdot N_{DPH}{}^{0.395};\ R^2 = 0.723,$$

$$V_S = 92.998 \cdot N_{DPH}{}^{0.363};\ R^2 = 0.815.$$

The groundwater-level correction was found to be effective in "statistically enhancing" the empirical correlations, which can be seen in Fig. 10. There is a very small difference between $V_{S,\mathrm{orig}}$ estimated from $N_{DPH}{}^{ORIG}$ and $V_{S,\mathrm{corr}}$ estimated from $N_{DPH}{}^{CORR}$. These developed empirical correlations proved to be sufficient for rough estimations of V_S from N_{DPH} and the groundwater-level correction can be applied in order to lower the statistical error, but a correlation with raw (original) data can also be effective in a good way for estimating V_S from N_{DPH}.

The shear-wave velocity V_S is one of the most important parameters for a determination of the dynamic soil properties and the ground response analysis. From the field measurements and empirical correlations, the shear-wave velocity V_S, the dynamic elastic moduli of the shear modulus (*Go*) (Eq. 2) and the Young's modulus (*Eo* and *Er*) (Eq. 4 and 6) were estimated (Fig. 11, 12, 13). Two different approaches (low vs. high strain) were compared, and the results found to be in good agreement when the relative difference between the velocities is small and smooth, Fig 14.

The measured dynamic soil properties (V_S, *Go*, *Eo*, *Er*) can be used for the seismic design of structures based on Eurocode 8 [17, 18, 19], site response studies [2], settlement analysis and V_S is also widely used in liquefaction assessments [1].

Preliminary seismic tests proved that dynamic probing tests are effective when looking at a discrete point of interest in a large field area. The suggested correlation V_S - N_{DPH} can be used to make rough estimations of V_S from N_{DPH} (they are site-specific, and so not applicable worldwide). It should not be used as a substitute for seismic measurements, but used as a comparison and verification of the measured shear-wave velocity and dynamic probing test for site-specific dynamic soil properties. In this way very useful information about the dynamic soil properties can be extracted for ground-response analyses and the study of local site effects, particularly for preliminary studies and/or noncritical projects that are under consideration.

REFERENCES

[1] Kramer, S.L. 1996. Geotechnical Earthquake Engineering. Prentice Hall, New Jersey.
[2] Reiter, L. 1990. Earthquake Hazard Analysis. Columbia University Press, New York.
[3] Barton, N. 2007. Rock Quality, seismic velocity, attenuation and anisotropy. Taylor & Francis Group, London.
[4] Hanumantharao, C., Ramana, G.V. 2008. Dynamic soil properties for microzonation of Delhi, India. J. Earth Syst. Sci. 117 S2, 719-730.
[5] Marto, A., Soon, T.C., Kasim, F. 2013. A correlation of shear wave velocity and standard penetration resistance. EJGE, 18, 463-471.
[6] Jafari, M.K., Shafiee, A., Razmkhah, A. 2002. Dynamic properties of fine grained soils in south of Tehran. Soil Dyn. and Earthquake Eng. 4, 25-35.
[7] Uma Maheswari, R., Boominathan, A., Dodagoudar, G.R. 2010. Use of Surface Waves in Statistical Correlations of Shear Wave Velocity and Penetration Resistance of Chennai soils. Geotechnical and Geology Engineering 119–137.
[8] Kuo, C.H., Wen, K.L., Hsieh, H.H., Chang, T.M., Lin, C.M., Chen, C.T. 2011. Evaluating Empirical Regression Equations for V_S and Estimating VS30 in Northeastern Taiwan. Soil Dyn. and Earthquake Eng. 31, 431-439.
[9] Akin, M.K., Kramer, K.L., Topal, T. 2011. Empirical Correlations of Shear Wave Velocity (VS) and Penetration Resistance (SPT-N) for Different Soils in an Earthquake prone Area (Erbaa-Turkey). Engineering Geology 119, 1-17.
[10] Anbazhagan, P., Kumar, A., Sitharam, T.G. 2013.

Seismic Site Classification and Correlation between Standard Penetration Test N Value and Shear Wave Velocity for Lucknow City. Indo-Gangetic Basin. Pure and Applied Geophysics 170, 299-318.
[11] Iyisan, R. 1996. Correlations between Shear Wave Velocity and In-Situ Penetration Test Results. Digest. 96, 371-374.
[12] Mayne, P.W., Schneider, J.A. 1999. Small and large strain soil properties from seismic flat dilatometer tests. Proc. Pre-failure Deformation Characteristics of Geomaterials, Jamiolkowski et al. editors, Torino, 419-426.
[13] Aki, K., Richards, P.G. 2009. Quantitative Seismology. University Science Book, California.
[14] Mavko, G., Mukerji, T., Dvorkin, J. 2003. The Rock Physics Handbook. Cambridge University Press, Cambridge.
[15] Ohsaki, Y., Iwasaki, R. 1973. Dynamic shear moduli and Poisson's ratio of soil deposits; Soils and Foundn. 13, 61-73.
[16] Burns, S.E., Mayne, P.W. 1996. Small and high strain soil properties using the seismic piezocone. Transport. Research Record 1548, National Acad. Press, Wash. DC, 81-88.
[17] CEN 2004. Eurocode 8 - design of structures for earthquakes resistance. Part 1 - general rules, seismic actions, design and rules for building. European standard EN 1998 -1, December 2004, European Committee for Standardization, Brussels.
[18] Hrvatski zavod za norme, 2011a. HRN EN 1998-1:2011 hr, Eurokod 8: Projektiranje potresne otpornosti konstrukcija -1. dio: Opća pravila, potresna djelovanja i pravila za zgrade (EN 1998-1:2004+AC:2009). HZN - Oglasnik za normativne dokumente 6/2011.
[19] Hrvatski zavod za norme, 2011b. Nacionalni dodatak za niz normi HRN EN 1998 - 1:2011/NA:2011, Eurokod 8: Projektiranje potresne otpornosti konstrukcija - 1.dio: Opća pravila, potresna djelovanja i pravila za zgrade.
[20] Markušić, S., Herak, M. 1999. Seismic zoning of Croatia. Natural Hazards 18, 269 - 285.
[21] Prelogović, E., Velić, J. 1988. Quaternary tectonic activity in western part of the Drava depression. Geološki vjesnik 41, 237 - 253.
[22] Babić, Ž., Čakarun, I., Sokač, A., Mraz, V. 1978. On geological features of quaternary sediments of Drava basin on Croatian territory. Geološki vjesnik 30(1), 43 - 61.
[23] Urumović, K. 1971. On quaternary aquifer complex in Varaždin area. Geološki vjesnik 24, 183 - 191.
[24] Urumović, K., Hlevnjak, B., Prelogović, E., Mayer, D. 1990. Hydrogeological conditions of Varaždin aquifer. Geološki vjesnik 43, 149 - 158.
[25] Nazarian, S., Stokoe II, K.H. 1984. In situ shear wave velocity from spectral analysis of surface waves, 8th World Conference on Earthquake Engineering Proceedings, 31-38.
[26] Stokoe II, K.H., Nazarian, S. 1983. Effectiveness of ground improvement from spectral analysis of surface waves, 8th Euro. Conf. on Soil Mech. and Found. Engin. Proceedings, 91-94.
[27] Stokoe II, K.H., Wright, G.W., Bay, J.A., Roesset, J.M. 1994. Characterization of geotechnical sites by SASW method, in Geophysical characterization of sites, ISSMFE Technical Committee #10, edited by R.D. Woods, Oxford Publishers, New Delhi.
[28] Park, C.B, Xia, J., Miller, R.D. 1998b. Imaging dispersion curves of surface waves on multichannel record, 68th Ann. Internat. Mtg., Soc. Expl. Geophys., Expanded Abstracts, 1377-1380.
[29] Xia, J., Miller, R.D., Park, C.B. 1999. Estimation of near-surface shear-wave velocity by inversion of Rayleigh wave: Geophysics 64, 691 - 700.
[30] Park, C.B, Miller, R.D, Xia, J. 1999. Multichannel analysis of surface waves. Geophysics 64, 3, 800-808.
[31] Park, C.B., Miller, R.D., Xia, J., Hunter, J.A., Harris, J.B. 1999. Higher mode observation by the MASW method: Technical Program with Biographies, SEG, 69th Annual Meeting, Houston, TX, 524-527.
[32] Xia, J., Miller, R.D., Park, C.B., Hunter, J.A., Harris, J.B. 1999. Evaluation of the MASW technique in unconsolidated sediments: Technical Program with Biographies, SEG, 69th Annual Meeting, Houston, TX, 437-440.
[33] Miller, R.D, Xia, J., Park, C.B., Ivanov, J.M. 1999. Multichannel analysis of surface waves to map bedrock. Leading Edge 18, 12, 1392-1396.
[34] http://www.masw.com/DataAcquisition.html/ <1.12.2014.>
[35] Waschkowski, E. 1982a. Dynamic Probing and Site Investigation. Proc. ESOPT 2, Amsterdam.
[36] Waschkowski, E. 1982b. Dynamic Probing and Practice. Proc. ESOPT 2, Amsterdam.
[37] Hack, R., Azzam, R., Charlier, R. 2004. Engineering geology for infrastructure planning in Europe: a European perspective. Springer, Berlin.
[38] EN ISO 22476 - 2: 2005: Geotechnical Engineering - Field testing - Part 2: Dynamic probing.
[39] DIN 4094: 2002: Subsoil - Field Investigations. Part 3: Dynamic probing.
[40] BS EN 1997 - 2: 2007. Eurocode 7 - Geotechnical design - Part 2: Ground investigation and testing, London.
[41] Stenzel, G., Melzer, K. J. 1978. Soil Investigations by Penetration Testing According to DIN 4094. Tief bau 20, 155-160, 240-244.
[42] Czado, B., Pietras, J.P. 2012. Comparison of the cone penetration resistance obtained in static and dynamic field test. AGH Journal of Mining and Geoengineering 36, 1, 97-105.

VREDNOTENJE PLASTIČNE KRITIČNE GLOBINE ZA PROBLEME SEIZMIČNIH AKTIVNIH BOČNIH ZEMELJSKIH PRITISKOV Z METODO NAPETOSTNIH KARAKTERISTIK

Amin Keshavarz
Persian Gulf University,
School of Engineering
Shahid Mahini Street, Bushehr, Iran
E-pošta: keshavarz@pgu.ac.ir

Ključne besede

plastična kritična globina, značilnosti napetosti, aktivni bočni zemeljski pritisk, potresno

Izvleček

Plastična kritična globina ali običajno imenovana globina natezne razpoke ima precejšen vpliv na aktivne bočne zemeljske pritiske v koherentnih tleh. V prispevku je globina za c-ϕ zemljino določena za primer potresa z uporabo napetostnih karakteristik ali metodo porušnic. Plastična kritična globina je bila izračunana na podlagi teorije metode napetostnih-karakteristik in ob upoštevanju horizontalnih in vertikalnih psevdo-statičnih potresnih koeficientov. Predlagana rešitev obravnava črto diskontinuitete v mreži napetostnih karakteristik. V analizi so bili prav tako upoštevani naklon zaledja in zidu, kohezija in notranji kot trenja ter tudi adhezija in kot trenja na površini med zemljino in zidom. Rezultati kažejo, da so plastične kritične globine te študije manjše od drugih metod in so bližje modificirani metodi Mononobe-Okabe.

EVALUATION OF THE PLASTIC CRITICAL DEPTH IN SEISMIC ACTIVE LATERAL EARTH PRESSURE PROBLEMS USING THE STRESS-CHARACTERISTICS METHOD

Amin Keshavarz
Persian Gulf University,
School of Engineering
Shahid Mahini Street, Bushehr, Iran
E-mail: keshavarz@pgu.ac.ir

Keywords

plastic critical depth, stress characteristics, active lateral earth pressure, seismic

Abstract

The plastic critical depth or the conventional tension crack depth has a considerable effect on the active lateral earth pressure in cohesive soils. In this paper the depth for c-ϕ soils has been evaluated in the seismic case using the stress-characteristics or slip-line method. The plastic critical depth was calculated on the basis of the theory of the stress-characteristics method and by considering the horizontal and vertical pseudo-static earthquake coefficients. The proposed solution considers the line of discontinuity in the stress-characteristics network. The earth slope, wall slope, cohesion and friction angle of the soil and the adhesion and the friction angle of the soil-wall interface were considered in the analysis as well. The results show that the plastic critical depths of this study are smaller than those of the other methods and are closer to the modified Mononobe-Okabe method. The effects of the wall and the backfill geometry, the mechanical properties of the soil and the pseudo-static coefficients were studied.

1 INTRODUCTION

In cohesive soils, the computed active lateral earth pressure can be negative from the ground surface to some depth. The plastic critical depth is the depth where the computed soil pressure is negative from the ground surface to that depth. To calculate the active lateral earth pressure many engineers assume that the lateral earth pressure is zero from the ground surface to the plastic critical depth. Therefore, the calculation of the plastic critical depth is important in any evaluation of the active lateral earth pressure. Numerical examples showed that if the plastic critical depth is considered, the static lateral earth pressure can be more than 20 to 40 percent of the lateral earth pressure, without taking into account the plastic critical depth [1].

Peng [2] assumed that the failure surface is planar and evaluated the static active lateral earth pressure using the limit-equilibrium method. He considered the plastic critical depth and the surcharge in his study. Peng [3] modified the Mononobe-Okabe method to calculate the seismic active lateral earth pressure. He presented some equations to calculate the lateral earth pressure and the plastic critical depth in *c-ϕ* soils.

Nian and Han [4] calculated the seismic active lateral earth pressure against rigid retaining walls. They used the Rankin theory and proposed an equation to estimate the plastic critical depth. In their study the retaining wall is vertical, but the ground surface can be inclined. Also, Iskander et al. [5] expanded the Rankin solution for seismic cases and proposed an equation for the plastic criti-

cal depth. Ma et al. [6] evaluated the lateral earth pressure and the plastic critical depth using the pseudo-dynamic method. Recently, Lin et al. [7] used the slice-analysis method to compute the nonlinear distribution of the seismic active earth pressure of cohesive-frictional soil.

The stress-characteristics or slip-line method is one of the famous methods for analysing geotechnical problems. This method was presented by Sokolovski [8, 9]. Reece and Hettiaratchi [10] and Kumar and Chitikela [11] used the stress-characteristics method to compute the passive lateral earth pressure. Cheng [12] proposed a rotation of the axes in the stress-characteristics method to determine the seismic lateral earth pressure. Peng and Chen [13] applied this method to compute the active lateral earth pressure in the static case. The stress-characteristics method has also been used to evaluate the stability of reinforced soil structures [14, 15].

Table 1 summarizes the different methods for calculating the plastic critical depth. The parameters used in the table will be defined in the next sections. It is clear that most of the methods proposed closed-form solutions. Some of them need trial and error, and three of them consider all the parameters in the solution.

In this paper the plastic critical depth is studied using the stress-characteristics method. Although Peng and Chen [13] used this method to compute the active lateral earth pressure, they did not consider the seismic effects

Table 1. Summary of different methods to calculate the plastic critical depth.

No.	Proposed by	Theory	Parameters considered				Comments
1	Rankin	Simple Rankin	c_w	☒	δ_w	☒	- The simplest equation (Eq. (25))
			θ	☒	β	☒	
			k_h	☒	k_v	☒	
			q	☑			
2	Peng, 2012 [3]	Modified Mononobe-Okabe	c_w	☑	δ_w	☑	- Closed form without trial and error
			θ	☑	β	☑	
			k_h	☑	k_v	☑	
			q	☑			
3	Ma et al., 2012 [6]	Pseudo-dynamic	c_w	☑	δ_w	☑	-No closed form - Needs optimization
			θ	☑	β	☒	
			k_h	☑	k_v	☑	
			q	☑			
4	Peng and Chen, 2013 [13]	Slip line	c_w	☑	δ_w	☑	-Closed form -Needs trial and error -When β=0 solution can be found without trial and error
			θ	☑	β	☑	
			k_h	☒	k_v	☒	
			q	☑			
5	Iskandet et al., 2013 [5]	Expanded Rankin	c_w	☒	δ_w	☒	- Closed form without trial and error
			θ	☑	β	☑	
			k_h	☑	k_v	☑	
			q	☒			
6	Nian and Han, 2013 [4]	Modified Rankin	c_w	☒	δ_w	☒	- Closed form without trial and error
			θ	☒	β	☑	
			k_h	☑	k_v	☑	
			q	☒			
7	Lin et al., 2015 [7]	Slice analysis method	c_w	☑	δ_w	☑	-Closed form -Needs trial and error
			θ	☑	β	☑	
			k_h	☑	k_v	☑	
			q	☑			
8	This study	Slip line	c_w	☑	δ_w	☑	-Closed form -Needs trial and error -When β=k_h=k_v=0, solution can be found without trial and error
			θ	☑	β	☑	
			k_h	☑	k_v	☑	
			q	☑			

and the discontinuity line in the stress field. In this study, the estimation of the plastic critical depth is explained clearly, and several analyses are made in different cases.

2 THEORY

The backfill is a c-ϕ soil, where c and ϕ are the cohesion and the friction angle of the soil, respectively. The soil obeys the Mohr-Coulomb failure criterion. The retaining wall is rigid, and the soil-wall interface has the adhesion c_w and the friction angle δ_w.

Figure 1 shows a soil element in the plane-strain case. There are two families of failure orientations, PA and PB, known as the negative and positive characteristics, and make a stress field. As shown, the stress-characteristics lines make the angle $\mu = \pi/4 - \phi/2$ with the orientation of the principal stress σ_1 [9]. Each point in the soil media has four features, x, z, p and ψ, where x and z are the coordinates of the point and p is the average stress in the Mohr's circle and ψ is the angle between σ_1 and the horizontal axis (Figure 1).

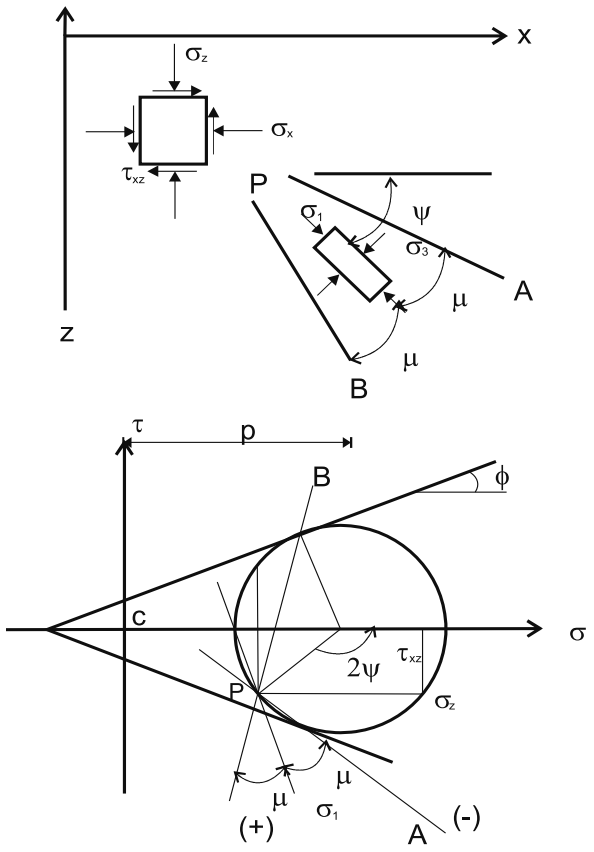

Figure 1. The orientation of the positive (σ^+) and negative (σ^-) characteristics and the Mohr's circle of stress [16].

If the body forces are zero, the equilibrium equations along the stress characteristics can be written as [9]:

$$2\left(p\tan\phi + c\right)d\psi + dp = 0 \qquad (1)$$

$$2\left(p\tan\phi + c\right)d\psi - dp = 0 \qquad (2)$$

2.1 Boundary conditions

Figure 2 shows the geometry of the problem. DE is the ground-surface boundary and has the surcharge q. β is the ground-surface angle with the horizontal axis and θ is the angle between the wall and the vertical axis. The positive signs of these angles are shown in the figure. k_h and k_v are the horizontal and vertical pseudo-static earthquake coefficients, respectively. The positive directions of the seismic accelerations are shown in the figure. To solve the problem, the boundary condition of the wall and ground surface must be calculated.

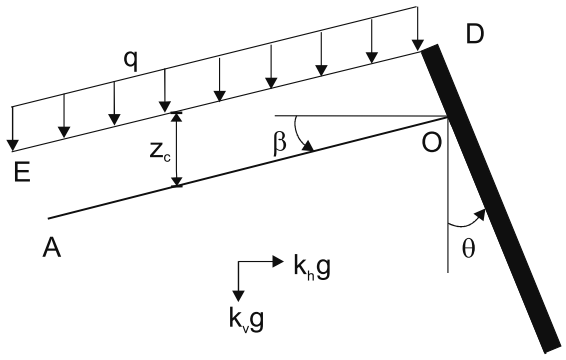

Figure 2. The geometry of the problem.

The Mohr's circles of stress along the ground surface and wall boundaries are shown in Figure 3. The normal and shear stresses on the ground surface can be written as

$$\sigma_0 = \overline{q}\cos\beta\left[\left(1-k_v\right)\cos\beta - k_h\sin\beta\right] = A_1\overline{q} \qquad (3)$$

$$\tau_0 = \overline{q}\cos\beta\left[\left(1-k_v\right)\sin\beta + k_h\cos\beta\right] = A_2\overline{q} \qquad (4)$$

where $\overline{q}$ is the equivalent surcharge (Eq. (18)) and

$$A_1 = \frac{\left(1-k_v\right)\cos\beta\cos\left(\delta+\beta\right)}{\cos\delta}$$
$$A_2 = \frac{\left(1-k_v\right)\cos\beta\sin\left(\delta+\beta\right)}{\cos\delta} \qquad (5)$$

and

$$\tan\delta = \frac{k_h}{1-k_v} \qquad (6)$$

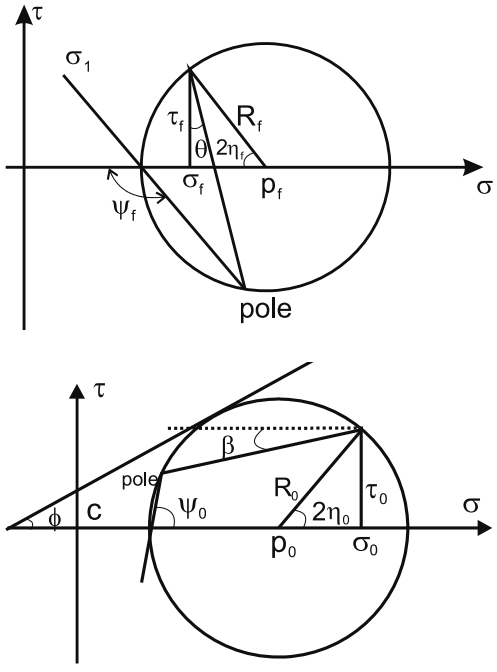

Figure 3. Mohr's circle of stress of the a) wall and b) ground surface.

The radius of the Mohr's circle on the ground surface can be written as (Figure 3b)

$$R_0 = p_0 \sin\phi + c\cos\phi = \sqrt{\left(\sigma_0 - p_0\right)^2 + {\tau_0}^2} \qquad (7)$$

From Eq. (7), the average stress on the ground surface, p_0, is

$$p_0 = \frac{\sigma_0 + c\cos\phi\sin\phi - \sqrt{\left(\sigma_0 \sin\phi + c\cos\phi\right)^2 - \left(\tau_0 \cos\phi\right)^2}}{\cos^2\phi} \qquad (8)$$

and using the Mohr's circle, we can write

$$\begin{aligned} \eta_0 &= \pi/2 + \beta - \psi_0 \\ \sigma_0 &= p_0 + \left(p_0 \sin\phi + c\cos\phi\right)\cos 2\eta_0 \\ \tau_0 &= \left(p_0 \sin\phi + c\cos\phi\right)\sin 2\eta_0 \end{aligned} \qquad (9)$$

The angle ψ_0 can be obtained from Eq. (9) as

$$\psi_0 = \frac{\pi}{2} + 0.5\left[\beta - \delta - \sin^{-1}\left(\frac{p_0 \sin\left(\delta + \beta\right)}{p_0 \sin\phi + c\cos\phi}\right)\right] \qquad (10)$$

Referring to Figure 3a, on the retaining wall boundary

$$\begin{aligned} \eta_f &= \psi_f - \pi/2 - \theta \\ \sigma_f &= p_f - \left(p_f \sin\phi + c\cos\phi\right)\cos 2\eta_f \\ \tau_f &= c_w + \sigma_f \tan\delta_w = \left(p_f \sin\phi + c\cos\phi\right)\sin 2\eta_f \end{aligned} \qquad (11)$$

The angle ψ on the wall, ψ_f, can be found from Eq. (11) as

$$\psi_f = \frac{\pi}{2} + \theta + 0.5\left[-\delta_w + \sin^{-1}\left(\frac{p_f \sin\delta_w + c_w \cos\delta_w}{p_f \sin\phi + c\cos\phi}\right)\right] \qquad (12)$$

2.2 Calculating the plastic critical depth

Since the stresses on the left- and right-hand side of point O are different, this point is a singularity point. To obtain the depth of the plastic critical depth without computing the whole network, the singularity point must be solved. If $\psi_f \geq \psi_0$, the stresses are continuous everywhere, but when $\psi_f < \psi_0$, there is a line of discontinuity in the stress field, which will be explained next. This type of discontinuity has been considered in some studies [9, 11, 17, 18]. Peng and Chen [13] stated that the solution obtained from this discontinuity is a virtual solution and does not represent reality. In this paper the discontinuity is used and the obtained results are in good agreement with other solutions.

If $\psi_f \geq \psi_0$, from Eq. (1), p_f can be found as

$$\begin{aligned} &\text{If} \quad \phi{=}0: \quad p_f = p_0 - 2c\left(\psi_f - \psi_0\right) \\ &\text{else} \quad : \quad p_f = -c\cot\phi + \left(p_0 + c\cot\phi\right)\exp\left[-2\tan\phi\left(\psi_f - \psi_0\right)\right] \end{aligned} \qquad (13)$$

But if $\psi_f < \psi_0$, a line of discontinuity exists in the problem. In this paper an approach similar to that of Lee and Herington [17] is used to solve this discontinuity. Figure 4 shows a soil element on the discontinuity line and Mohr's circle of stress for the left- and right-hand sides of this element.

Referring to Mohr's circle of stress (Figure 4), we can write

$$R_R \sin 2\left(\psi_R - \omega\right) = R_L \sin 2\left(\psi_L - \omega\right) \qquad (14)$$

$$p_R - R_R \cos 2\left(\psi_R - \omega\right) = p_L - R_L \cos 2\left(\psi_L - \omega\right) \qquad (15)$$

where ω is the angle between the discontinuity line and the horizontal axis, p_R, R_R and ψ_R are the average stress, the radius of the Mohr's circle and the angle ψ for the right-hand side of the discontinuity line, respectively. These parameters for the left-hand side of the discontinuity line are denoted by p_L, R_L and ψ_L. Using Eq. (14) and (15), ω and p_R can be obtained as

$$\omega = 0.5\left[\psi_R + \psi_L - \cos^{-1}\left(\sin\phi\cos\left(\psi_R - \psi_L\right)\right)\right] \qquad (16)$$

$$p_R = \frac{R_L \sin 2\left(\psi_L - \omega\right)}{\sin\phi \sin 2\left(\psi_R - \omega\right)} - c\cot\phi \qquad (17)$$

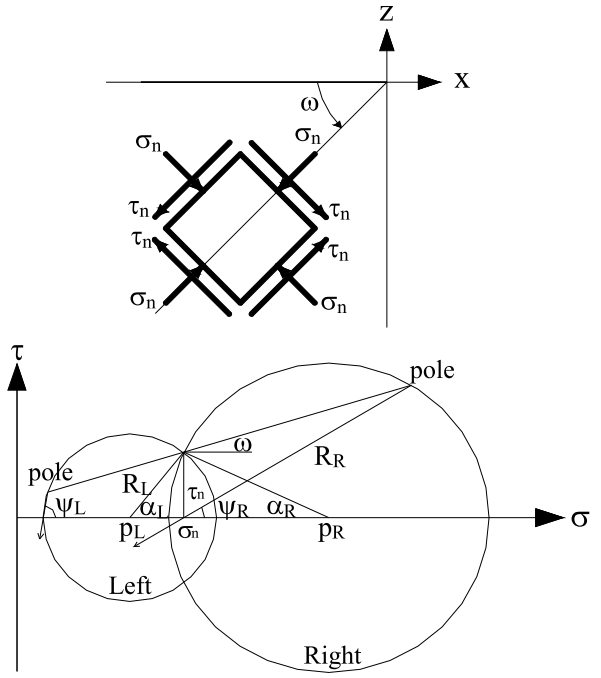

Figure 4. A soil element on the discontinuity line and Mohr's circle of stress of the element.

To calculate the plastic critical depth in active lateral earth pressure problems, an equivalent surcharge can be used [13]. This uniform equivalent surcharge on the OA boundary (Figure 2) can be written as

$$\overline{q} = q + \gamma z_c \qquad (18)$$

where z_c is the plastic critical depth and γ is the unit weight of the soil.

The equivalent surcharge $\overline{q}$ must be computed such that the normal stress on the wall is zero. When $\sigma_f = 0$, from Eq. (11) and (12) [13]

$$p_f = c\tan\phi + \frac{\sqrt{c^2 - {c_w}^2}}{\cos\phi} \qquad (19)$$

If $\psi_f \geq \psi_0$, the value of p_0 can be obtained from Eq. (13) as

$$\begin{aligned} &\text{If} \quad \phi{=}0: \quad p_0 = p_f + 2c\left(\psi_f - \psi_0\right) \\ &\text{else} \quad : \quad p_0 = -c\cot\phi + (p_f + c\cot\phi)\exp\left[2\tan\phi\left(\psi_f - \psi_0\right)\right] \end{aligned} \qquad (20)$$

and if $\psi_f < \psi_0$, using Eq. (17)

$$p_0 = -c\cot\phi + \sin 2\left(\psi_f - \omega_0\right)\frac{p_f + c\cot\phi}{\sin 2\left(\psi_0 - \omega_0\right)} \qquad (21)$$

where from Eq. (16)

$$\omega_0 = 0.5\left[\psi_f + \psi_0 - \cos^{-1}\left(\sin\phi\cos\left(\psi_f - \psi_0\right)\right)\right] \qquad (22)$$

Finally, from Eqs. (3), (4) and (7)

$$\overline{q} = \frac{A_1 p_0 + \sqrt{\left(p_0\sin\phi + c\cos\phi\right)^2\left({A_1}^2 + {A_2}^2\right) - \left(p_0 A_2\right)^2}}{{A_1}^2 + {A_2}^2} \qquad (23)$$

To calculate $\overline{q}$, first, p_f and ψ_f are calculated from Eqs. (19) and (12). Since p_0 and ψ_0 are not independent of each other, a trial-and-error procedure must be used to compute these parameters. First, an initial value is assumed for p_0, then ψ_0 is computed from Eq. (10) and based on the value of ψ_0, a new value for p_0 is obtained from Eq. (20) or (21). This procedure is repeated until the differences between the new and old values of p_0 and ψ_0 are small enough. Having p_0, the value of $\overline{q}$ can be calculated from Eq. (23) and finally z_c is obtained from Eq. (18) as

$$z_c = \frac{\overline{q} - q}{\gamma} \geq 0 \qquad (24)$$

In the static case, when β=0, the plastic critical depth can be computed without trial and error. When $\psi_f \geq \psi_0$, and for the static case, the results of this paper are the same as those of Peng and Chen [13].

3 RESULTS

Based on the algorithm described in the previous section, a computer code was prepared. In this part of the paper different parametric analyses were made for the plastic critical depth, and the results were compared to the results of the other studies.

In the static case (k_h=k_v=0) and for δ_w=c_w=θ=β=0, the solution leads to the following equation, which is the simple Rankin formula for the plastic critical depth

$$z_c = \frac{2c}{\gamma}\tan\left(\frac{\pi}{4} + \frac{\phi}{2}\right) - \frac{q}{\gamma} \qquad (25)$$

Nian and Han [4] developed the Rankin theory to calculate the seismic active lateral earth pressure. They neglected the friction angle and the adhesion of the soil-wall interface and assumed that the wall is vertical (i.e., δ_w=c_w=θ=0). Their equation for z_c is

$$z_c = \frac{2c\left(\sin\phi\left(1 - \tan\beta\tan\delta\right) + \sqrt{\left(1 - \tan\beta\tan\delta\right)^2 + 4\tan^2\delta}\right)}{\gamma\left(1 - k_v\right)\cos\phi\left(\left(1 - \tan\beta\tan\delta\right)^2 + \dfrac{4\tan^2\delta}{\cos^2\phi}\right)} \qquad (26)$$

Also, Peng [3] developed the Mononobe-Okabe theory for the seismic case by taking into account the effect of the plastic critical depth and proposed the following equation to calculate $\overline{q}$

$$\overline{q}=\frac{c\cos(\theta-\beta)\cos\phi+c_w\sin(\alpha_a+\beta)\sin(\alpha_a+\theta-\phi)}{\sqrt{k_h{}^2+(1-k_v)^2}\cos(\alpha_a+\theta)\sin(\alpha_a-\phi-\delta)\cos\beta} \quad (27)$$

where

$$\tan\alpha_a=\frac{\sin(\phi+\delta-\theta)+m_0\sin\theta\cos\theta+\sqrt{1-m_0\cos(\theta+\phi+\delta)}}{\cos(\theta-\phi-\delta)+m_0\sin^2\theta}$$
$$m_0=\frac{c_w\cos(\beta+\delta)}{(c+c_w)\cos(\theta-\beta)\cos\phi} \quad (28)$$

In addition, α_a can also be calculated using the following equations:

$$\text{if}\quad c\cos(\theta-\beta)\cos\phi+c_w\sin(\phi+\beta+\delta)\sin(\theta+\delta)>0,\quad \text{then}$$
$$\tan\alpha_a=\frac{\sin(\phi+\delta-\theta)+n_0\sin(\phi+\delta)\cos(\phi+\delta)+\sqrt{1+n_0\cos(\theta+\phi+\delta)}}{\cos(\theta-\phi-\delta)+n_0\cos^2(\phi+\delta)}$$
$$n_0=\frac{c_w\cos(\beta+\delta)}{c\cos(\theta-\beta)\cos\phi+c_w\sin(\phi+\beta+\delta)\sin(\theta+\delta)} \quad (29)$$
$$\text{if}\quad c\cos(\theta-\beta)\cos\phi+c_w\sin(\phi+\beta+\delta)\sin(\theta+\delta)=0,\quad \text{then}\ \alpha_a=\phi+\delta$$

A comparison of the results of this paper with the results of the other methods is shown in Table 2. The percentage relative errors between the results of this paper and the other methods are shown in the table as well. In the last row of the table the average percentage errors for all the cases are written. It is clear that the least and the most errors belong to Peng's limit-equilibrium method [3] (average error 3%) and Eq. (25) (average error 38%), respectively. In addition, the depths computed from the stress-characteristics method are lower than those of the other methods.

In the static case and for q=θ=0, a comparison was made between the results of this study for z_c and those of others, as shown in Figure 5. In this case the results of Eq. (25), Nian and Han [4] and Iskander et al. [5] are the same. It is clear that the results of this study are very close to Peng [3] (average difference is about 1.4%). Eq. (25) predicts smaller values of z_c (about 15% smaller) and also the results of Lin et al. [7] are about 29% smaller than the results in this paper.

To evaluate the effects of the parameters on the plastic critical depth, several parametric analyses were made. Figure 6 shows the effects of the pseudo-static horizontal (k_h) and vertical (k_v) coefficients on the plastic critical depth z_c. The horizontal axis is k_h and varies from -0.5 to 0.5. It is clear that z_c increases with an increase in k_h. When k_h is positive, its variation has more influence on increasing z_c. For example, if k_v=0, when k_h changes from 0 to -0.5, z_c decreases by about 58%, but when k_h changes from 0 to 0.5, the increase in z_c is about 93%. These differences in the negative values of k_v are less than those of the positive values.

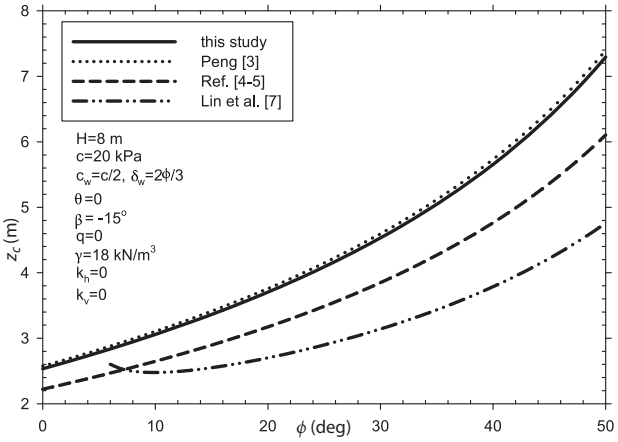

Figure 5. A comparison between the results of this study and those of others.

Table 2. Comparison of the results of this study with other methods. (θ=-10º, β=0, δ_w=ϕ/2, c_w=0.5c, k_h=-0.2, k_v=0.1, γ=18 kN/m^3).

ϕ (deg)	c (kPa)	q (kPa)	z_c (m)					Absolute relative error (%)			
			Ma et al. 2012, [6]	Eq. (25)	Nian & Han, 2013, [4]	Peng, 2012,[3]	This study	Ma et al. 2012, [6]	Eq. (25)	Nian & Han, 2013, [4]	Peng, 2012, [3]
20	0	10	0	0	0	0	0	0	0	0	0
20	10	0	1.424	1.592	1.315	1.224	1.206	15	24	8	1
20	10	10	0.904	1.032	0.759	0.668	0.651	28	37	14	3
40	10	0	1.68	2.384	1.837	1.442	1.382	18	42	25	4
40	10	10	1.168	1.832	1.281	0.886	0.826	29	55	36	7
20	20	0	2.6	3.168	2.629	2.447	2.412	7	24	8	1
20	20	10	2.072	2.624	2.074	1.892	1.857	10	29	10	2
40	20	0	3.048	4.768	3.674	2.884	2.764	9	42	25	4
40	20	10	2.52	4.208	3.118	2.328	2.208	12	48	29	5
Average error:								16	38	19	3

Also, increasing k_v leads to an increase in z_c. Similar to k_h, when k_v is positive, the variations are more rapid. The average changes in z_c for k_v= -0.5 relative to k_v=0 are about 22% and 40% in the negative and positive values of k_h, respectively. These changes for k_v=0.5 relative to k_v=0 are 39% and 144% in the negative and positive values of k_h, respectively.

The results of Peng [3] are also shown in Figure 6. It is clear that the values of results of this study are lower than those of Peng. For the selected parameters shown in the figure, the average relative errors between these two methods are 1% for the positive values of k_h and k_v and 30% for the negative values of k_h and k_v.

The effects of the soil friction angle (ϕ) and ground-surface slope angle (β) values on z_c are shown in Figure 7. It is clear that z_c increases with an increase in ϕ. The results of the analyses indicate that the soil-wall interface friction angle (δ_w) has very little influence on z_c and its effect can be ignored.

Increasing β leads to an increase in the plastic critical depth. When β changes from -30º to 30º, z_c increases by about 17%.

Figure 8 shows the influence of the soil cohesion and soil-wall interface adhesion on z_c. The horizontal axis is the soil cohesion (c) and several graphs have been plotted for different values of c_w/c. It is obvious that by increasing c, the plastic critical depth increases. Increasing c_w/c also leads to an increase in z_c, but its influence is less than that of c. For the assumed parameters indicated in the figure, the difference between the results of c_w/c=0 and c_w/c=1 for all values of c is about 30%. The change of z_c with c is linear. The slope of this

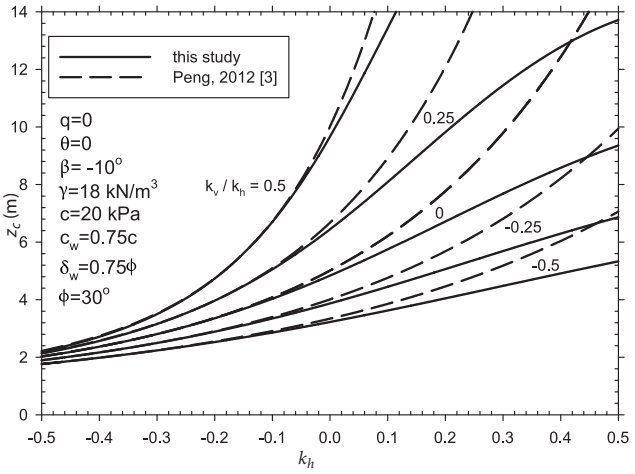

Figure 6. The effects of the k_h and k_v values on the plastic critical depth.

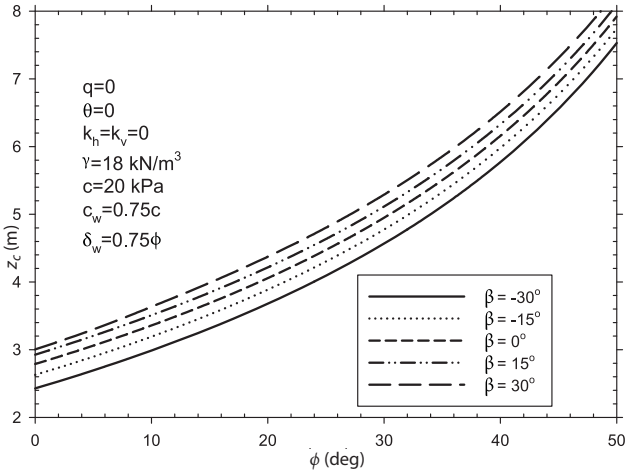

Figure 7. The effects of the ϕ and β values on the plastic critical depth.

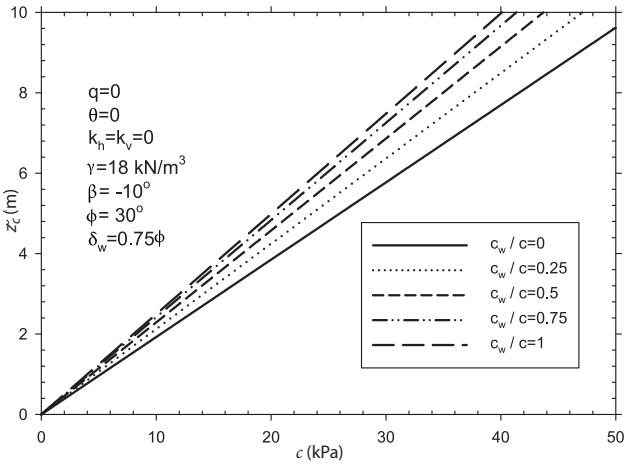

Figure 8. The effects of the c and c_w values on the plastic critical depth.

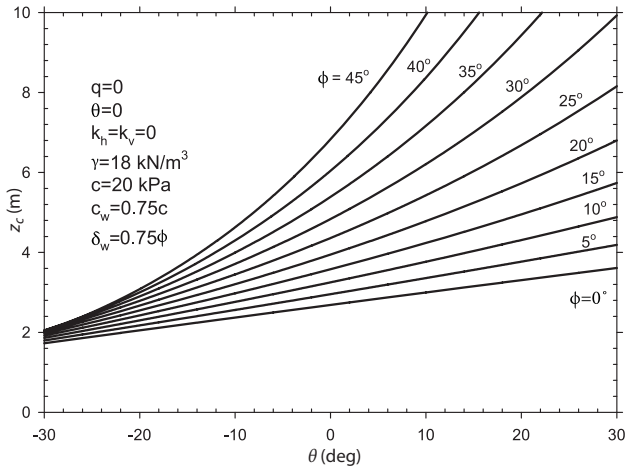

Figure 9. The effects of the θ values on the plastic critical depth.

line changes from 0.19 to 0.25 m/kPa when c_w/c changes from 0 to 1.

Figure 9 shows the influence of the wall angle (θ) on z_c. The horizontal axis shows the wall angle and changes from -30º to 30º. Different graphs have been plotted for different values of the soil friction angle. We can see that by increasing θ, the value of z_c increases. z_c varies more rapidly with θ for the larger values of ϕ. For example, when ϕ=45º, by increasing θ from -30º to 0, z_c increases by about 202%. This increase for ϕ=0, when changing θ from -30º to 0 it is about 55% and when changing θ from 0 to 30º it is about 34%.

4 CONCLUSIONS

The stress-characteristics method has been used to evaluate the plastic critical depth. The most important conclusions from this study are:

- The values of the results of the stress-characteristics method described in this paper for the plastic critical depth, z_c, are smaller than those of the pseudo--dynamic [6], modified Rankin [4] and modified Mononobe-Okabe [3] methods and are closer to the modified Mononobe-Okabe method. The method of Lin et al. [7] under predicts the plastic critical depth.
- Increasing the horizontal and vertical pseudo-static coefficients (based on their assumed directions) can increase z_c. The percentage changes relative to the static case can be more than 100%.
- The values of z_c increase with an increase in the soil friction angle, but the soil-wall interface friction angle has very little influence on z_c and can be ignored.
- For the assumed direction of the ground-surface angle β, by increasing it, z_c increases. For the sample parameters selected in this paper, by changing β from -30º to 30º, the average increase in z_c is about 17%.
- The cohesion of the soil (c) has a considerable effect on z_c. The variation of z_c with c is linear. The slope of this line increases with an increase in c_w/c.
- Increasing the wall angle (for the assumed direction of this study) leads to an increase in z_c. This effect is greater for larger values of ϕ. The influence of θ on z_c is more than that of β.

Acknowledgements

The author would like to thank the reviewer for very valuable comments and suggestions that were helpful in developing the paper.

REFERENCES

[1] Shukla, S.K., Gupta, S.K., Sivakugan, N. 2009. Active earth pressure on retaining wall for c-ϕ soil backfill under seismic loading condition, Journal of Geotechnical and Geoenvironmental Engineering 135, 5, 690-696.

[2] Peng, M.X. 2010. Analytical solution of plastic critical depth for active earth pressure on retaining wall (in Chinese), Rock and Soil Mechanics 13, 10, 3179-3183.

[3] Peng, M.X. 2012. Coulomb's solution to seismic active earth pressure on retaining walls, Chinese Journal of Rock Mechanics and Engineering 31, 3, 640-648.

[4] Nian, T., Han, J. 2013. Analytical solution for Rankine's seismic active earth pressure in c-ϕ soil with infinite slope, Journal of Geotechnical and Geoenvironmental Engineering 139, 9, 1611-1616.

[5] Iskander, M., Chen, Z., Omidvar, M., Guzman, I., Elsherif, O. 2013. Active static and seismic earth pressure for c–ϕ soils, Soils and Foundations 53, 5, 639-652.

[6] Ma, S.J., Wang, K.H., Wu, W.B. 2012. Pseudo-dynamic active earth pressure behind retaining wall for cohesive soil backfill, Journal of Central South University 19, 11, 3298-3304.

[7] Lin, Y.L., Leng, W.M., Yang, G.L., Zhao, L.H., Li, L., Yang, J.S. 2015. Seismic active earth pressure of cohesive-frictional soil on retaining wall based on a slice analysis method, Soil Dynamics and Earthquake Engineering 70, 133-147.

[8] Sokolovskii, V.V. 1960. Statics of soil media, London, UK: Butterworth.

[9] Sokolovskii, V.V. 1965. Statics of granular media, Oxford, UK: Pergamon Press.

[10] Reece, A., Hettiaratchi, D. 1989. A slip-line method for estimating passive earth pressure, Journal of Agricultural Engineering Research 42, 1, 27-41.

[11] Kumar, J., Chitikela, S. 2002. Seismic passive earth pressure coefficients using the method of characteristics, Canadian Geotechnical Journal 39, 2, 463-471.

[12] Cheng, Y. 2003. Seismic lateral earth pressure coefficients for c-ϕ soils by slip line method, Computers and Geotechnics 30, 8, 661-670.

[13] Peng, M.X., Chen, J. 2013. Slip-line solution to active earth pressure on retaining walls, Geotechnique 63, 12, 1008-1019.

[14] Jahanandish, M., Keshavarz, A. 2005. Seismic bearing capacity of foundations on reinforced soil slopes, Geotextiles and Geomembranes 23, 1, 1-25.

[15] Keshavarz, A., Jahanandish, M., Ghahramani, A. 2011. Seismic bearing capacity analysis of rein-

forced soils by the method of stress characteristics, Iranian Journal of Science and Technology, Transaction of Civil Engineering 35, C2, 185-197.

[16] Anvar, S.A., Ghahramani, A. 1997. Equilibrium equations on zero extension lines and their application to soil engineering, Iranian Journal of Science and Technology, Transaction B-Engineering 21, 1, 11-34.

[17] Lee, I.K., Herington, J.R. 1972. A theoretical study of the pressures acting on a rigid wall by a sloping earth or rock fill, Geotechnique 22, 1, 1-26.

[18] Liu, F.Q., Wang, J. H. 2008. A generalized slip line solution to the active earth pressure on circular retaining walls, Computers and Geotechnics 35, 2, 155-164.

MIKRO ODZIVI ZRNATIH MATERIALOV PRI RAZLIČNIH VERTIKALNIH TLAKIH Z UPORABO METODE DISKRETNIH ELEMENTOV

Md. Mahmud Sazzad
Rajshahi University of Engineering & Technology,
Department of Civil Engineering
Rajshahi-6204, Bangladeš
E-pošta: mmsruet@gmail.com

Ključne besede

mikrostrukture, vertikalni pritisk, tekstura, mikro topologija, usklajevalno število, makro-mikro odnos

Izvleček

Z uporabo metode diskretnih elementov (DEM) so na sestavljenih ovalih potekali dvoosni tlačni preizkusi, s katerimi so se preučevali odzivi zrnatih materialov na mikro ravni pri različnih vertikalnih tlakih. Numerični vzorci so bili sestavljeni iz 8450 ovalov v pravokotnem okvirju brez prekrivanja. Pripravljeni so bili štirje vzorci različne gostote iz začetno ustvarjenega razstresenega vzorca pri različnih vertikalnih tlakih. Rezultati simulacij podajajo napetostno-deformacijsko-dilatacijsko obnašanje, podobno kot pri opazovanih peskih pri različnih vertikalnih tlakih. Ugotovljen je bil razvoj različnih mikro-parametrov in njihovih medsebojnih odnosov. Ko je vertikalni tlak razmeroma visok, je razlika med koordinacijskim številom in učinkovitim koordinacijskim številom zelo majhna; vendar pa je razlika očitna za nizki vertikalni tlak. Opisana je tudi mikro topologija zrnatega sestava za več pomembnih stanj prestriga. Omeniti je potrebno, da je topološka razporeditev zrnatih materialov odvisna od vertikalnih tlakov. Normalizirano število praznih por je minimalno pri najnižjem vertikalnem tlaku, medtem ko je enako število največje pri najvišjem vertikalnem tlaku. Linearno razmerje je opaziti med normaliziranim številom praznih por in učinkovitim koordinacijskim številom, ne glede na vertikalne tlake. Merjen je razvoj deviatorične teksture za različne vertikalne tlake in predstavljen makro-mikro odnos.

MICRO-SCALE RESPONSES OF GRANULAR MATERIALS UNDER DIFFERENT CONFINING PRESSURES USING THE DISCRETE ELEMENT METHOD

Md. Mahmud Sazzad
Rajshahi University of Engineering & Technology,
Department of Civil Engineering
Rajshahi-6204, Bangladesh
E-mail: mmsruet@gmail.com

Keywords

microstructures, confining pressure, fabric, microtopology, coordination number, macro-micro relationship

Abstract

Biaxial compression tests were carried out on assemblies of ovals to study the micro-scale responses of granular materials under different confining pressures using the discrete element method (DEM). A total of 8450 ovals were generated in a rectangular frame without any overlap. Four dense samples were prepared from the initially generated sparse sample under different confining pressures. The simulated results yield a stress-strain-dilatancy behaviour similar to that observed in sands under different confining pressures. The evolution of the different micro-parameters and their inter-relationships are established. When the confining pressure is relatively high, the difference between the coordination number and the effective coordination number is very small; however, the difference is apparent for a low confining pressure. The microtopology of the granular assembly at several important states of shear is also reported. It is noted that the topological distribution of the granular materials is confining-pressure dependent. The normalized void-cell number is a minimum under the lowest confining pressure, whereas the same number is a maximum under the highest confining pressure. A linear relationship is observed between the normalized void-cell number and the effective coordination number, regardless of the confining pressures. The evolution of the deviatoric fabric for different confining pressures is measured and the macro-micro relationship is presented.

1 INTRODUCTION

The responses of granular materials are greatly influenced by the confining pressure. This is evident from numerous experimental studies [1-8]. These studies, in general, indicated that the deviatoric stress increases or the angle of the internal friction, $\phi = \sin^{-1}\left[(\sigma_1 - \sigma_2)/(\sigma_1 + \sigma_2)\right]$, decreases with an increase of the confining pressure, where σ_1 and σ_2 are the stresses in the x_1- and x_2-directions, respectively. For example, Fukushima and Tatsuoka [2] considered extremely low to high confining pressures (5–400 kPa) in triaxial compression tests and indicated that ϕ does not change a great deal when the confining pressure is low and the change is apparent when the confining pressures are relatively higher. In a similar study, Tatsuoka et al. [3] conducted a series of drained plane-strain compression tests under confining pressures of 4.9 to 392 kPa considering the variation of bedding angles and reported that the dependency of ϕ is very small when the confining pressure is lower than 50 kPa. Nevertheless, these characterizations have been made from experimental studies based on macroscopic measurements where the micro-scale information is not known. To explore the microscopic responses for different confining pressures, the discrete element method (DEM) [9] can be used. Only a few studies considering the confining pressures using DEM have been reported in the literature. Mirghasemi et al. [10] studied the

effects of confining pressures on the shear strength and dilatancy of simulated rockfill using DEM and demonstrated that the simulated stress-dilatancy behaviour is similar to data obtained from experiments on rockfills. Sitharam [11] studied the effect of confining pressures on the micro-scale responses using DEM and indicated that the increase in the average coordination number and the accompanying decrease in the fabric anisotropy reduce the shear strength at higher confining pressures. It is important to understand the micro-scale information, even from a simpler simulation using DEM, before using this knowledge to develop physically sound continuum models. The objectives of the present paper are: (i) to simulate the macro-mechanical responses of assemblies of oval particles under different confining pressures (0–100 kPa) using DEM and (ii) to carry out a comprehensive study in order to explore the evolution of different micro-quantities under different confining pressures using DEM.

2 NUMERICAL EXPERIMENTS

In this section, the numerical method used in the simulation, the sample-preparation procedures using ovals and the simulation of the biaxial compression tests are briefly discussed.

2.1 Brief overview of DEM

The numerical simulations were carried out using DEM. The basic idea in DEM is simple. Each particle in DEM can make and break contacts with its neighbours. The accelerations of a particle are computed using Newton's second law of motion, as follows:

$$m\ddot{x}_i = \sum f_i \quad i = 1,2 \quad , \qquad (1)$$

$$I\ddot{\theta} = \sum M \quad , \qquad (2)$$

where m is the mass, $\ddot{x}_i$ are the translational acceleration components, f_i are the force components, I is the moment of inertia, $\ddot{\theta}$ is the rotational acceleration and M is the moment of a particle. The velocities and displacements are obtained by integrating the accelerations over time. The increments of the normal and shear displacements are computed by comparing the two successive time increments and used in the force-displacement law to obtain the increments of the normal and shear forces as follows:

$$\Delta f^n = k_n \Delta u_n, \quad \Delta f^s = k_s \Delta u_s, \qquad (3)$$

where k_n and k_s are the normal and shear contact stiffnesses, respectively. Slipping between particles occurs as soon as the following condition is satisfied:

$$\left| f^s \right| \geq f^n \tan\phi_\mu \quad , \qquad (4)$$

where ϕ_μ is the interparticle friction angle, f^n is the normal force and f^s is the shear force.

2.2 Sample preparation

Numerical samples consisting of 8450 ovals in eleven different sizes (i.e., widths) ranging from 1 to 2 mm were prepared. A schematic diagram of an oval with reference axes is shown in Fig. 1. In the present simulation the computer program OVAL [12] is used. In OVAL, a simple contact model consisting of two linear springs in the normal and tangential directions is incorporated. The initial sample was created by randomly placing the ovals (height-to-width ratio of 0.60) on grids of a rectangular frame with no contact. The initial sample generated at this stage was very loose. This sample was then compacted isotropically with 15, 25, 50 and 100 kPa in different stages using the periodic boundaries, a boundary condition in which the periodic cells are surrounded by identical cells. A particle that sits astride a periodic boundary has a numerical image on the opposite boundary. A deformation rate tensor is used to apply the global deformation uniformly. The interparticle friction coefficient, defined as $\mu = \tan\phi_\mu$, was intentionally turned off (set to zero) during the isotropic compaction to densify the assembly. When the target confining stress was reached, setting μ to zero in different stages during the isotropic compression, the sample was allowed to adjust with μ equal to 0.5 for a few steps before the start of the simulation. Then, μ was set to 0.50 [25] during the simulation of biaxial compression tests for all the confining pressures. An isotropically compressed dense sample compacted with 100 kPa with reference axes is shown in Fig. 2. The void ratio of the sample after the isotropic compression for different confining pressures was the same (0.126).

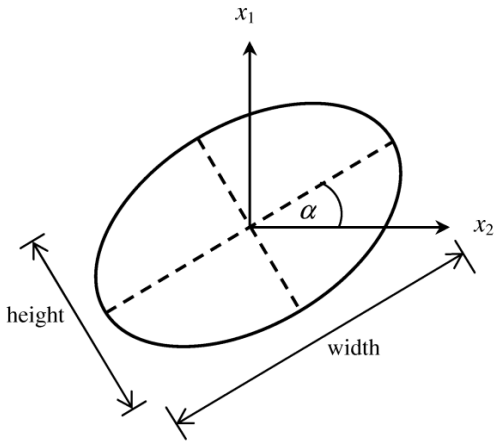

Figure 1. Schematic diagram of an oval with an inclination angle α.

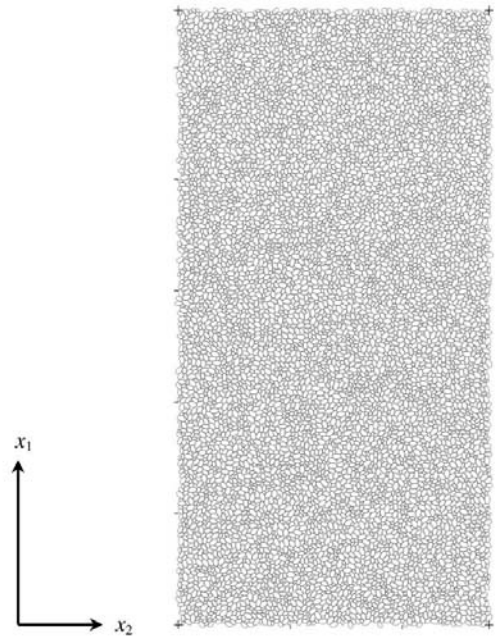

Figure 2. Isotropically compressed dense sample compressed to 100 kPa with reference axes.

2.3 Simulation of a biaxial compression test

Simulations of drained biaxial compression tests were performed using the strain-control condition. During shear, the sample height decreased vertically with a very small strain increment of 0.00002% in each step by keeping the stress in the lateral direction constant (i.e., 15 or 25 or 50 or 100 kPa, whichever applicable). The parameters used in the simulations are presented in Table 1. Note that the coefficients of global-type viscous damping used in the present study (Table 1) are maintained sufficiently small to keep the effect of the numerical damping to a minimum and to provide more stable solutions. The quasi-static condition during the simulation was examined by monitoring a non-dimensional index, I_{uf}, defined as follows [13]:

$$I_{uf} = \sqrt{\frac{\sum_{1}^{N_p}(unbalanced\ \ forces)^2 / N_p}{\frac{1}{\sum_{1}^{N_c}(contact\ \ forces)^2 / N_c}}} \times 100(\%)\,, \qquad (5)$$

where N_p and N_c are the numbers of particles and contacts, respectively. The unbalanced force in Eq. (5) is the resulting force acting on a particle. Lower values of I_{uf} are desirable because they are associated with a higher simulation accuracy [13] and indicative of the lowest effect of numerical damping. In the present study, I_{uf} remains reasonably small (the average value is less than 0.4%) during shear, regardless of the confining pressures.

Table 1. DEM Parameters used in the simulations

DEM parameters	Value
Normal contact stiffness, k_n (N/m)	1×10^8
Shear contact stiffness, k_s (N/m)	1×10^8
Mass density (kg/m^3)	2650
Increment of time step (s)	1×10^{-6}
Interparticle friction coefficient, μ	0.50
Damping coefficients	0.05

3 MACRO-MECHANICAL RESPONSES

Fig. 3(a) shows the relationship between the deviatoric stress, $q = (\sigma_1 - \sigma_2)/2$, and the axial strain, ε_1, while Fig. 3(b) shows the relationship between q/p and ε_1 for different confining pressures, ranging from 15 to 100 kPa. Here, the mean stress, $p = (\sigma_1 + \sigma_2)/2$. Note that q increases with an increase in the confining pressures. The classic behaviour of granular materials such as sand

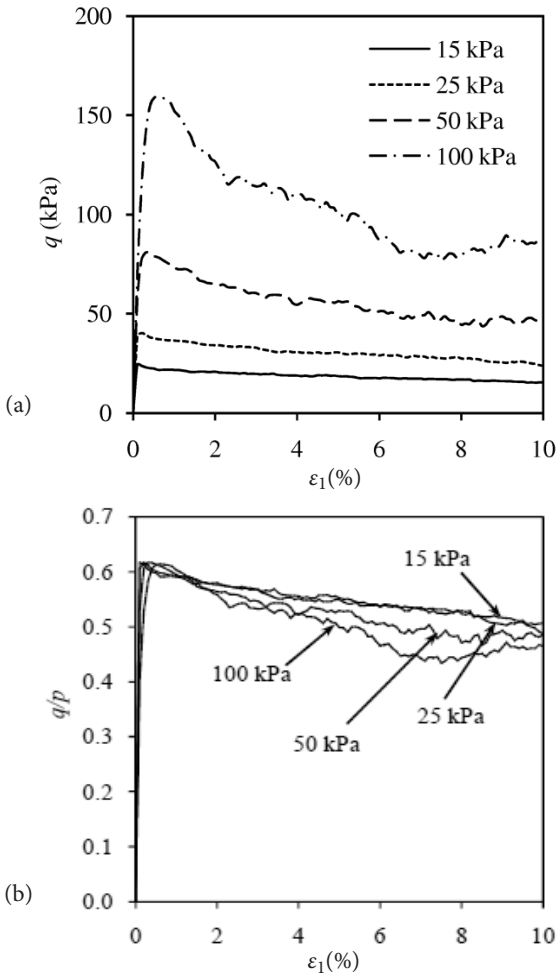

Figure 3. (a) Relationship between q and ε_1; (b) q/p and ε_1 for different confining pressures.

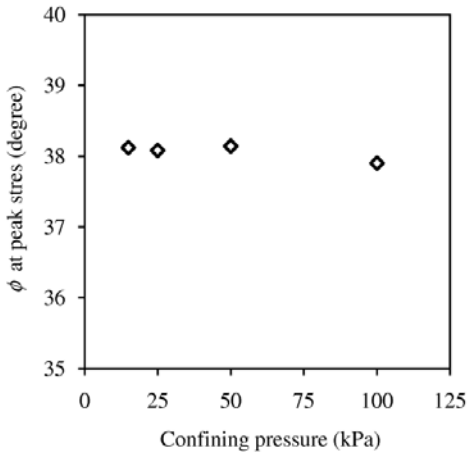

Figure 4. Relationship between ϕ at the peak stress state and the confining pressure.

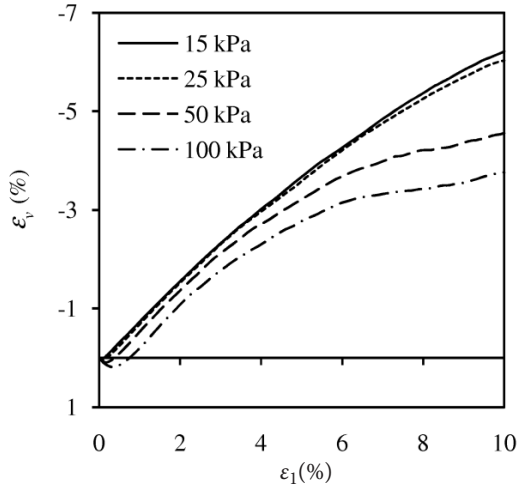

Figure 5. Relationship between ε_v and ε_1 for different confining pressures.

for a dense sample under plane-strain conditions (i.e., hardening is followed by softening) is observed. The relationship between ϕ at the peak stress and the confining pressure is shown in Fig. 4. Note that the change in ϕ at the peak stress is negligible when the confining pressure is lower than 50 kPa. Above a confining pressure of 50 kPa, very little decrease in ϕ is observed. The simulated behaviour reported in Fig. 4 is qualitatively the same as that reported by Tatsuoka et al. [3] for plane-strain compression and Fukushima and Tatsuoka [2] for a triaxial compression test using Toyoura sand, in which it was found that the change ϕ with the confining pressure is very small when the confining pressure is lower than approximately 50 kPa. This confirms the ability of DEM to capture the real behaviour of sands qualitatively using ovals, even under very small confining pressures.

The relationship between the volumetric strain, ε_v, and ε_1 is shown in Fig. 5. ε_v is defined as $\varepsilon_v=dV/V$, where dV is the change in volume and V is the initial volume of the sample prior to the shear. A positive value of ε_v denotes compression, while a negative value denotes dilation. Note that the dilation is suppressed as the confining pressure increases. The sample exhibits only little compression at small strains for a confining pressure of 100 kPa (maximum one), which is followed by a huge dilation. In contrast, the sample exhibits dilation from the beginning of the shear for a confining pressure of 15 kPa (minimum one) due to the lower lateral confinement. Note also that the evolution of ε_v is almost the same for relatively lower values of the confining pressures (i.e., 15 and 25 kPa), which is the same as reported in Tatsuoka et al. [3]. The relationship between the dilatancy index, $DI=-d\varepsilon_v/d\varepsilon_1$, and ε_1 is shown in Fig. 6 for different confining pressures, where $d\varepsilon_v$ is the change in ε_v and $d\varepsilon_1$ is the change in ε_1. Note that the relationship is dependent on the confining pressures even for a small strain.

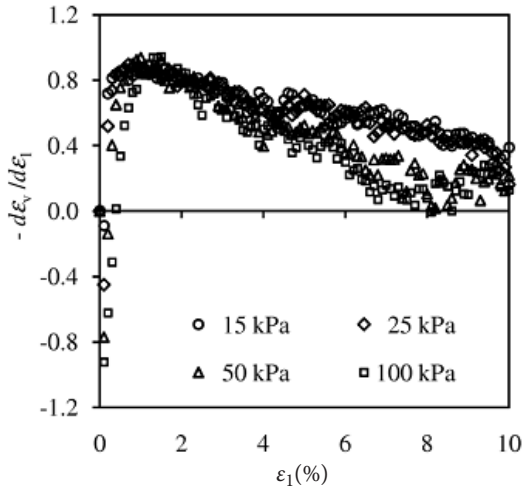

Figure 6. Evolution of dilatancy index $-d\varepsilon_v/d\varepsilon_1$ with ε_1 for different confining pressures.

4 MICRO-MECHANICAL RESPONSES

In this section the evolution of different micro-parameters such as the coordination number, the effective coordination number and the slip coordination number and their inter-relationship are presented.

4.1 Coordination number

The change in the coordination number, Z, as a function of ε_1 is shown in Fig. 7. Z is defined as follows [16]:

$$Z=\frac{2N_c}{N_p} \qquad (6)$$

A considerable reduction in Z is observed for the initial stage of the simulation due to the reshuffling of the initial fabric regardless of the confining pressures. The

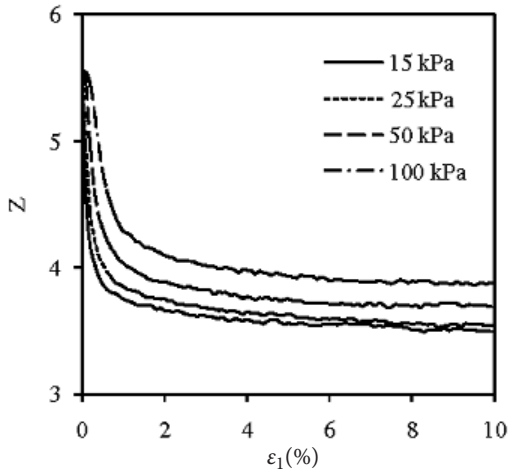

Figure 7. Evolution of Z as a function of ε_1 for different confining pressures.

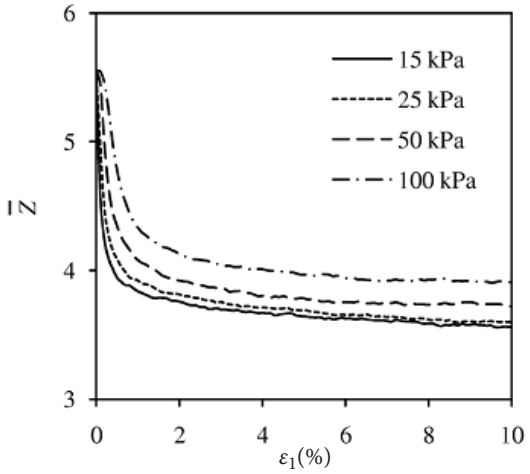

Figure 8. Evolution of $\bar{Z}$ as a function of ε_1 for different confining pressures.

behaviour is similar to that observed in other DEM studies [11, 14]. The reduction in Z is the highest for the lowest confining pressure. This is directly linked to the higher dilation under lower confining pressures, as is clear in Fig. 5. The lateral boundaries for lower confining pressures (i.e., 15 and 25 kPa) have less restriction to move outward from the sample, causing relatively more disintegration of the contacts in the lateral direction.

4.2 Effective coordination number

The effective coordination number is defined by considering the particles that effectively participate in the load-bearing framework, as reported in Kuhn [15]. The non-participating particles are neglected in computing the effective coordination number. The effective coordination number is defined in a similar way to the coordination number, as follows [15-16]:

$$\bar{Z} = \frac{2\bar{N}_c}{\bar{N}_p} \qquad (7)$$

where $\bar{N}_c$ and $\bar{N}_p$ are the total number of contacts and particles, respectively, that share in the effective load-bearing framework. The change in $\bar{Z}$ as a function of ε_1 is shown in Fig. 8. Note that the behaviour of $\bar{Z}$ is similar to that of Z. A comparison between Z and $\bar{Z}$ for confining pressures of 15 kPa and 100 kPa is shown in Fig. 9 to show their relative importance and comparable evolution during shear.

Note that the evolution of $\bar{Z}$ is higher than Z for both the confining pressures, even though their initial values are same. This indicates that the number of non-participating particles increases with the increase of ε_1 during shear. Note also that the difference between $\bar{Z}$ and Z is higher for a confining pressure of 15 kPa than for 100 kPa.

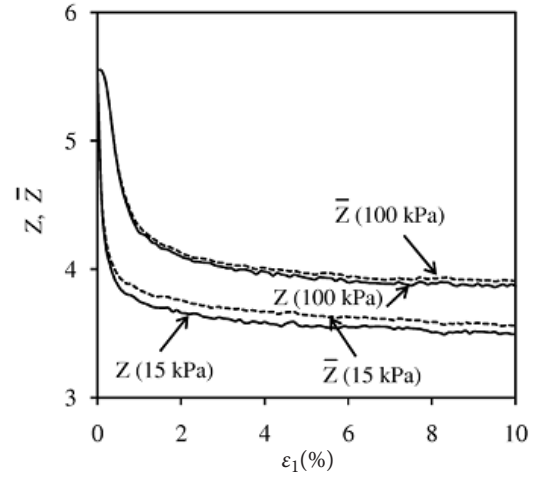

Figure 9. A comparison between Z and $\bar{Z}$ for confining pressures of 15 and 100 kPa.

4.3 Slip coordination number

The slip coordination number can be defined in a similar way to the coordination number, as follows [16]:

$$S = \frac{2N_{sl}}{N_p}, \qquad (8)$$

where N_{sl} is the total number of sliding contacts. The change in S as a function of ε_1 is shown in Fig. 10. Note that S reduces rapidly after an initial increase up to the peak, regardless of the confining pressures. The reduction is greater for a confining pressure of 100 kPa than for 15 kPa. Note also that the evolution of S has no similarity with Z and $\bar{Z}$ up to the peak stress.

4.4 Microtopology

The topological distribution of a granular system can be represented as a planar graph by connecting the branch

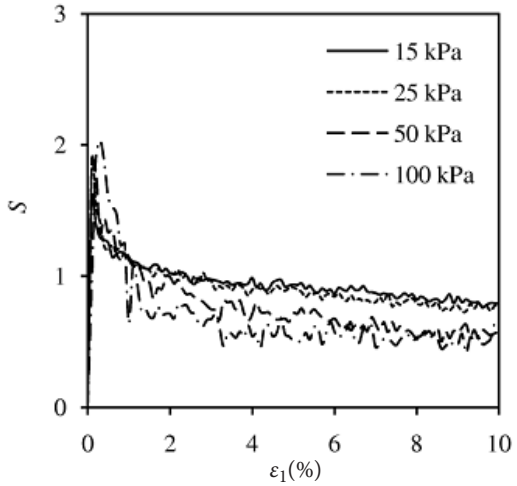

Figure 10. Evolution of S as a function of ε_1 for different confining pressures.

vectors of those particles that effectively participate in the load-bearing framework. Such a topological distribution of a granular assembly, considering only the effective contacts and particles, was proposed by Kuhn [15]. All sorts of non-participating particles are neglected in the planar graph in which each polygonal micro-domain is referred to as a void cell.

Following the same approach as reported in Kuhn [15], the topological distributions of granular materials in the initial state prior to shear (ε_1=0), at the peak stress state and at large strain (ε_1=10%) for confining pressures of 15 and100 kPa are shown in Fig.11. The number of void cells is a maximum at zero strain, indicating a compact contact network for the initial state of the simulation prior to shear. The sizes of the void cells are also smaller at this stage. When the deformation starts, the number

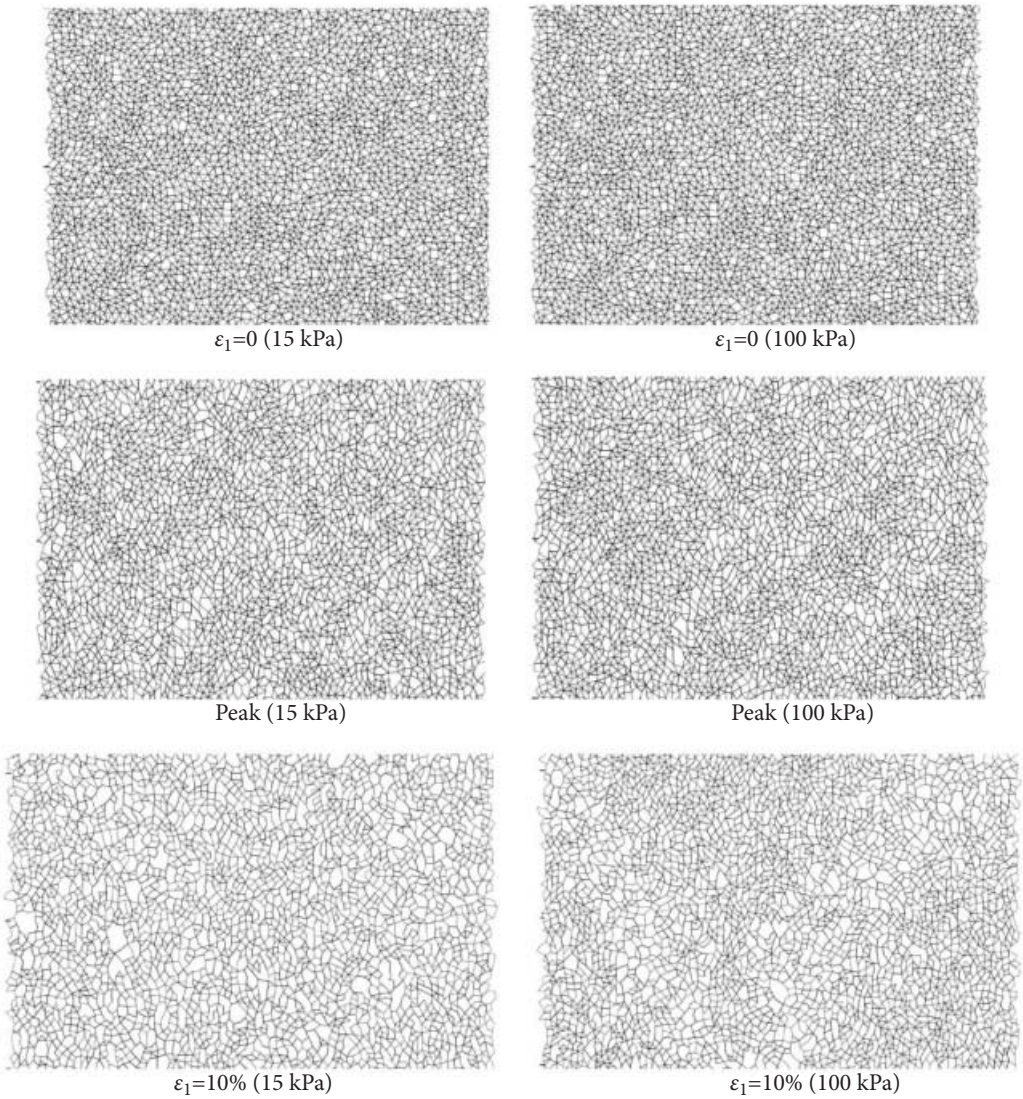

Figure 11. Snapshots of the topological distributions of granular materials at ε_1=0, at the peak stress state and ε_1=10% for confining pressures of 15 and 100 kPa.

of void cells starts decreasing and the size of the void cells starts getting larger. At the peak stress state, the distributions of the void cells reshuffle and the change is apparent. Many void cells become elongated, almost parallel to the x_1-direction due to the disintegration of contacts in the x_2-direction. In addition, large voids are observed in several regions. The number of void cells continuously decreases and the size of the void cells further increases as the deformation continues.

Large voids are observed at ε_1=10% for a confining pressure of 100 kPa. The formation of large void cells in several regions is a consequence of excessive contact disintegration due to the rotation of the particles and the collapse of the force chains. Although the void cells appear to evolve in a similar way for all the confining pressures, the difference is evident in Fig. 12, where the

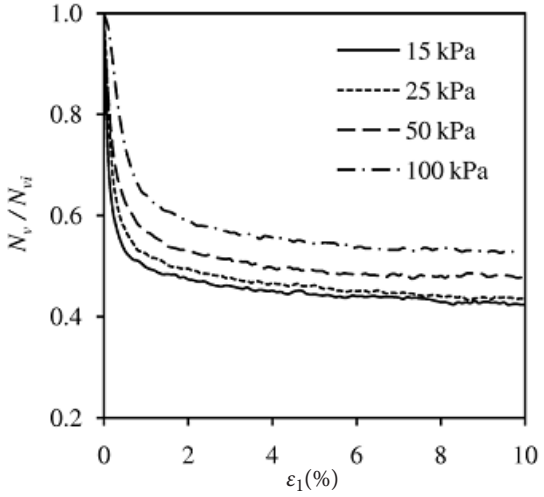

Figure 12. Relationship between N_v / N_{vi} and ε_1 for different confining pressures.

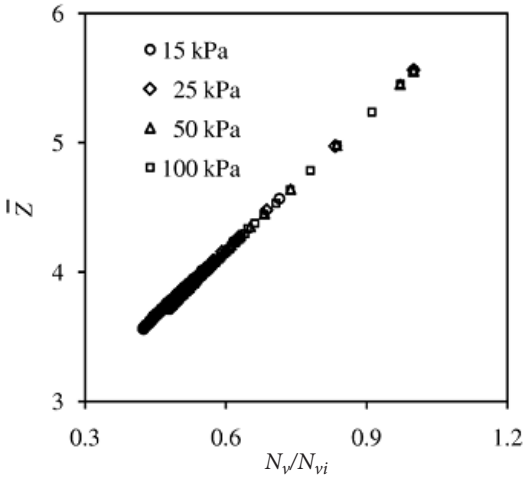

Figure 13. Relationship between $\overline{Z}$ and N_v / N_{vi} for different confining pressures.

number of void cells (N_v) is normalized by the initial number of void cells (N_{vi}) prior to shear (ε_1=0) and plotted against ε_1. Note that the normalized void-cell number is same at zero strain for all the confining pressures; however, it reduces as the deformation progresses. The minimum value N_v/N_{vi} is observed for a confining pressure of 15 kPa, whereas the maximum value is observed for a confining pressure of 100 kPa. The minimum number of N_v/N_{vi} for a confining pressure of 15 kPa is associated with the maximum dilation during shear. The relationship between $\overline{Z}$ and N_v/N_{vi} for different confining pressures is shown in Fig. 13.

The relationship between N_v/N_{vi} and $\overline{Z}$ regardless of the confining pressures can be mathematically expressed as follows:

$$\overline{Z} = 3.45\left(\frac{N_v}{N_{vi}}\right) + 2.1 \qquad (9)$$

4.5 Deviatoric fabric

The fabric in a granular system is highly disordered on the grain scale. The fabric is usually characterized by contact normals [17-19]. The fabric, H_{ij}, can be quantified in term of contact normals as follows [20]:

$$H_{ij} = \frac{1}{N_c}\sum_{\alpha=1}^{N_c} n_i^{\alpha} n_j^{\alpha} \qquad i,j = 1-2\ , \qquad (10)$$

where n_i^{α} is the i-th component of the unit contact normal at the α-th contact.

Further characterization of the contact normals based on the strong and weak contacts would be interesting [21-22]. In the present study, a contact is defined as strong if it carries a contact force (f) greater than the average contact force (f_a) and defined as weak if it carries a contact force smaller than, or equal to f_a. The average contact force is given by

$$f_a = \sqrt{\frac{\sum_{k=1}^{N_c} \left| f^k \right|^2}{N_c}} \qquad (11)$$

Two additional fabric tensors for strong and weak contacts can be defined similar to Eq. (10) as follows [22]:

$$H_{ij}^s = \frac{1}{N_c}\sum_{s=1}^{N_s} n_i^s n_j^s \qquad i,j = 1-2\ , \qquad (12)$$

$$H_{ij}^w = \frac{1}{N_c}\sum_{w=1}^{N_w} n_i^w n_j^w \qquad i,j = 1-2\ , \qquad (13)$$

where n_i^s and n_i^w are the i-th component of the unit contact normals for the s-th strong and w-th weak contact, respectively, N_s is the number of strong contacts, N_w is the number of weak contacts and $N_c = N_s + N_w$.

The evolution of the deviatoric fabric, $H_{11} - H_{22}$, for different confining pressures is shown in Fig. 14 as a function of ε_1. $H_{11} - H_{22}$ is zero at ε_1=0 and increases with ε_1 up to a peak, regardless of the confining pressures and reaches the same value at large strain. The evolution of the fabric anisotropy is dominant for the lowest confining pressures. The highest fabric anisotropy with the lowest confining pressures is associated with the highest dilatancy, as observed in Fig. 5. The dilatancy is suppressed by the increasing confining pressures resulting in the suppression of the fabric anisotropy.

Similar to $H_{11} - H_{22}$, the evolution of $H_{11}^s - H_{22}^s$ and $H_{11}^w - H_{22}^w$ as a function of ε_1 is also shown in Figs. 15(a)

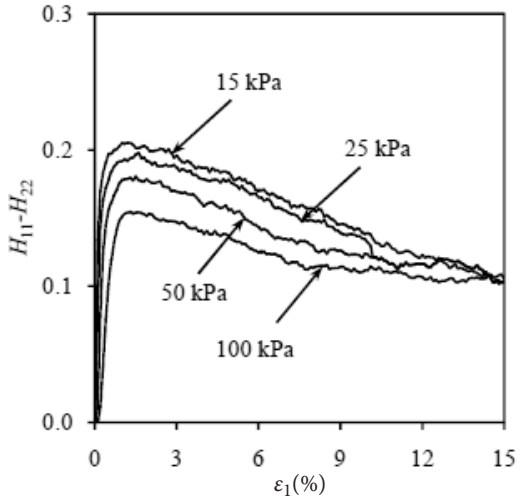

Figure 14. Evolution of $H_{11} - H_{22}$ as a function of ε_1 for different confining pressures.

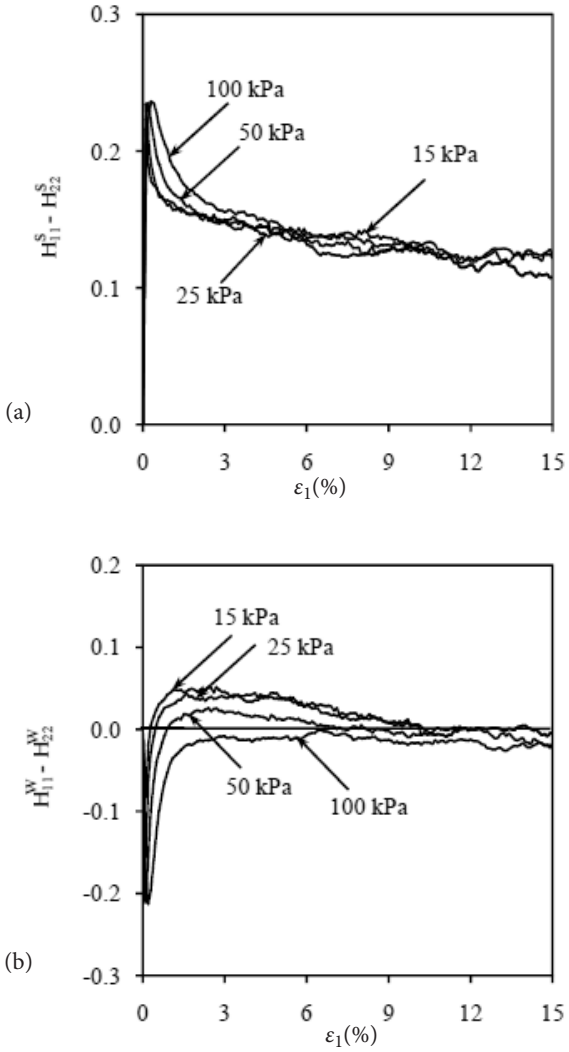

Figure 15. Relationship between a) $H_{11}^s - H_{22}^s$ versus ε_1 and b) $H_{11}^w - H_{22}^w$ versus ε_1 for different confining pressures.

and 15(b), respectively. $H_{11}^s - H_{22}^s$ peaks at a small strain. At a large strain, $H_{11}^s - H_{22}^s$ reaches almost the same value for different confining pressures. The evolution of $H_{11}^w - H_{22}^w$ is rather different from that of $H_{11}^s - H_{22}^s$. $H_{11}^w - H_{22}^w$ is opposite to $H_{11}^s - H_{22}^s$ near the peak, indicating a reverse fabric evolution of weak contacts, compared to strong contacts. However, $H_{11}^w - H_{22}^w$ approaches to positive values with the increase of ε_1. The phase-change point of $H_{11}^w - H_{22}^w$ from negative to positive is confining-pressure dependent. At large strain, $H_{11}^w - H_{22}^w$ also reaches the same value for different confining pressures.

4.6 Macro-micro relationship

Several approaches in the literature related to the macro-quantity (stress ratio) and the micro-quantity (fabric) computed using the single micro-parameter (contact normal) depending on the varieties of simulation conditions, such as particle shape, stress paths, sample density, etc. [14, 22, 23-24] were reported. These studies indicated that the micro-quantity relates strongly to the macro-quantity when the contact normal vectors of strong contacts are considered in quantifying the fabric tensors. These studies also observed a unique macro-micro relationship regardless of the conditions used in their studies. Following a similar approach, the relationship between q/p and $(H_{11} - H_{22})/(H_{11} + H_{22})$ at different confining pressures is shown in Fig. 16 (a), while the relationship between q/p and $(H_{11}^s - H_{22}^s)/(H_{11}^s + H_{22}^s)$ is shown in Fig. 16 (b).

Note that the relationship between q/p and $(H_{11} - H_{22})/(H_{11} + H_{22})$ is pressure dependent when all the contacts are considered. In contrast, q/p is almost equal to $(H_{11}^s - H_{22}^s)/(H_{11}^s + H_{22}^s)$ for relatively lower confining pressures (i.e., 15–50 kPa) when strong contacts are

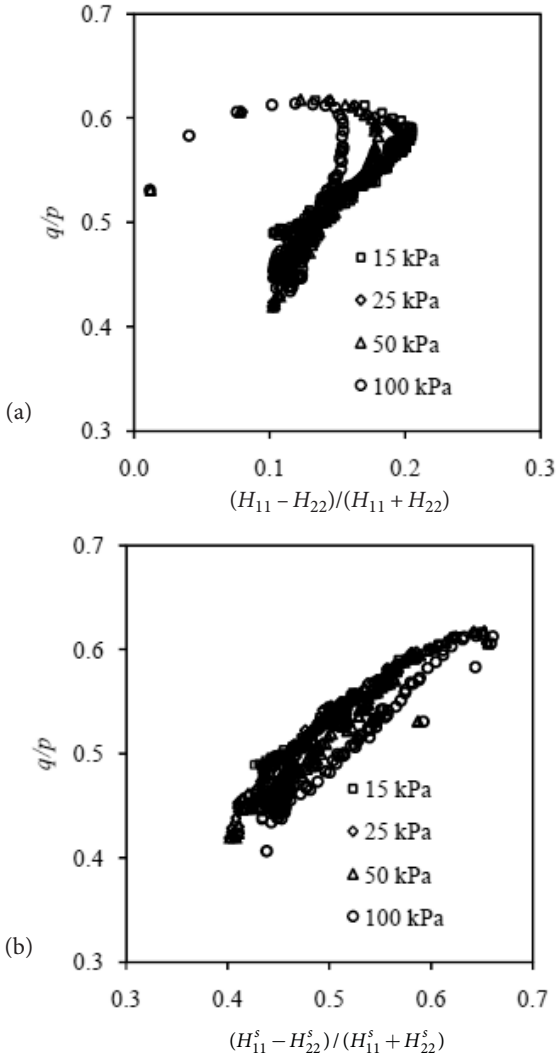

Figure 16. Relationship between a) q/p and $(H_{11} - H_{22})/(H_{11} + H_{22})$ versus ε_1 and b) q/p and $(H^s_{11} - H^s_{22})/(H^s_{11} + H^s_{22})$ for different confining pressures.

considered. Note also that a unique relationship, regardless of the confining pressures considered in the present study, is not available, even when strong contacts are considered in quantifying the fabric tensors.

5 CONCLUSIONS

A numerical simulation was carried out to investigate the evolution of microstructures under different confining pressures using the DEM. The simulated stress-strain-dilatancy behaviour is qualitatively similar to that observed in experimental studies using sands for different confining pressures. Different micro-parameters are measured and their inter-relationship is discussed. It is important to understand the evolution of these micro-parameters and their inter-relationship for different confining pressures, even from simpler simulations, before using this knowledge in developing physically sound and micro-mechanic-based continuum models. This micro-information may also be helpful for the comprehensive understanding of the complex behaviour of a granular system. Several interesting and important findings of this study are summarized below.

(i) The difference between the coordination number and the effective coordination number is very small when the confining pressure is relatively high; however, the difference is apparent when the confining pressure is very low.
(ii) The slip coordination number reduces sharply after an initial increase up to the peak stress, regardless of the confining pressures. At large strain, the slip coordination number under low confining pressures takes precedence over the larger confining pressures.
(iii) The topological distribution of granular materials is confining-pressure dependent. The minimum value for the normalized void-cell number is observed for the lowest confining pressure, whereas the maximum value is observed for the highest confining pressure.
(iv) A linear relationship between the normalized void-cell number and the effective coordination number is observed, regardless of the confining pressures.
(v) A single micro-parameter related to the contact normals of all the contacts is not sufficient to establish a unique macro-micro relationship between the stress ratio and the fabric ratio, regardless of the confining pressures.

REFERENCES

[1] Ponce, V.M., Bell, J.M. 1971. Shear strength of sand at extremely low pressures. J. SME Div, Proc of ASCE 97(SM4), pp. 625-638.
[2] Fukushima, S., Tatsuoka, F. 1984. Strength and deformation characteristics of saturated sand at extremely low pressures. Soils and Foundations 24, 4, 30-48.
[3] Tatsuoka, F., Sakamoto, M., Kawamura, F. 1986. Strength and deformation characteristics of sand in plane strain compression. Soils and Foundations 26, 1, 65-84.
[4] Yamamuro, J.A., Lade, P.V. 1996. Drained sand behavior in axisymmmetric tests at high pressures. Journal of Geotechnical Engineering 122, 2, 109-119.
[5] Yamamuro, J.A., Lade, P.V. 1997. Instability of granular materials at high pressures. Soils and Foundations 37, 1, 41-52.

[6] Alshibli, K.A., Batiste, S.N., Sture, S. 2003. Strain localization in sand: plane strain versus triaxial compression. Journal of Geotechnical and Geoenvironmental Engineering 129, 6, 483-494.
[7] Koseki, J., Yoshida, T., Sato, T. 2005. Liquefaction properties of toyoura sand in cyclic tortional shear tests under low confining stress. Soils and Foundations 45, 5, 103-113.
[8] Kumar, J., Madhusudhan, B.N. 2010. Effect of relative density and confining pressure on poisson ratio from bender and extender elements tests. Geotechnique 60, 7, 561–567.
[9] Cundall, P.A., Strack, O.D.L. 1979. A discrete numerical model for granular assemblies. Geotechnique 29, 1, 47-65.
[10] Mirghasemi, A.A., Rothenburg, L., Matyas, E.L. 1997. Numerical simulations of assemblies of two-dimensional polygon-shaped particles and effects of confining pressure on shear strength. Soils and Foundations 37, 3, 43-52.
[11] Sitharam, T.G. 1999. Micromechanical modeling of granular materials: effect of confining pressure on mechanical behavior. Mechanics of Materials 31, 10, 653-665.
[12] Kuhn, M.R. 2003. Smooth convex three-dimensional particle for the discrete element method. Journal of Engineering Mechanics 129, 5, 539-547.
[13] Ng, T.T. 2006. Input parameters of discrete element methods. Journal of Engineering Mechanics 132, 7, 723-729.
[14] Sazzad, M.M., Suzuki, K. 2012. A comparison between conventional triaxial and plane-strain compression on a particulate system using 3D DEM. Acta Geotechnica Slovenica 12, 2, 17-23.
[15] Kuhn, M.R. 1999. Structured deformation in granular materials. Mechanics of Materials 31, 6, 407-429.
[16] Sazzad, M.M. 2014. Micro-scale behavior of granular materials during cyclic loading. Particuology. doi:10.1016/j.partic.2013.12.005.
[17] Oda, M., Nemat-Nasser, S., Konishi, J. 1985. Stress-induced anisotropy in granular masses. Soils and Foundations 25, 3, 85-97.
[18] Nouguier-Lehon, C., Cambou, B., Vincens, E. 2003. Influence of particle shape and angularity on the behavior of granular materials: a numerical analysis. International Journal of Numerical Analytical Methods in Geomechanics 27, 14, 1207-1226.
[19] Sazzad, M.M., Suzuki, K. 2010. Micromechanical behavior of granular materials with inherent anisotropy under cyclic loading using 2D DEM. Granular Matter 12, 6, 597–605.
[20] Satake, M. 1982. Fabric tensor in granular materials. In Vermeer PA and Luger HJ (eds), Proc IUTAM Symposium on Deform Fail of Granular Materials, Delft, Balkema, pp. 63–68.
[21] Radjai, F., Wolf, D.E., Jean, M., Moreau, J.J. 1998. Bimodal character of stress transmission in granular packings. Physical Review Letter 80, 1, 61-64.
[22] Sazzad, M.M., Suzuki, K. 2013. Density dependent macro-micro behavior of granular materials in general triaxial loading for varying intermediate principal stress using DEM. Granular Matter 15, 5, 583–593.
[23] Antony, S.J. 2000. Evolution of force distribution in three-dimensional granular media. Physical Review E 63, 1, 1–13.
[24] Antony, S.J., Momoh, R.O., Kuhn, M.R. 2004. Micromechanical modelling of oval particulates subjected to bi-axial compression. Computation Material Science 29, 4, 494–498.
[25] Kuhn, M.R. 2003. Heterogeneity and patterning in the quasi-static behavior of granular materials. Granular Matter 4, 155–166.

TEMELJNA ŠTUDIJA O UČINKOVITOSTI NA MESTU IZDELANEGA SAMOSTOJNEGA BETONSKEGA PILOTA X PREREZA

Yu Wang
PLA University of Science and Technology,
State Key Laboratory of Disaster Prevention & Mitigation of Explosion & Impact
Nanjing 210007, Kitajska
E-pošta: lgdxwangyu@163.com

Yaru Lv
PLA University of Science and Technology,
State Key Laboratory of Disaster Prevention & Mitigation of Explosion & Impact
Nanjing 210007, Kitajska
E-pošta: yaru419828@163.com

Dongdong Zhang *(vodilni avtor)*
PLA University of Science and Technology,
College of Field Engineering
Nanjing 210007, Kitajska
E-pošta: zhangdodo_163@163.com

Jieying Zhou
PLA University of Science and Technology,
College of Defense Engineering
Nanjing 210007, Kitajska
E-pošta: zhoujieying666@126.com

Ključne besede

na mestu izdelan betonski pilot X prereza, terenski statični obremenilni preizkus, tridimenzionalni numerična povratna analiza, mehanizem prenosa napetosti, stranska odpornost, ločni efekt zemljine

Izvleček

Na mestu izdelani betonski piloti X prereza (XCC) se uporabljajo, ker imajo višjo nosilnost kot na mestu izdelani betonski piloti krožnega prereza (CCC) z enako površino prereza. Čeprav je bila preučevana nosilnost XCC pilotov, uspešnost samostojnih XCC pilotov, predvsem glede mehanizma prenosa napetosti v odvisnosti od geometrijskih učinkov, še vedno ni povsem jasna. V prispevku je podana primerjava terenskih statičnih obremenilnih preizkusov za XCC in CCC samostojna pilota z enako površino prečnega prereza. Za boljše razumevanje so bile dodatno izvedene tridimenzionalne numerične povratne analize. Izmerjeni in izračunani rezultati kažejo, da ima XCC samostojni pilot približno 25% višjo mejno nosilnost kot CCC samostojni pilot. To je zato, ker ima XCC samostojni pilot približno 20% višji skupni stranski odpor, ki je zaradi 60% večjega obsega prereza pilota in nekoliko manjše stranske odpornosti na enoto površine. V zemljini so se razvili bočni ločni učinki, ki povzročajo neenakomerno razporeditev efektivne normalne in strižne napetosti po obsegu XCC samostojnega pilota. Ugotovimo lahko, da imajo XCC samostojni piloti višjo učinkovitost z vidika privarčevanega materiala v primerjavi s CCC samostojnimi piloti.

A FUNDAMENTAL STUDY OF THE PERFORMANCE OF X-SECTION CAST-IN-PLACE CONCRETE SINGLE PILES

Yu Wang
PLA University of Science and Technology,
State Key Laboratory of Disaster Prevention & Mitigation of Explosion & Impact
Nanjing 210007, China
E-mail: lgdxwangyu@163.com

Yaru Lv
PLA University of Science and Technology,
State Key Laboratory of Disaster Prevention & Mitigation of Explosion & Impact
Nanjing 210007, China
E-mail: yaru419828@163.com

Dongdong Zhang *(corresponding author)*
PLA University of Science and Technology,
College of Field Engineering
Nanjing 210007, China
E-mail: zhangdodo_163@163.com

Jieying Zhou
PLA University of Science and Technology,
College of Defense Engineering
Nanjing 210007, China
E-mail: zhoujieying666@126.com

Keywords

X-section cast-in-place concrete pile, field static load test, three-dimensional numerical back-analysis, stress-transfer mechanism, side resistance, soil arching

Abstract

X-section cast-in-place concrete (XCC) piles are used because they have a higher bearing capacity than circular-section cast-in-place concrete (CCC) piles of the same cross-sectional area. Although the bearing capacity of XCC piles has been studied, the performance of XCC single piles, especially for the stress-transfer mechanism dependent on the geometrical effects, is still not fully understood. This paper reports two comparative field static load tests on an XCC and a CCC single pile of the same cross-sectional area. In addition, corresponding three-dimensional numerical back-analyses are performed to provide a fundamental understanding. The measured and computed results reveal that the XCC single pile has an approximately 25% higher ultimate bearing capacity than the CCC single pile. This is because the XCC single pile has an approximately 20% larger total side resistance, which is caused by a 60% larger pile perimeter and a slightly smaller unit side resistance. Lateral soil arching effects are developed, causing a non-uniform effective normal stress and a shear stress across the circumference of the XCC single pile. It is suggested that XCC single piles have a higher efficiency in terms of material saving compared with CCC single piles.

1 INTRODUCTION

In order to improve the bearing capacity of a single pile, it is necessary to either increase its side resistance, end resistance or both [1]. By manipulating the cross-sectional geometry of a pile, its cross-sectional perimeter can be increased without increasing the cross-sectional area (material waste), which, in effect, alters the side resistance. Many studies have been conducted on the behaviour of special cross-sectional piles, such as the barrette [2], the belled pile [3], the pipe pile [4-5], the large diameter cast-in-place pipe pile [6], the tapered pile [7], and the H pile [8-9]. These piles alter the cross-sectional shapes that are designed to achieve the same objective, which is improving the pile performance, particularly the bearing capacity.

In recent years a new cross-sectional-shaped pile, the X-section cast-in-place concrete (XCC) pile, has been implemented in China (see Fig. 1). Since 2008, these new XCC piles, constructed as a piled raft system (including pile, gravel and/or geogrid), have been used to reinforce the soft ground for motorways in Nanjing, for example, two linkage sections between the express-way and the Fourth Bridge of the Yangtze River, two sections of the Jiangshan Street, and a section of the 312 National Motorway. The utilization of XCC piles in those projects has resulted in cost savings of more than 20%.

To advance these techniques, mainly for the design and construction of XCC piles, comparative field tests and three-dimensional (3D) numerical back-analyses between an XCC piled raft and a circular-section cast-in-place concrete (CCC) piled raft of the same cross-sectional area and configuration have been conducted by Lv et al. [10-12]. The results indicate that, under the same load conditions, approximately 66% and 46% of the applied load is carried by the XCC and CCC pile, respectively, and simultaneously, approximately 45% and 24% of the applied load is taken by the side resistance of the XCC and CCC pile, respectively. In other words, the larger bearing capacity of the XCC piled raft contributes to the cross-sectional geometry, leading to a larger pile perimeter and arching effects. In addition, a modified analytical solution, dependent on the cross-sectional geometry of XCC piles, was derived from the solution of Mindlin and Geddes by Lv et al. [13]. Corresponding parametric studies were conducted to explore the geometrical effects. In addition, the behaviour of the negative skin friction on the surface of XCC piles has been studied and reported by Kong et al. [14].

However, the stress-transfer mechanism of a single pile is quite different from that of a piled raft [15-17].

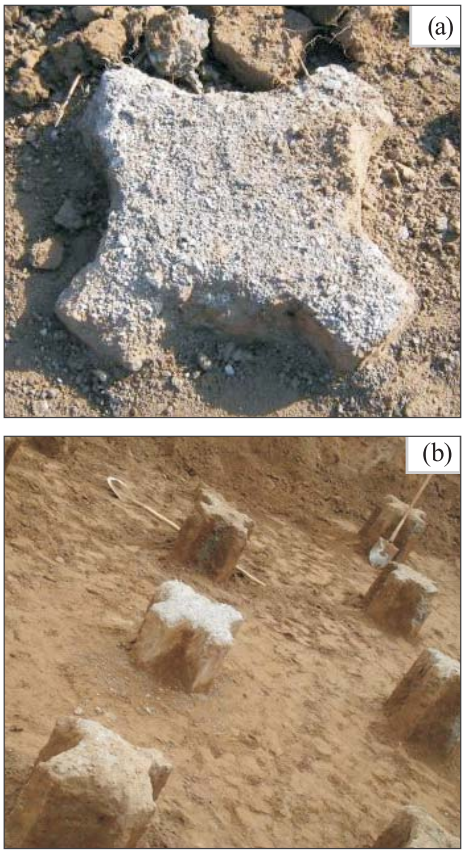

Figure 1. Constructed: (a) XCC single pile, and (b) XCC pile group.

This is because the applied load is entirely carried by the pile for single piles, but it is carried by the piles and their surrounding soil for piled rafts. Nevertheless, the performance of XCC single piles, especially the stress-transfer mechanism between XCC single piles and their surrounding soil, is still not fully understood. This paper aims at revealing the fundamental stress-transfer mechanism for XCC single piles by field tests and 3D numerical back-analyses. For comparison, a CCC single pile of the same cross-sectional area is involved. The pile-soil interactions were considered by means of setting slip elements at the pile-soil interfaces.

2 BRIEF REVIEW OF XCC PILES

The cross-section and corresponding parameters of the XCC piles are shown in Fig. 2. The circle drown by the dashed line is defined as the surrounding circle and the arcs cutting into the surrounding circle at four symmetrical positions are defined as the cutting arc. The geometrical parameters of an X-shaped cross-section are *2a*, *2R*, θ, where *2a* is the distance between two adjacent arcs; *2R* is the diameter of the surrounding circle; and θ is the degree of the central angle of the cutting arcs. Thus, the radius of the cutting arcs *r* can be obtained by:

$$r = \frac{(\sqrt{R^2 - a^2} - a)}{\sqrt{2}\sin\frac{\theta}{2}} \qquad (1)$$

For given geometrical parameters, the cross-sectional area of an XCC pile (A_X) is calculated as:

$$A_x = \pi R^2 - 2\left[\theta\, r^2 - \sin(\theta\ )r^2\right] - \\ - 2\left[\left(\frac{\pi}{2} - 2\arcsin(\frac{a}{R})\right)R^2 - \cos\left(2\arcsin(\frac{a}{R})\right)R^2\right] \qquad (2)$$

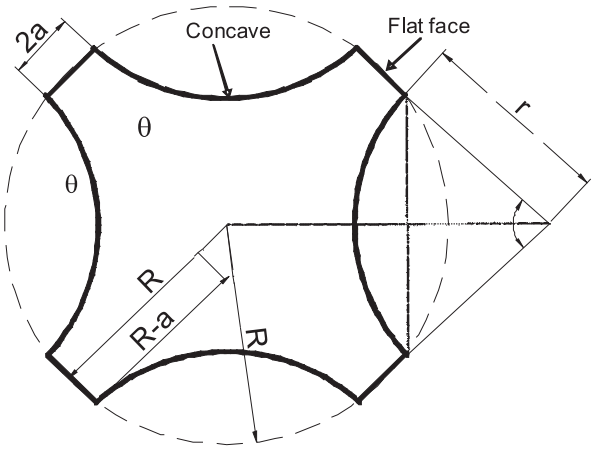

Figure 2. Cross-section and parameters of an XCC pile.

The cross-sectional perimeter of an XCC pile (C_X) is calculated as

$$C_x = 8\arcsin(\frac{a}{R})R + 4\theta\, r \qquad (3)$$

The X-shaped cross-sections are formed to enlarge the pile perimeter by changing the directions of the arcs. Hence, ideally, the side resistance can be increased without decreasing the end resistance.

3 METHODOLOGIES

The performance of XCC single piles was studied using field tests and numerical simulations. Two field static load tests were conducted on an XCC single pile and a CCC single pile of the same cross-sectional area to explore the bearing capacity of XCC single piles. Meanwhile, corresponding 3D numerical back-analyses were carried out, not only to analyze the field tests but also to provide a deeper understanding.

3.1 Brief review of field static load tests

Two field static load tests were conducted in Nanjing, China. The XCC testing pile was cast in place using typical C20 concrete with dimensions of $2R$ = 0.53 m, $2a$ = 0.11 m, θ = 130° and a pile length (L) = 10.5 m, giving a cross-sectional area of 0.112 m^2 (Eq. 2). As a reference, a CCC single pile with the same cross-sectional area (pile diameter D = 0.38 m) was produced. Thus, the perimeters of the XCC cross-section and the CCC cross-section are 1.93 m and 1.19 m, respectively (Eq. 3). The perimeter of the XCC single pile is approximately 60% larger than that of the CCC single pile.

The site of the field tests is a relatively flat terrain. Original landscape features are retained and belong to the Yangtze River floodplain topography, according to the geomorphologic unit. The geotechnical properties of the soil profile are shown in Fig. 3. The ground-water table is located at a depth of approximately 2.2 m below the ground surface. Cone penetration tests (CPTs) were conducted to obtain the stiffness of the soil layers. The soil layer from the ground surface to a depth of approximately 3.5 m is soft; this is a fill layer. From a depth of 3.5 m to 8.0 m, the penetration resistance is more than 10 MPa, indicating a stiff fine sand layer. From a depth of 10.5 m to 20.0 m, the penetration resistance is approximately 7 MPa, suggesting a sand layer. Between the stiff fine sand and the sand layer, there is a soft interlayer with a thickness of 2.5 m, which is silty clay. Some soil samples were retrieved for laboratory testing. The properties of the soil layers, including the water content, the unit weight, the effective friction angle, and the void ratio, are summarized in Table 1.

The test instrumentation consisted of the load apparatus and the detecting instruments. The load apparatus included a hydraulic jack and dial indicators. Different pressures, controlled by the load apparatus, were applied to the pile heads using a slow maintained load testing method. The pressure was read from the hydraulic table

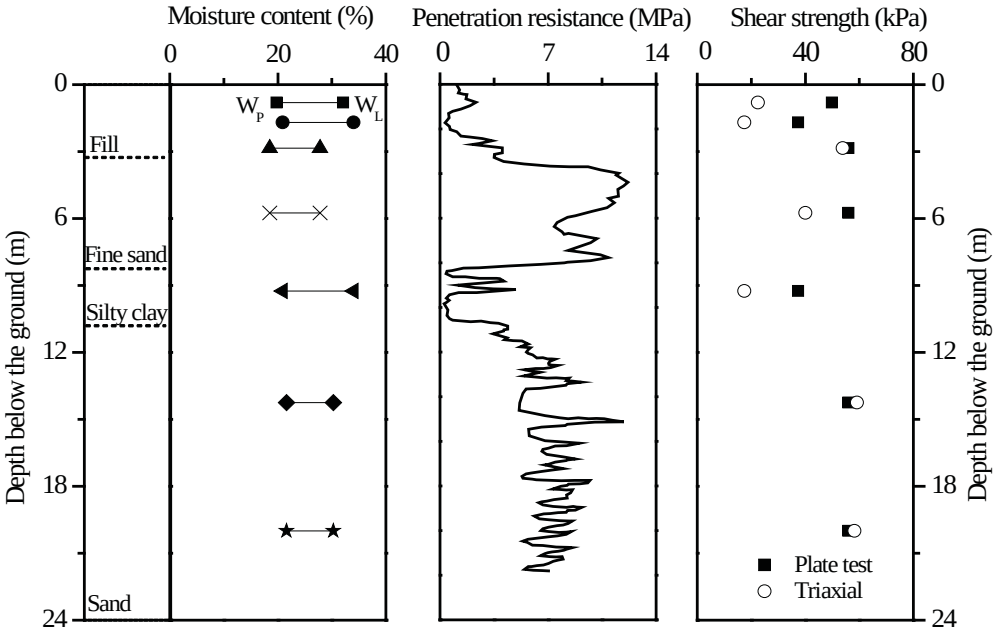

Figure 3. Soil layers and properties.

Table 1. Properties of the soil layers.

From /m	To /m	Type of soil	Mean water content /%	Void ratio	Unit weight /(kN/m^3)	Young's modulus /MPa	Cohesion */kPa	Effective friction angle /°
0.0	3.5	Fill	29.4	0.96	17.8	6	0	20
3.5	8.0	Fine sand	26.3	0.76	18.9	24	0	20
8.0	10.5	Silty clay	38.6	1.11	17.6	6	0	31
10.5	20.0	Sand	26.1	0.75	18.9	24	0	31

* denotes 1 Pa in ABAQUS

and the settlement was recorded using dial indicators with an accuracy of 0.01 mm. Each instrument was calibrated before the tests. More details about the field tests can be found in the literature [11].

3.2 Introduction of 3D numerical back-analyses

In this paper, 3D numerical back-analyses were carried out using the finite-element program ABAQUS [18]. For consistency, a full solid was simulated without taking advantages of the symmetry. In other words, the dimensions of the numerical CCC single pile and the numerical XCC single pile coincide well with those of the corresponding testing pile. Fig. 4a shows the meshes of the 3D pile foundations. Reduced integrated 8-node brick elements were created. Duplicated nodes were used to form a zero-thickness interface between the piles and their surrounding soil, as shown in Fig. 4b, adjacent to which the fine elements were generated. The interface friction angle (δ) was estimated using the equation proposed by Randolph and Wroth [19]:

$$\delta = \tan^{-1}[\sin\phi' \cos\phi' / (1+\sin^2\phi')] \qquad (4)$$

where ϕ' is the effective friction angle. The lateral earth-pressure coefficients (K_0) were estimated using the equation:

$$K_0 = 1 - \sin\phi' \qquad (5)$$

The external boundaries were positioned 5 m (approximately 13D) laterally from the center of the single piles and 20 m (approximately 1.9L) below the ground surface. Since the piles located at a distance of 6D or greater can be considered as a single acting pile [20], the distance chosen (13D) is deemed as sufficient to ensure no boundary effects. The boundary conditions are as follows: the radial curved plane was allowed to move freely in the tangential and z directions, but was fixed in the radial direction; for the bottom plane (i.e., z = 20 m), all of the movements were restrained.

A drained analysis was used in the numerical simulations. The piles (typical concrete) were simulated to be

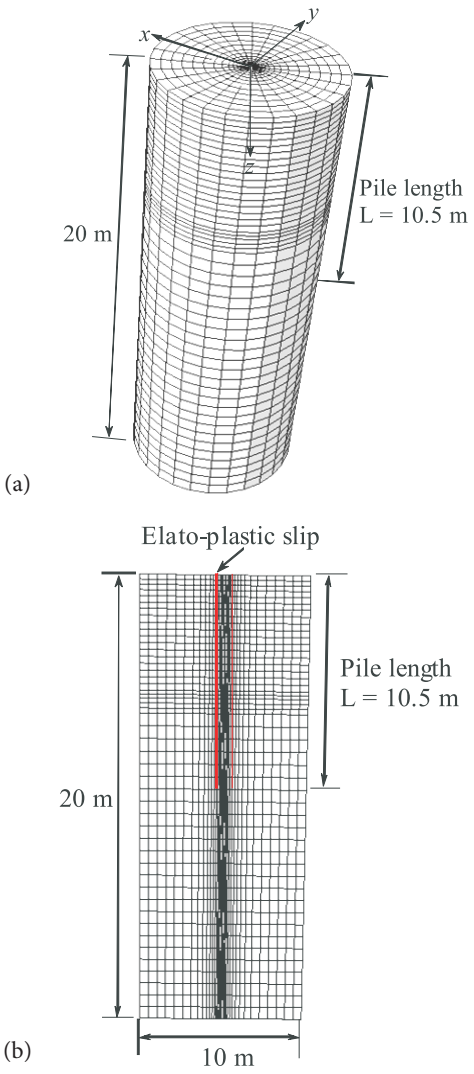

Figure 4. Finite-element mesh of: (a) 3D pile, and (b) elasto-plastic slip.

linear-elastic, with the Young's modulus being E_p (= 20 GPa) and the Poisson's ratio being ν (= 0.2). The soil profile was simulated as an elasto-plastic material using the composite Mohr-Coulomb criterion. Fig. 5 shows the yield surface of the Mohr-Coulomb criterion [18]. The yield function is given by

$$F = R_{mc}q - p\tan\phi - c = 0 \qquad (6)$$

where p is the normal stress; q is the deviatoric stress; and $R_{mc}(\Theta,\phi)$ is a measure of the shape of the yield surface in the deviatoric plane and is defined as

$$R_{mc} = \sin(\Theta + \pi/3)\Big/(\sqrt{3}\cos\phi) + \cos(\Theta + \pi/3)\tan\phi/3 \quad (7)$$

where ϕ is the slope of the Mohr-Coulomb yield surface in the $R_{mc}q$-p stress plane, which is commonly referred to as the friction angle of the soils and ranges from 0 to 90°; c is the cohesion of the material; and Θ is the deviatoric polar angle, which is defined as

$$\cos(3\Theta) = r^3/q^3 \qquad (8)$$

where r denotes the third stress invariant.

To eliminate the influence of apparent cohesion, the values of the cohesion for all of the soil layers were set to zero (1 kPa in ABAQUS). The effective friction angles were given according to the laboratory tests. The Young's moduli of the soil layers were estimated based on the CPT tests. The Poisson's ratios were taken to be 0.35 for all of the soil layers. The groundwater table was set at 2.2 m below the ground surface as the monitored results in field. The soil properties are summarized in Table 1.

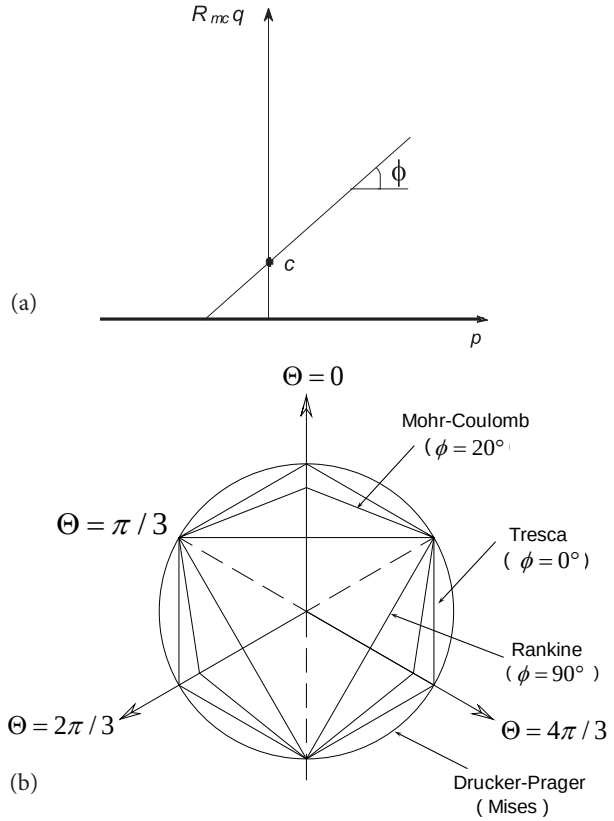

Figure 5. Yield surface of the Mohr-Coulomb criterion in: (a) the meridional plane, (b) the deviatoric plane [18].

To simulate the static load tests, twelve steps including eight loading steps from P = 100 kN to 800 kN and four unloading steps from P = 800 kN to 0 kN were applied to the CCC single pile. A corresponding fifteen steps, including ten loading steps from P = 100 kN to 1000 kN and five unloading steps from P = 1000 kN to 0 kN, were applied to the XCC single pile. The load of each step was applied to the pile heads using linear amplitude.

4 RESULTS AND ANALYSES

4.1 Measured and computed load-settlement relationships

The measured and computed pile settlements versus the applied loads are shown in Fig. 6. Since the pile tips were located at the bottom sand layer, the measured settlement curves do not show a well-defined ultimate load. The computed settlement curves illustrate obvious elastic and plastic stages. The plastic stages of the CCC single pile and the XCC single pile start at approximately P = 220 and 310 kN, respectively. In addition, the computed settlement of the CCC single pile is underestimated during the loading stages. Meanwhile, the computed settlement of the XCC single pile is underestimated for the former loading stages, but overestimated for the latter loading stages. The differences between the measured and the computed results could be induced by overestimating the soil stiffness and idealizing the constitutive model. However, good agreements in the trend indicate the validation of the numerical back-analyses.

The ultimate bearing capacity that was adopted in this study was obtained using the settlement criterion s/D = 5% [21], where s denotes the pile settlement and D denotes the equivalent pile diameter. Hence, the

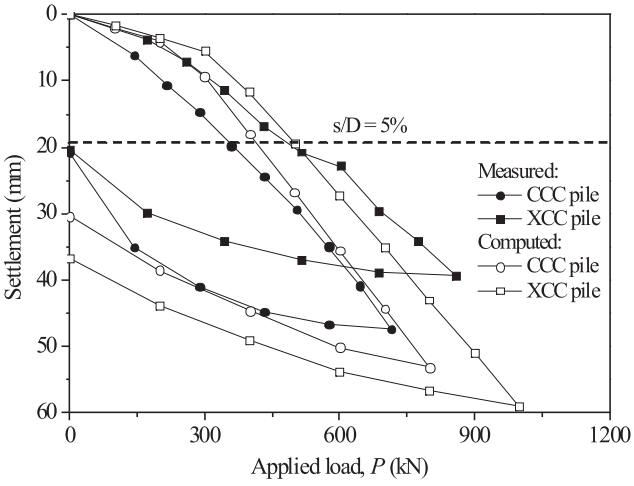

Figure 6. Measured and computed load-settlement relationships.

measured ultimate bearing capacities of the CCC single pile and the XCC single pile are P = 350 and 500 kN, respectively. Subsequently, using the same criterion, the computed ultimate bearing capacities of the CCC single pile and the XCC single pile are approximately P = 400 and 500 kN, respectively. It is obvious that the computed XCC single pile has an approximately 25% higher ultimate bearing capacity than the CCC single pile of the same cross-sectional area. In other words, XCC single piles have a higher efficiency in the cross-sectional area than the CCC piles. The contributions of the higher bearing capacity of the XCC piles will be explored step by step.

4.2 Load sharing between the side resistance and the end resistance

Fig. 7a and 7b show the computed axial forces of the CCC single pile and the XCC single pile, respectively. Both the CCC single pile and the XCC single pile have a similar trend, i.e., the axial force increases with an increasing applied load. Since the maximum loads of 800 kN and 1000 kN were applied to the CCC single pile and the XCC single pile in field tests, respectively, four loading steps (i.e., 200 kN, 400 kN, 600 kN, and 800 kN) are involved in the computed CCC single pile, and five loading steps (i.e., 200 kN, 400 kN, 600 kN, 800 kN, and 1000 kN) are included for the computed XCC single pile in this figure. Additionally, both the CCC single pile and the XCC single pile have another similar trend, i.e., the axial force decreases with the increasing depth. The axial force at the pile heads equals the applied load (P), while the axial force at the pile tips indicates the end resistance (Q_{end}). Therefore, the slope of the axial force is the unit side resistance and the difference between the applied load and the end resistance (P–Q_{end}) is the total side resistance. It was observed that the slope of the axial force of the XCC single pile is smaller than that of the CCC single pile, demonstrating that the side resistance of the XCC single pile should be larger than that of the CCC single pile. In other words, the end resistance of the XCC single pile is smaller than that of the CCC single pile. This is because the XCC single pile has 60% more pile perimeter than the CCC single pile, although it has an identical cross-sectional area.

Based on the above description, the load sharing of the end resistance (α_{end}) and the side resistance (α_{side}) is obtained using Eq. 9 and Eq. 10, respectively. Fig. 8 shows the proportion of the load sharing of the side resistance and the end resistance with respect to the applied load. No matter what the cross-sectional shapes, α_{end} decreases with the applied load for the initial loading stages, but the trend becomes negative during the later loading stages, resulting in a minimum peak value at approximately P = 300 kN. Meanwhile, α_{side} increases with the applied load for the initial loading stages, but the trend becomes negative for the later loading stages, inducing a maximum peak value at the same load. This phenomenon is governed by the mobilization of the side resistance and the end resistance. It is found that during the initial loading stages, more than 80% of the applied load is carried by the end resistance. This indicates that the applied load is mainly resisted by the pile tips because the trend of the relative motion between the pile and soil has not been developed. Then, α_{side} exceeds 50% at approximately P = 200 kN. After the full mobilization of the side resistance (relative motion is approximately 5 to 10 mm) [22], α_{side} decreases, but α_{end} increases again. This is because the end resistance is fully mobilized at approximately s/D = 5%, which is always later than the full mobilization of the side resistance [22].

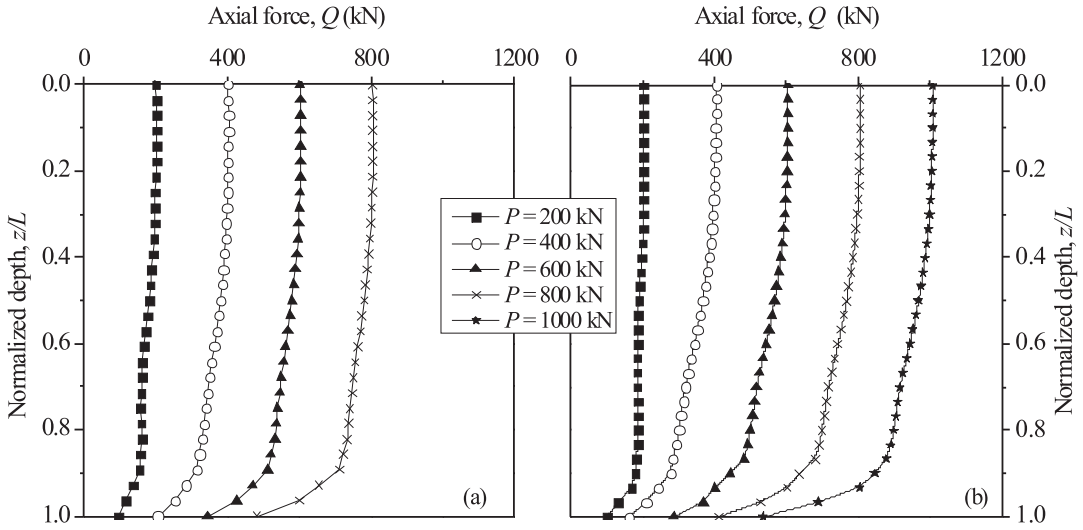

Figure 7. Computed axial force of: (a) CCC single pile, and (b) XCC single pile.

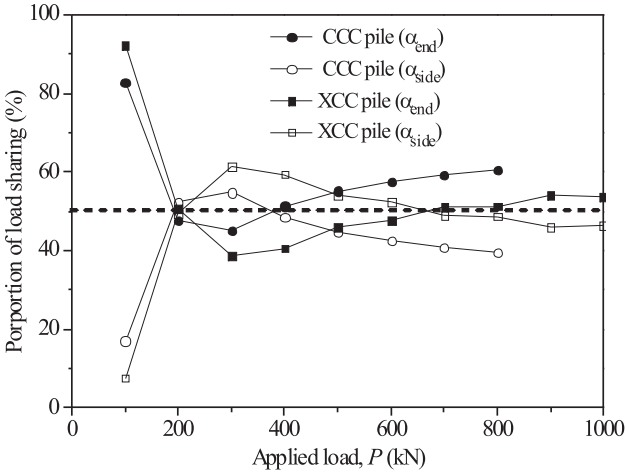

Figure 8. Computed load sharing of the side resistance and the end resistance.

$$\alpha_{end} = \frac{Q_{end}}{P} \qquad (9)$$

$$\alpha_{side} = 1 - \alpha_{end} = \frac{P - Q_{end}}{P} \qquad (10)$$

In addition, it was found that α_{side} is exceeded by α_{end} at P = 400 and 700 kN for the CCC single pile and the XCC single pile, respectively. This illustrates that the side resistance of the XCC single pile plays a more important role in resisting the applied load than the CCC single pile in serviceability conditions [22]. For example, α_{side} of the XCC single pile is always larger than that of the CCC single pile. The average side resistance of the XCC single pile is about 120% that of the CCC single pile.

4.3 Unit side resistance and total side resistance

In order to investigate the larger α_{side} of the XCC piles, the unit side resistance and the total side resistance at P = 500 kN are derived in Fig. 9a and 9b, respectively. In this study, the unit side resistance is back-calculated using the axial force. The total side resistance of a cross-section is obtained by the unit side resistance multiplied by the pile perimeter and the effective length of the segment. From the figure it is clear that the unit side resistance of the XCC single pile is smaller than that of the CCC single pile, especially for the lower part of the pile shaft. Below z/L = 0.7, the discrepancy between the two piles increases as the depth is increased. The unit side resistance of the CCC single pile is more than three times that of the XCC single pile at z/L = 0.85. Since the pile perimeter is normalized, the difference is caused by geometrical effects. After multiplying the unit side resistance by the pile perimeter, the total side resistance of the XCC single pile is about 120% that of the CCC single pile. This means that the pile perimeter plays an important role in improving the side resistance of XCC piles. The 60% higher pile perimeter induces an about 20% total side resistance, indicating that XCC single piles have a lower efficiency in the pile perimeter than the CCC piles.

To reveal the lower efficiency of the pile perimeter for XCC piles, the shear stress at different locations, i.e., X1, X2, X3, and X4, is derived and shown in Fig. 9c. As a reference, the shear stress estimated by the β-method [23] is also plotted in the same figure, including β = 0.1, 0.2, and 0.3. It was found that the shear stress developed on the concave surfaces of the XCC single pile (that can be described by β = 0.28) is larger than that developed

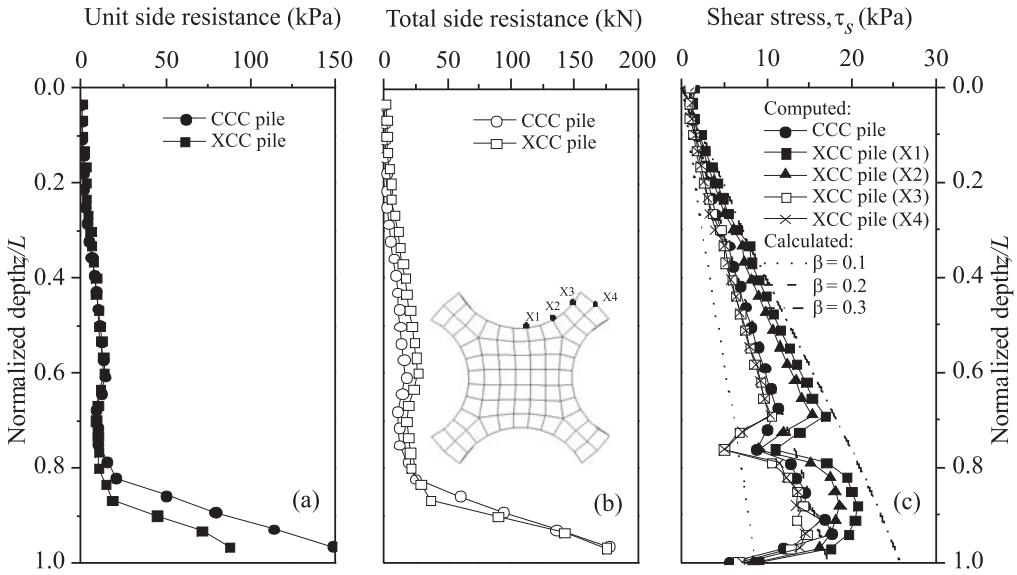

Figure 9. Computed: (a) unit side resistance, (b) total side resistance, and (c) non-uniform shear stress under P = 500 kN.

on the cylindrical surfaces of the CCC single pile (which can be described by $\beta = 0.20$), which is in turn larger than that developed on the outward flat surfaces of the XCC single pile (which can be described by $\beta = 0.18$). This observation provides two findings: firstly, for XCC piles, the β-method always overestimates the shear stress of the flat surfaces but underestimates the shear stress of the concave surfaces; secondly, the non-uniform shear stress induces a lower efficiency in the pile perimeter of the XCC single piles. In addition, at the intersection of the fill and fine sand ($z/L = 0.33$) and the fine sand and the silty clay ($z/L = 0.76$), the shear stress is unusual due to the special characteristics of the pile-soil interfaces.

4.4 Effective normal stress

Since the magnitude of the shear stress is closely related to the effective normal stress, the effective normal stress in the surrounding soil elements is derived on the basis of polar coordinates. Fig. 10 shows the effective normal stress distribution for the section $z/L = 0.5$ at $P = 500$ kN. It was found that the effective normal stress acting on the concave surfaces of the XCC pile is the largest of all sections, resulting in the largest shear stress at position X1 (see Fig. 9c). Meanwhile, the effective normal stress acting on the flat surfaces of the XCC pile is smaller than that on the cylindrical surface of the CCC pile and the concave surfaces of the XCC pile, resulting in a small shear stress of X4. This is because specific soil arching effects are developed across the circumference of the XCC piles, inducing stress redistribution. This is the fundamental reason for the larger ultimate bearing capacity of XCC single piles.

In order to illustrate the distribution of the effective normal stress along the depth, the effective normal stress acting on the pile shafts along the depth under $P = 500$ kN is shown in Fig. 11. Different locations, i.e., X1, X2, X3, and X4, are also involved. It was found that no matter whether it is the CCC single pile or the XCC single pile, the effective normal stress increases along the upper depth and then decreases along the lower depth. There are peak values at the intersections between two adjacent soil layers (i.e., $z/L = 0.33$ and 0.76). This trend agrees well with the distribution of the non-uniform shear stress (see Fig. 9c). Governed by the geometrical effects, the effective normal stress acting on X1 is the largest, but that acting on X3 is the smallest. In other words, the non-uniform shear stress on XCC pile shafts is induced by the non-uniform effective normal stress, which in turn results from the stress concentration and the principal stress rotation. There is an interesting phenomenon that the effective normal stress of X4 is obviously larger than that of X3, but the shear stresses of X3 and X4 are almost identical. This result demonstrates that the flat surfaces are easier to fully mobilize than the concave surfaces.

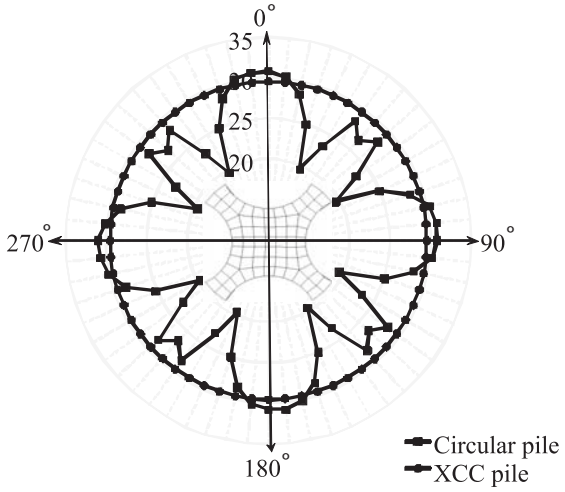

Figure 10. Computed effective normal stress at $z/L = 0.5$ under $P = 500$ kN.

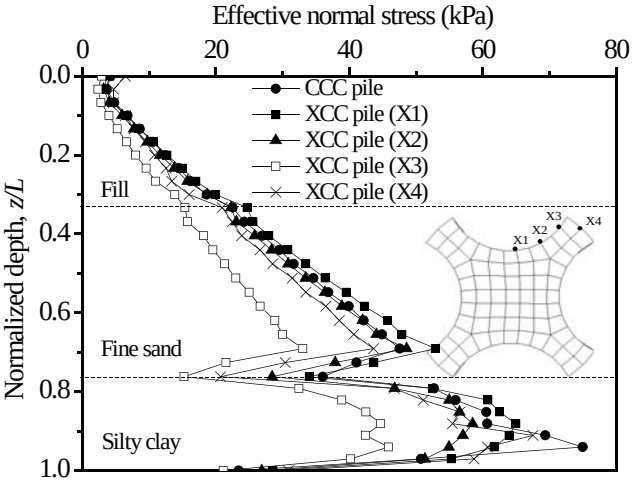

Figure 11. Computed effective normal stress along the depth under $P = 500$ kN.

5 CONCLUSIONS

Two field static load tests and the corresponding 3D numerical back-analyses were performed on an XCC single pile and a CCC single pile of the same cross-sectional area to investigate the performance of XCC single piles with respect to the geometrical effects. Based on the measured and computed load-settlement relationships, it is observed that the XCC single pile has an approximately 25% higher ultimate bearing capacity than the CCC single pile. This is mainly attributed to the geometrical effects of XCC piles, including a larger pile perimeter and a special stress-transfer mechanism, resulting in a large total side resistance.

Although the unit side resistance of the XCC single pile is slightly smaller than that of the CCC single pile under

the same applied load, the total side resistance of the XCC single pile is approximately 120% that of the CCC single pile. This is caused by two opposite factors: firstly, the perimeter of the XCC single pile is approximately 160% that of the CCC single pile; secondly, the unit side resistance acting on the XCC single pile is smaller than that on the CCC single pile due to geometrical effects. A non-uniform effective normal stress was observed across the circumference of the XCC singe pile, leading to a non-uniform shear stress. Thus, the shear stress acting on the concave surfaces of the XCC single pile is larger than that on the cylindrical surface of the CCC single pile, which is larger than that on the flat surfaces of the XCC single pile. This is the special stress-transfer mechanism of XCC single piles, which is induced by soil arching effects around the X-shaped cross-section.

XCC single piles have a higher efficiency in the cross-sectional area (material saving) than CCC single piles of the same cross-sectional area since they have a higher bearing capacity. Meanwhile, XCC single piles have a lower efficiency in the cross-sectional perimeter than CCC single piles of the same cross-sectional area because the increment of the bearing capacity (25%) is smaller than the increment of the pile perimeter (60%).

Acknowledgement

The authors acknowledge the support of the National Nature Science Foundation of China (51408607), the Central Universities fund operating expenses (No: 2013B01214).

REFERENCES

[1] Poulos, H.G., Davis, E.H. 1980. Pile foundation analysis and design. New York Wiley.
[2] Gifford, A.B., Green, G.E., Buechel, G.J., Feldman, A.I. 1986. In situ tests and design of a cylinder pile wall. Use of in situ tests in geotechnical engineering (GSP 6) (ASCE), New York, pp. 569–587.
[3] Ng, C.W.W., Yau, T.L., Li, J.H., Tang, W.H. 2001. Side resistance of large diameter bored piles socketed into decomposed rocks. Journal of Geotechnical and Geoenvironmental Engineering (ASCE) 127, 8, 642–657.
[4] Lee, J.H., Salgado, R., Paik, K. 2003. Estimation of load capacity of pipe piles in sand based on cone penetration test results. Journal of geotechnical and geoenvironmental engineering (ASCE) 129, 5, 391–403.
[5] White, D.J. 2002. An investigation into the behaviour of pressed-in Piles. PhD dissertation, University of Cambridge.
[6] Ding, X.M., Zheng, C.J., Liu, H.L. 2014. A theoretical analysis of vertical dynamic response of large-diameter pipe piles in layered soil. Journal of Central South University 21, 3327–3337.
[7] Ghazavi, M. 2007. Analysis of kinematic seismic response of tapered piles. Geotechnical and Geological Engineering 25, 1, 37–44.
[8] William, G.D., Thomas, S., Sarah, A., John, D., Christopher, L. 2010. Field-measured response of an integral abutment bridge with short steel H-piles. Journal of Bridge Engineering 15, 1, 32–43.
[9] Yang, J., Tham, L.G., Lee, P.K.K., Yu, F. 2006. Observed performance of long steel H piles jacked into sandy soils. Journal of Geotechnical and Geoenvironmental Engineering (ASCE) 132, 1, 24–35.
[10] Lv, Y., Ding, X., Liu, H. 2011. In-situ tests on cast-in-place concrete X-section pile for bearing capacity of single-pile composite foundation. Geotechnical Special Publication No. 220 ASCE, Changsha, 39–47.
[11] Lv, Y., Liu, H., Ding, X., Kong, G. 2012. Field tests on bearing characteristics of X-section pile composite foundation. Journal of Performance of Constructed Facilities (ASCE) 26, 2, 180–189.
[12] Lv, Y., Liu, H., Ng, C.W.W., Ding, X., Gunawan, A. 2014. Three-dimensional numerical analysis of the stress transfer mechanism of XCC piled raft foundations. Computer and Geotechnics 55, 365–377.
[13] Lv, Y., Liu, H., Ng, C.W.W., Gunawan, A., Ding, X. 2014. A modified analytical solution of soil stress distribution for XCC pile foundations. Acta Geotechnica 9, 3, 529–546.
[14] Kong, G., Zhou, H., Liu, H., Ding, X., Liang, R. 2014. A simplified approach for negative skin friction calculation of special-shaped pile considering pile-soil interaction under surcharge. Journal of Central South University 21, 3648–3655.
[15] Clancy, P., Randolph, M. F. 2001. Analysis of piled raft foundations using a variational approach. International Journal for Numerical and Analytical Methods in Geomechanics 17, 12, 849–869.
[16] Poulos, H.G. 2001. Piled raft foundations-design and applications. Géotechnique 50, 2, 95-113.
[17] Kalpakci, V., Özkan, M.Y. 2012. A simplified approach to the settlement estimation of piled rafts. Acta Geotechnica Slovenica 1, 77-85.
[18] ABAQUS standard user's manual, Ver. 6.6. 2006. Hibbitt, Karlsson & Sorensen. Inc., Pawtucket, R.I.
[19] Randolph, M.F., Worth, C.P. 1980. Application of the failure state in undrained simple shear to the shaft capacity of driven piles. Géotechnique 31, 1, 143-157.
[20] Lee, C.J., Chen, C.Z. 2002. Negative skin friction on ground piles. Proc. Int. Conf. Physical Modeling in Geotech., St. John's Newfoundland, Canada, 679-684.
[21] O'Neill, M.W., Reese, R.C. 1999. Drilled shaft: construction procedures and design methods. Federal Highway Administration, Washington, D.C.
[22] O'Neill, M.W. 2001. Side resistance in piles and drilled shafts. Journal of Geotechnical and Geoenvironmental Engineering (ASCE) 127, 1, 3-16.
[23] Meyerhof, G.G. 1976. Bearing capacity and settlement of pile foundations. Journal of Geotechnical and Geoenvironmental Engineering 102, 3, 197-227.

OBNAŠANJE ZEMLJINE OJAČANE S PASIVNIMI SIDRI IN BRIZGANIM BETONOM TER SIDRANIH ZIDOV NA PODLAGI PODATKOV TERENSKEGA MONITORINGA V RAZLIČNIH POGOJIH TAL V ISTANBULU

Dogan Çetin
Yildiz Technical University,
Civil Engineering Department
Davutpasa Campus, Esenler, Istanbul, Turčija
E-pošta: dogancetin56@hotmail.com

Ključne besede

globoki izkop, premik zidu, sestava tal, zaščita iz pasivnih sider in brizganega betona, sidrani zid

Izvlecek

V študiji so, iz več kot 90 terenskih opazovanj, zbrani in analizirani podatki o bočnih premikih sten 28 globokih izkopov v Istanbulu. Najbolj pogosto uporabljeni podporni zidovi za izvedbo globokih izkopov v Istanbulu so zidovi iz pasivnih sider in brizganega betona (SNPWs) in kontinuirane pilotne stene (CPWs). Druge vrste podpornih zidov vključujejo sidrane stene iz mikro pilotov (MPWs), diafragme (DWs), betonske stene (CWs) in pilotne stene s prekrivanjem pilotov (SPWs). Analize so bile izvedene za podatke za zidove iz pasivnih sider in brizganega betona ter podatke za sidrane zidove. Vrednosti maksimalnih bočnih pomikov zidu $\delta_{h,max}$ za projekte iz pasivnih sider in brizganega betona se splošno gibljejo od 0.05%H do 0.35%H, s povprečno vrednostjo 0.20%H. Medtem, ko se vrednosti maksimalnih bočnih pomikov zidu $\delta_{h,max}$ za projekte s sidranimi pilotnimi stenami splošno gibljejo od 0.043%H do 0.32%H, s povprečno vrednostjo 0.155%H. Nekateri dejavniki, ki vplivajo na deformacije globokih izkopov, kot so gostota pasivnih sider, kvocient vpetja stene in togost stene, so bili proučevani na osnovi podatkov terenskega opazovanja. Premiki zidu so bili primerjani tudi z rezultati opazovanj bočnih premikov nekaterih primerov varovanja izkopov iz celega sveta.

PERFORMANCE OF SOIL-NAILED AND ANCHORED WALLS BASED ON FIELD-MONITORING DATA IN DIFFERENT SOIL CONDITIONS IN ISTANBUL

Dogan Çetin
Yildiz Technical University,
Civil Engineering Department
Davutpasa Campus, Esenler, Istanbul, Turkey
E-mail: dogancetin56@hotmail.com

Keywords

deep excavation, wall displacement, soil formation, soil-nailed wall, anchored wall

Abstract

In this study, data on the lateral wall displacements of 28 deep excavations in Istanbul soil from over 90 field monitors were collected and analysed. The most commonly used retaining walls for deep excavations in Istanbul are soil-nailed shotcrete walls (SNPWs) and contiguous pile walls (CPWs). Other types of retaining walls include anchored micropile walls (MPWs), diaphragm walls (DWs), concrete walls (CWs) and secantpile walls (SPWs). The analyses were performed under two main headings: analysis of soil-nailed walls' data and analysis of anchored walls' data. The data of $\delta_{h,max}$ generally range from 0.05%H to 0.35%H with an average value of 0.20%H in the soil-nailed projects. The data of $\delta_{h,max}$ generally range from 0.043%H to 0.32%H with an average value of 0.155%H in anchored pile wall projects. Some factors affecting the deformation of deep excavations, such as nail density, embedded wall ratio and wall stiffness, were studied based on field-monitoring data. Wall movements were also compared with observations in some case histories from around the world.

1 INTRODUCTION

Due to the city's rapid economic growth, a number of deep excavation projects for high-rise buildings, shopping malls and metro systems have been carried out in Istanbul during the past two decades [1]. Estimates of the wall movements and ground deformations induced by deep excavations are critically important in urban areas in order to be able to provide safety for adjacent structures and buildings [2, 3]. Understanding the behaviour of excavation bracing is a complicated issue because of the number of factors affecting the performance of wall systems, such as soil type, base stability, compression and rebound, consolidation, wall-system stiffness, construction procedures, and workmanship [3, 4]. Any of these factors can contribute to the overall movement of a supported excavation. Therefore, great concern has been shown with respect to deep excavations since the report initiated by Peck [5]. Numerous researches have been performed to understand and evaluate the behaviour of retaining walls. Because of the difficulties in making a direct analysis of the performance of wall systems and the behaviour of ground deformation [3,6,7], case studies have been a better way to obtain information about deep excavations and retaining walls. Case studies performed by Ma et al. [3], Hwang and Moh [6], Finno and Bryson [8], Ou et al. [9], Hou et al. [10], Wong and Chou [11] can be given as examples.

Databases prepared by Goldberg et al. [12], Mana and Clough [13], Clough and O'Rourke [14], Ou et al. [15], Wong and Patron [16], Carder [17], Fernie and Suckling [18], Wong et al. [19], Hsieh and Ou [20], Long [21], Yoo [22], Moormann [23] and Leung and Ng [24] present comprehensive information about the performance of in-situ walls constructed in urban areas in terms of different soil conditions, adjacent structures and utilities.

In this study, data from field monitors on the lateral displacement of the walls from some 28 deep excavations in Istanbul soil were collected. The notation for the symbols and parameters used in this study is shown in Figure 1. The magnitudes of the lateral displacement for different types of retaining systems were compared with each other and also compared with relevant case histories worldwide. Furthermore, some factors affecting the deformation of deep excavations were studied.

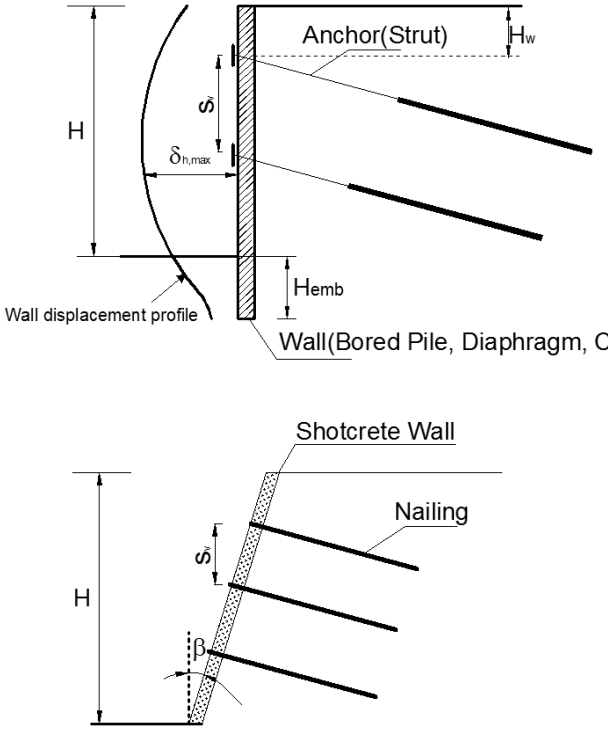

Figure 1. Definition of the wall and support parameters in a deep excavation.

H is the excavation depth, H_{emb} is the embedded wall length, s_v is the vertical distance between the anchors or soil-nailing levels, H_w is the depth of the ground-water level from the surface, $\delta_{h,max}$ is the maximum wall displacement and β is the wall inclination from the vertical in Fig.1.

2 GENERAL SOIL CONDITIONS IN PROJECT FIELDS

A very comprehensive and detailed geotechnical survey carried out by the Metropolitan Municipality of Istanbul between 2005 and 2009 for very large areas of both the Asian and European sides of the city [25, 26] was used to explain the soil profile and general soil properties in the project fields. As a result of that intensive work, 24 different local soil formations were identified on both the Asian and European sides. If the project fields are placed on the map of the microzonation work, it can be seen that 7 of the 24 local formations were encountered in deep-excavation projects. These local formations can be called Fill, Alluvium, Gungoren, Gurpinar, Bakirkoy, Cukurcesme and Trakya. The alluvium in the investigated areas mainly consists of clay-type materials of soft-to-medium stiffness. Sand layers are also present at different depths. The Gungoren formation is composed of clay and sand layers that are very stiff and dense. The over-consolidated clay layers in this formation show claystone properties. The Gurpinar formation generally consists of consecutive clay-claystone and/or sand-sandstone layers. The Bakirkoy formation contains limestone layers, but this formation also has clay-sand layers within the limestone layer. The Cukurcesme formation in the investigated areas is mostly composed of gravel and/or sand of different fractions and forms. The Trakya formation is the general name of the claystone-sandstone-mudstone in Istanbul. The upper level of this formation can be seen mostly as highly fractured and/or weathered. Therefore, the upper levels in the Trakya formation can be defined as clay or sand, depending on the main fraction of the material. Figure 2 shows the borders of the investigation areas. The investigation work can be classified as in-situ tests and laboratory tests.

According to the soil-investigation works carried out by the related department of the Metropolitan Municipality of Istanbul, the ground-water level is generally between 1 m and 20 m from the ground surface in the investigated area depending on the altitude of the point at which the measurement of the ground-water level was made.

2.1 In-situ Tests

The geological investigation and geophysical measurements were carried out as in-situ tests. The geological investigation consists of normal borehole, deep borehole, liquefaction borehole, landslide borehole and CPT. Table 1 shows the content of the geological survey.

Table 2 shows the content of the geophysical investigation.

Table 1. Content of the geological survey.

Type of investigation work	Number of borehole points for Asian Side	Number of borehole points for European Side	Total quantity of bore-holes for Asian Side (m)	Total quantity of boreholes for European Side (m)
Normal Borehole	4426	2830	98681	86840
Deep Borehole	122	27	11594	4201
Liquefaction Borehole	433	764	6683	12344
Landslide Borehole	10	608	227	18144
CPT Test	?	663	4076	8769

Table 2. Content of the geophysical investigation.

Measurement method	Number points measured for Asian Side	Number points measured for European Side	Total quantity (m)
Seismic refraction	4132	2762	435093
Seismic reflection	-	-	34105
PS-Logging	504	201	10997
Array microtremor	30	30	-
Electric resistance	80	2625	-

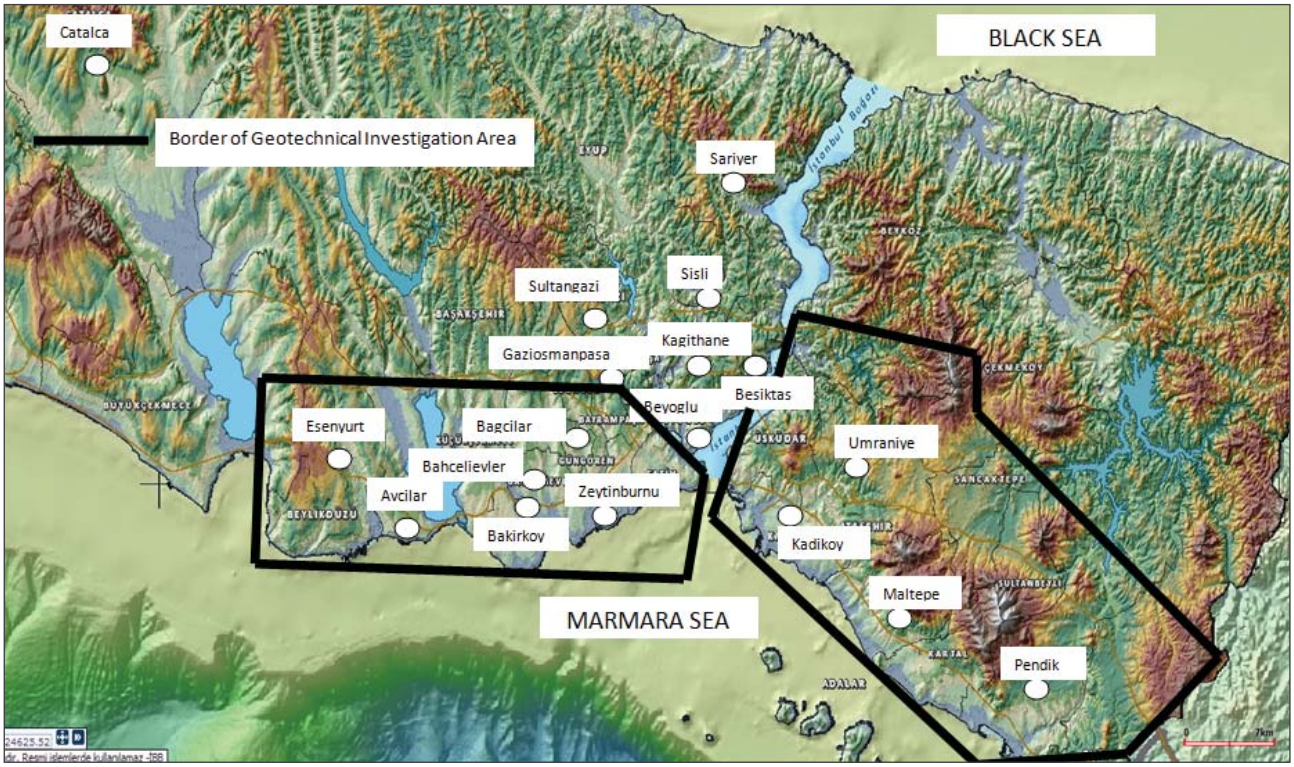

Figure 2. Location of the projects and the border of the geotechnical investigation area in Istanbul.

2.2 Laboratory Tests

Laboratory tests included whole basic soil tests such as Atterberg limits, sieve analysis, unaxial and triaxial compressive strength tests, natural water content tests, hydrometer tests and consolidation tests. According to the reports of the microzonation works [25, 26], for natural water content tests ASTM D2216, for sieve analysis ASTM D422, for hydrometer tests ASTM D4221, for Atterberg Limits tests ASTM D4318, for unconfined compression tests ASTM D2166 and for Triaxial Compression tests ASTM D2850 standards were followed. Table 3 shows the content of the laboratory tests.

Table 3. Content of the laboratory tests.

Side	Natural water content tests	Determination of the grain size distribution		Atterberg Limits	Unaxial Compressive Tests	Triaxial Tests	Consolidation
		Sieve analysis	Hydrometer Tests				
Asian	29072	29071	6867	21608	572	214	1339
European	53938	53938	124	46432	1120	462	2315

Table 4. Average soil properties of the local soil formation.

Local formation name	Definition of the formation	W_n (%)	W_L (%)	W_p (%)	I_p (%)	Particle size distribution			C_u (kPa)
						Clay and Silt (%)	Sand (%)	Gravel (%)	
Fill	New and old fill material	23.8	46.5	13.2	33.3	48.4	28.3	23.3	85
Alluvium	Sandy soft to stiff clay	32.2	50.3	13	37.3	68.1	26.4	5.5	69
Trakya	Mudstone, sandstone, claystone (from fractured to extensively fractured)	14.6	35.5	15.3	20.2	35.2	37.7	27.1	93
Gurpinar	Alternating sandy stiff clay-claystone	24.6	56.1	15.7	40.4	73.6	23.4	3	127
Gungoren	Soft-to-medium sandy clay	28.9	60.6	16	44.5	79.1	17.7	3.2	98
Bakirkoy	Limestone with clay strip	24.1	47.1	15.2	31.9	62.8	18	19.2	78
Cukurcesme	Clayey gravely sand	17.8	41.3	13.5	27.8	36.6	54.2	9.2	164

As a result of a comprehensive geotechnical investigation, 24 different local soil formations were identified on the Asian and European sides of Istanbul. As can be seen from Figure 2, most of the projects were carried out bordering the geotechnical investigation area. Therefore, the soil formations encountered in the project files were identified using the results of the geotechnical investigation. Selected projects were conducted in 7 different local soil formations. The properties of the soil formation and a brief explanation of the local soil formation are given in Table 4.

3. SUMMARY OF INFORMATION FROM COLLECTED DATA

For the database, data from 28 individual projects in Istanbul were collected. Almost all of these projects were carried out in the past two decades. The data were mainly extracted from conference proceedings, PhD theses and a company database that contains a lot of valuable unpublished data. In each case, the measured wall displacement was analysed in terms of the wall type, the support system and its geometric configuration, the embedded wall ratio, the soil-nailing density, the wall stiffness and the soil type.

The most common method for measuring wall deflection is the use of vertical inclinometers, instruments for measuring the relative horizontal displacements through a borehole casing placed behind the wall. The bottom must be embedded to the zero displacement zone. An inclinometer is read using a probe. The probe measures the tilt, which can be converted to a horizontal movement. The inclinometer probe is connected to a power source and readout unit to enable the measurements. The electrical cable linking the probe to the readout device is usually marked in 0.5-m increments so the shape of the casing can be measured at consistent depths. The measurements are taken starting at the bottom of the inclinometer. Subsequent readings are made of the casing as the probe is raised incrementally, usually at 0.5-m intervals, to the top of the casing. This process is conducted shortly after the casing is installed to determine the initial shape of the casing, i.e., to obtain the zero reading. The difference between the zero and the subsequent readings is used to determine the change in the shape and position of the initially vertical casing [27].

Two sets of casing grooves allow the inclinometer probe to be oriented in either of two planes set at 90° to each other. Therefore, the horizontal components of movement, both transverse and parallel to any assumed direction of movement, can be computed from the inclinometer measurements [28]. The measurement accuracy is generally to hundredths of a mm.

The most commonly used retaining walls for deep excavations in Istanbul are soil-nailed shotcrete walls (SNPWs) and contiguous pile walls (CPWs). Other types of retaining walls include anchored micropile walls (MPWs), diaphragm walls (DWs), concrete walls (CWs) and secant pile walls (SPWs). Summarized information about the projects is given in Table 5.

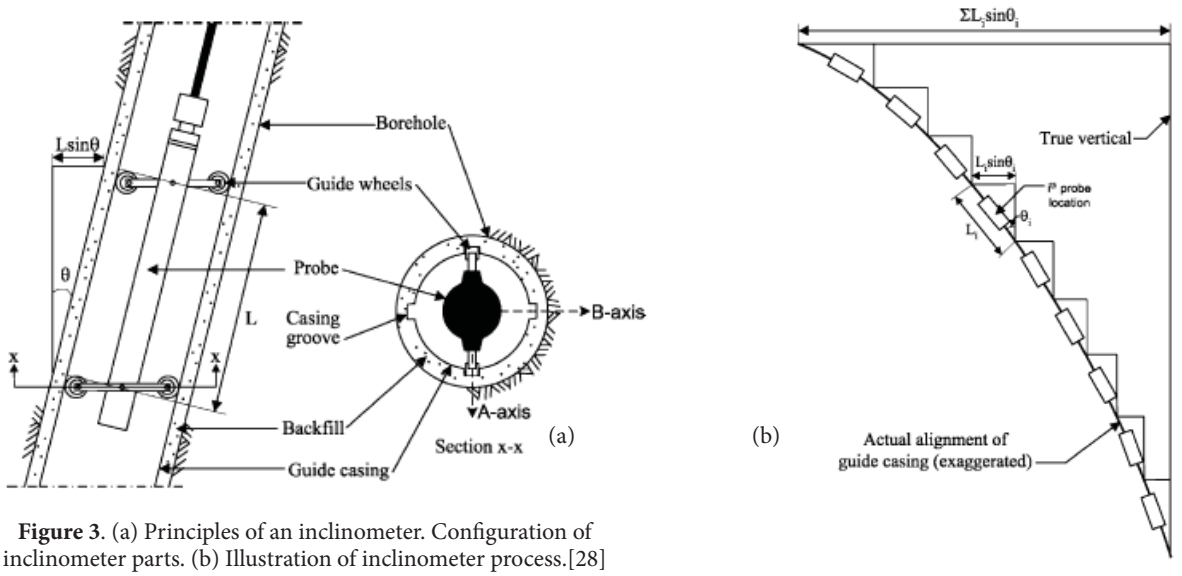

Figure 3. (a) Principles of an inclinometer. Configuration of inclinometer parts. (b) Illustration of inclinometer process.[28]

Table 5. Summary information of the projects.

No.	Project Name	District	Support System	Wall type	Soil profile	Soil formation name	H (m)	H_w (m)	H_{emb} (m)	S_v (m)	S_h (m)	η (m/m^2)	EI (kNm^2/m)	n	$\delta_{h,max}$ (mm)	Reference
1	Baumax AVM	Avcilar	Multi anchored	80 cm diameter bored pile	Clayey sand-Hard clay	Gungoren	15.8	-	6.7	2.4	1	-	312500	4	7.9 25.3 18.9 36.3	Unpublished data
2	Karabulut Textile Factory Project	Kagithane	Multi anchored+ strut	65 cm diameter secant pile	Silty soft clay	Alluvium	8	-2	6	2	1.2	-	172300	2	18.4 30	Unpublished data
3	BusinessPort AVM	Bahcelievler	Multi anchored	65 cm diameter bored pile	Clayey sand-clay	Gungoren	21.6 21.6 21.6 19 18	-	3.7 3.7 3.7 4.1 4.5	2.5	1.8	-	115000	5	49.7 68.5 43.2 34.2 19.8	Unpublished data
4	Taksim Residence	Sisli	Multi anchored	25 cm diameter micro pile	Mudstone-sandstone	Trakya	19.65 18.70	-14		?	?	-	1070	2	19.65 16.8	Cetin et al. [29]
5	Bomonti	Sisli	Multi anchored	25 cm diameter micro pile	Fractured sandstone	Trakya	26 22.8	-	2.5 2.1	2.5	1.5	-	2350	2	43.3 42.5	Unpublished data
			Soil nailing	Shotcrete wall	Fractured sandstone	Trakya	22	-		1.5	1.5	5.5		1	14.60	
6	Tekfen Towers	Levent	Soil nailing	Shotcrete wall	Highly fractured gray-wacke	Trakya	25 24 20 19.50 24	-	-	1.5	2	2.85	?	5	45 14.4 10 9.75 19.2	Yilmaz et al. [30]
7	Otoport	Esenyurt	Multi anchored	80 cm diameter bored pile	Clayey sand-sandy clay	Gungoren	25 21	-6	7.2 6	2.3	2		312500	2	51.7 22.1	Unpublished data
8	Setat 2002	Levent	Soil nailing	Shotcrete wall	Dense fill	Fill	9.50 10 10 13	-	-	1.5	2	2.4	?	4	7.6 10 10 22.1	Yilmaz et al. [30]

Table 5. Summary information of the projects (Continued).

No.	Project Name	District	Support System	Wall type	Soil profile	Soil formation name	H (m)	H_w (m)	H_{emb} (m)	S_v (m)	S_h (m)	η (m/m^2)	EI (kNm^2/m)	n	$\delta_{h,max}$ (mm)	Reference
9	Ideal Hospital	Gazios-manpasa	Multi anchored	100 cm diameter bored pile	Gravely sand overlying sandstone	Cuku-rcesme Trakya	29.2	-	4.4	2.9-2.5-2	1.2	-	699850	1	18.9	Unpub-lished data
10	Metal Co. Factory Project	Catalca	Multi anchored	65 cm diameter secant pile	Sandy gravely clay	?	9.25 5.25	-	6.75 3.75	2.5 1.7	1.8 2	-	123240	2	16.2 4.1	Unpub-lished data
11	BJK Fulya Complex	Besiktas	Soil nail-ing	Shotcrete wall	Exten-sively fractured sandstone	Trakya	18.50 25 32.5	-	-	1.5	1.8	3.4 5.3 4.9	?	3	14.8 22.5 52	Keskin [1]
12	Saglık Group Hotel Project	Beyoglu	Single prop	65 cm diameter secant pile	Alluvium	Alluvium	6.1	-7	5.9	-	-	-	172300	2	7.4 7.9	Unpub-lished data
13	Erdem Hospital	Gunesli	Multi anchored	65 cm diameter bored pile+ reinforced concrete wall	Medium-hard clay	Güng-oren	16.3 16.3	-	3 3	1	0.9-1.8	-	122570	2	45.5 13.7	Unpub-lished data
14	Filiz Con-struction Co.	İkitelli	Multi anchored	80 cm diameter bored pile	Medium-hard clay	Gung-oren	18.2	-	3	-	-	-	312500	4	7.95	Unpub-lished data
15	Besler Co. Ware-house	Pendik	Soil nail-ing	Shotcrete wall	Exten-sively fractured grey-wacke	Trakya	14.7 16.2 18.4	-	-	2 2	2 1.8	2.3 2.4 2.7	-	3	10.3 17.8 12.9	Keskin [1]
16	Ozbas Cons. Co. Residence Project	Kadikoy	Multi anchored	25 cm diameter micro-pile+ 40 cm con-crete wall	Highly fractured sandstone overlying Highly fractured limestone	Trakya Bakirkoy	22.9 25.9 25.9 22.7	-	-	2.1	1.8	-	233940	4	9.1 30.7 40.3 35.7	Unpub-lished data
17	Isti-nyepark	İstinye-Sariyer	Soil nail-ing	Shotcrete wall	Exten-sively fractured gray-wacke	Trakya	10 10 12 12 14 16 18 20 22	-	-	1.5	2	1.7 2.8 2 2.9 3 2.7 3.1 3.2 3.4	?	9	27 22 37.2 25.2 19.6 44.8 55.8 80 96.8	Keskin [1]
18	Kanyon	Levent	Soil nail-ing	Shotcrete wall	Exten-sively fractured gray-wacke	Trakya	14 15.7 18.8 21.3 25.3 26.3 28.3 28.3 28.3	-	-	1.5	2	3.1 3.1 4 4.3 4.7 4.9 5.0 5.0 5.1	?	9	28 45.5 31.9 68.2 58.2 86.8 53.7 67.9 96.2	Keskin [1]

Table 5. Summary information of the projects (Continued).

No.	Project Name	District	Support System	Wall type	Soil profile	Soil formation name	H (m)	H_w (m)	H_{emb} (m)	S_v (m)	S_h (m)	η (m/m^2)	EI (kNm^2/m)	n	$\delta_{h,max}$ (mm)	Reference
19	Zeytinburnu Municipality Underground Parking Lot Project	Zeytinburnu	Multi anchored	45 cm diameter bored pile	Limestone with clay layers	Bakirkoy	11.3		3.7	2.6	2.1	-	29240	6	28.5 34 6.9 8.8 26.6 20.1	Unpublished data
20	Alper Co. Company Residence Project	Umraniye	Soil nailing	Shotcrete wall	Fractured Sandstone	Trakya	15.2 15.2			1.6	1.4	-		2	24.9 34.5	Unpublished data
21	Mashattan Residans	Maslak	Soil nailing	Shotcrete wall	Extensively fractured graywacke	Trakya	18.3			1.5	1.6	2.8		1	58.6	Keskin [1]
22	Terrace-Mix	Esenyurt	Multi anchored	80 cm diameter bored pile	soft-medium clay	Gurpinar	11.5 11.5 13.4 13.4		12 12 9.6 9.6	2.2	1.25	-	312500	4	10.4 15.3 26.9 17.2	Unpublished data
23	Tepe Shopping Mall	Maltepe	Soil nailing	Shotcrete wall	Extensively fractured graywacke	Trakya	7 9 9 10			1.5	1.8	2.4 5.3 3.1 5.3		4	5.6 16.2 15.3 24	Keskin [1]
24	Cultural Center	Sultangazi	Multi anchored	65 cm diameter bored pile	Fill -Sandstone	Fill Trakya	17.6 17.6		3 3	2	1.7	-	146000	2	4.5 6.7	Unpublished data
25	Hotel Radisson	Kucukcekmece	Soil nailing	Shotcrete wall	clay-sand-limestone-over consolidated clay	Gungoren Bakirkoy	7.5 7.5		-	2	2	-		2	15.4 38.4	Durgunoglu and Olgun [31]
26	Axis Shopping Mall	Kaigthane	single anchored +multi propped	Diaphragm wall	Soft clay overlying	Gungoren Trakya	17		-			-	1280000	1	100	Durgunoglu et al. [28]
27	Faco Medicine Factory Project	Levent-Besiktas	Multi anchored	65 cm diameter bored pile 25 cm diameter micropile	Graywacke	Trakya	22 18		1.5 1.5	3.2 2.7	1.95 2.1	-	115000 2350	1 1	45 36	Adatepe et al. [33]
28	Siyavuspasa Underground Parking Lot Project	Bahcelievler	Multi anchored	80 cm diameter bored pile	Fill overlying Hard clay	Fill Gurpinar	11		3	2.25	1.7	-	312500	4	10.1	Unpublished data

H is the excavation depth, H_w is the depth of the underground water level from the surface, H_{emb} is the embedded wall length, S_v is the vertical distance between the anchor or soil-nailing levels, S_h is the horizontal distance between the anchor or the soil nailing, η is the nail density (m/m^2), EI is the wall stiffness, n is number of the inclinometers in a project, $\delta_{h,max}$ is the maximum lateral wall displacement in Table 5.

The anchor properties in the anchored wall projects are given in Table 6.

4 DATA ANALYSIS

4.1 Analysis of soil-nailed wall data

Soil nailing is a useful technique for constructing excavations by reinforcing with fully bonded steel bars. The reinforced surface is stabilized with sprayed concrete, which creates a zone similar to a conventional gravity retaining wall. However, this sprayed concrete face does not play a vital role in the structural stability of the soil-nailed wall system. The inclination to the vertical of the wall, the soil condition, the excavation depth and the nail density per unit length of the wall (m^2/m) can be considered important factors affecting the performance of the wall system. Figure 4 shows the relationship between the maximum lateral displacement of the wall ($\delta_{h,max}$) and the excavation depth (H) for soil-nailed shotcrete wall systems. The data shown in Figure 4 are from projects 5, 6, 8, 11, 15, 17, 18, 20, 21, 23 and 25.

There is a clear relationship between $\delta_{h,max}$ the maximum lateral displacement and the excavation depth. The data of $\delta_{h,max}$ generally range from 0.05%H to 0.35%H

Table 6. Anchor Properties for anchored walls.

Project No	Project Name	Excavation Depth (m)		Number of Anchor Rows	Anchor Length (m)		Tendon Diameter (")	EA (kN/m)	Allowable Tensile Capacity (KN)
		Min.	Max.		Min.	Max.			
1	Baumax AVM	15.80		6	20	25	0.6	112000	728
2	Karabulut Textile Factory	8		3	20	14	0.6	84000	545
3	BusinessPort	18	21.60	5-8	12	22	0.6	84000	545
4	Taksim Residence	18.7	19.65	?	?	?	0.6	84000	545
5	Bomonti Hotel and Congress Center	22.8	26	11	12	28	0.6	84000	545
7	Otoport	21	25	10	35		0.6	84000	545
9	Ideal Hospital	29.2		11	18	32	0.6	140000	910
10	Metal Co. Factory	5.25	9.25	3-4	13	19	0.6	84000	545
13	Erdem Hospital	16.3		7	19	30	0.6	84000	545
14	Filiz Co. Factory	18.2		6	14	25	0.6	84000	545
16	Ozbas Residence	22.7	25.9	12	13	35	0.6	84000	545
19	Zeytinburnu Parking lot	11.3		4	14	20	0.6	84000	545
22	Terramix	11.5	13.4	4-5	14	26	0.5	59200	385
24	Cultural Center	8-17.6		3-8	12	19	0.6	84000	545
27	Faco Medicine Factory	18	22	7-9	13	22	0.6	84000	545
28	Siyavuspasa Parking lot	11		4	14	21	0.5	59200	385

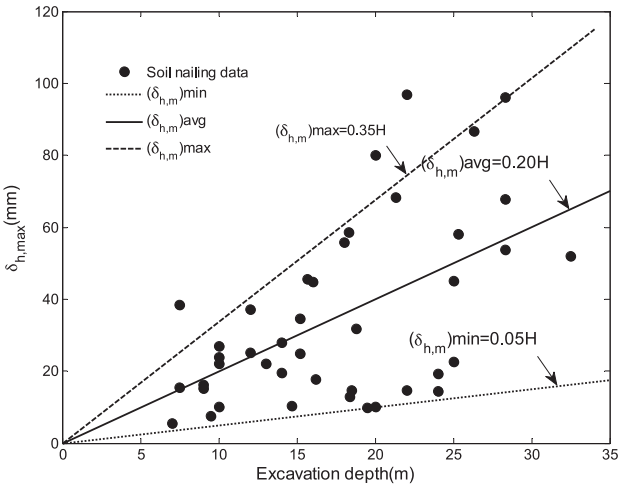

Figure 4. Relationship between maximum wall displacement and excavation depth for soil-nailing data.

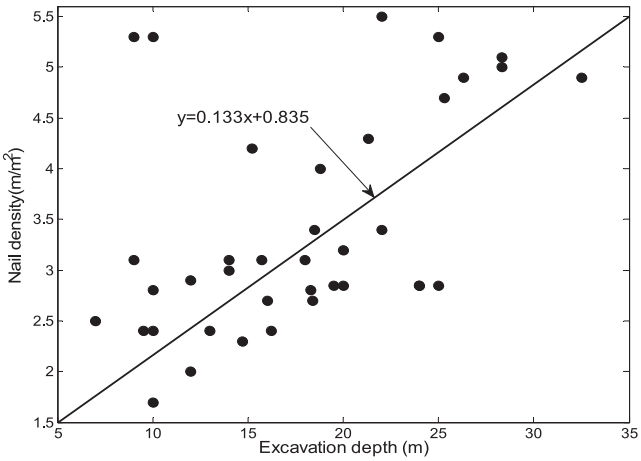

Figure 5. Relationship between nail density and excavation depth.

with an average value of 0.20%*H*. Except for projects 8 and 23, all the data shown in Figure 4 were obtained from projects carried out in the Trakya formation that is mainly composed of claystone-sandstone-mudstone, from extensively fractured to highly fractured. With a few exceptions, it can be said that the distribution of the data is within very reasonable limits. The data outside the limit are from Projects 17 and 25. Project 17 was conducted in the Gurgoren formation, which, composed of soft clay layers, is a weak soil formation in comparison to the Trakya formation. The excavation depth and the maximum wall displacement as a percentage of excavation depth were 7.5 m and 0.51%*H*, respectively, for project 17. It can be said that the wall movement beyond the maximum limit was due to the weak soil condition. In project 25 there were 9 inclinometers. The data from 7 inclinometers are within the limits, while the data from only 2 inclinometers are outside the limits. Sometimes, unexplained, excessive wall movement can be seen in projects that have very long facades.

Generally, the inclination of the wall varies between 5° and 11° to the vertical in soil-nailing projects. This inclination has some positive effects on the performance of the wall, such as a lower earth pressure, a lower soil density and a better safety factor in comparison with the condition of a zero wall inclination to the vertical. Mittal [34] conducted a study on the effects of the variation of some design parameters, such as the nail length, the nail inclination and the wall inclination, on the safety of the wall. It was found that the safety factor of the wall system increases uniformly with an increasing wall inclination up to 20° to the vertical. Beyond this angle, the dimension of the increase of the safety factor of the wall system is very high.

4.1.1 Influence of nail density

The nail density can be calculated as follows:

$$\eta = L/s_v\, s_h \;\; [1, 35] \qquad (1)$$

where η is the nail density, L is the average nail length, s_v is the vertical distance between the nail levels and s_h is the horizontal distance between the nails.

Figure 5 shows the relationship between the nail density and the excavation depth. The nail density increases with the height of the soil-nailed wall. With the exception of a few points, the data are evenly distributed on both sides of the slope line.

Figure 6 (next page) shows the relationship between the nail density and maximum wall displacement.

The data are scattered over a wide range. Increasing the nail density is a natural consequence of increasing the excavation depth. Therefore, the nail density should be considered in conjunction with the excavation depth. It can be said that increasing the nail density is not a decisive factor solely on the performance of the wall.

4.2 Analysis of anchored wall data

The data for five different wall types were collected and analysed. Figure 7 shows the relationship between the maximum wall displacement and the excavation depth depending on the type of wall.

Similar to the soil-nailing data, there is a clear relationship between the maximum lateral displacement and the excavation depth. The data of $\delta_{h,max}$ generally range

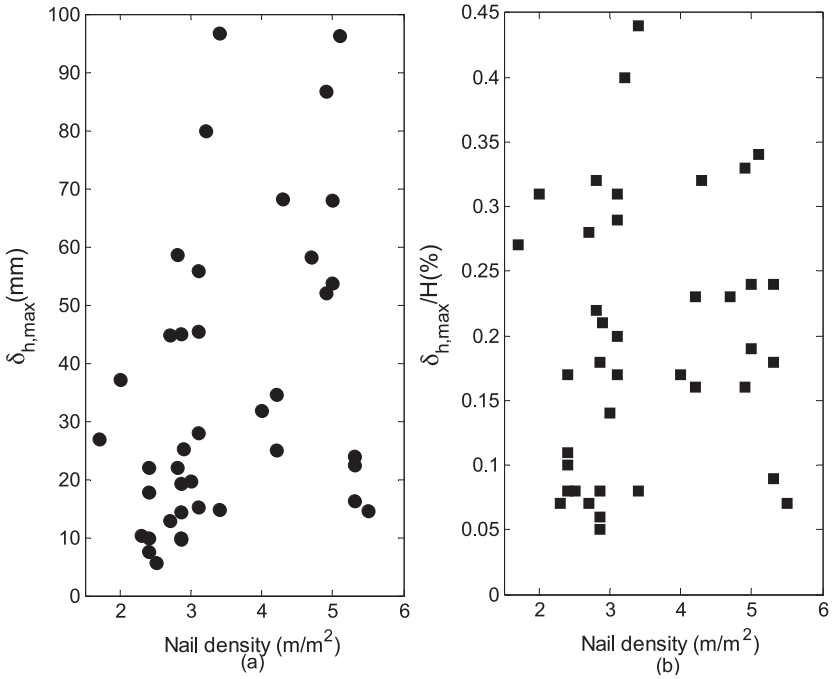

Figure 6. Relationship between nail density and maximum wall displacement.

from 0.043%*H* to 0.32%*H* with an average value of 0.155%*H*. With a few exceptions, it can be said that the distribution of the data is within very reasonable limits. The data from project 26 were obtained from soft clay overlying sandstone. The excavation depth was 17 m, which can be considered as a large depth. Although the wall type was a diaphragm wall, which has a high wall stiffness, the weak soil conditions combined with the large excavation depth may have caused high wall movements in practice.

The secant pile wall and the diaphragm wall systems are used to prevent water flow into the excavation site if the underground water level is above the final excavation depth. Although the data for the secant pile wall (SCW) and the diaphragm wall (DW) are

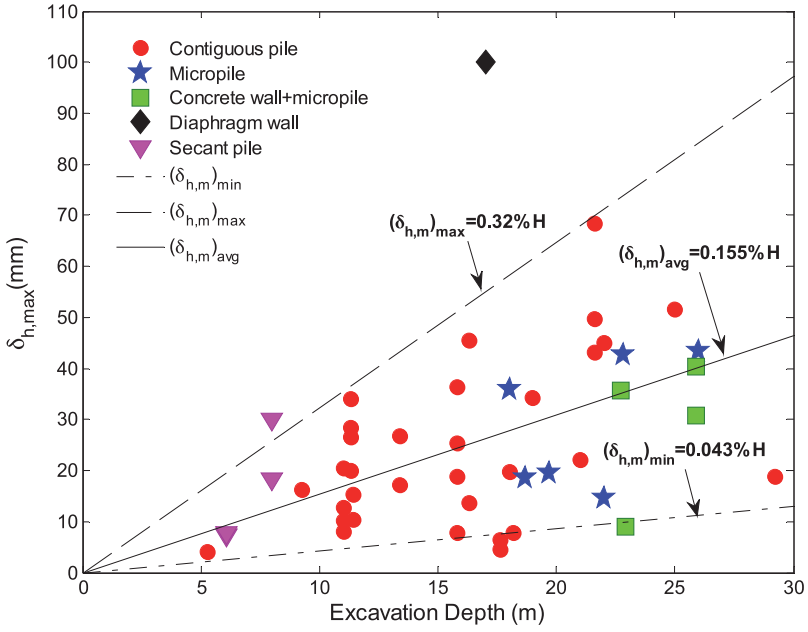

Figure 7. Relationship between maximum wall displacement and excavation depth depending on the type of wall.

very limited, it can be seen in Fig. 7 that the $\delta_{h,max}$ values from the SCW and DW projects are close to or over the max line. This limited data indicate that the underground water level should be taken into account very carefully in the design stage of the wall. MPW and MPW+CW data show that this type of wall has a very good performance in the soil conditions mentioned. As for contiguous pile walls (CPW), the data are generally between the maximum line and minimum line up to an excavation depth of H=20 m. However, for excavation depths greater than H=20 m, the data are above the average line and below the maximum line. An excavation depth of 20 m can be considered as a threshold for a CPW.

Table 7 shows the results obtained from projects 1, 2, 7 and 13 and the results given by some researchers for soft clay soil conditions regardless of the construction method or wall type.

Table 7. Comparison of this study's results with other studies for soft-to-stiff clay condition.

Study	$\delta_{h,max}$ / H			Soil Condition	Note
	Min.	Avg.	Max.		
This study (project 2, 7, 13, 22)	0.09	0.18	0.37	Soft-to-stiff clays	Four different project results
Goldenberg et al. [20]		0.90		Soft-to-stiff clays	Case histories collection
Bentler [37]		0.452		Soft-to-stiff clays	Case histories collection
Wang et al. [36]		0.452		Soft-to-stiff clays	Case histories collection
Kung et al. [38]		0.39		Taipei clay	Case histories collection
Ou et al. [15]		0.40		Taipei soft soil	Case histories collection

As can be seen in Table 7, the average limit of lateral movement for soft-to-stiff clays is 0.18%H. This is smaller than the values given by Goldenberg et al. [20], Bentler [37], Wang et al. [36], Kung et al. [38] and Ou et al. [15].

Long [21] presented a database consisting of about 300 case histories collected from different soil conditions with different wall and support types. As a result of an intensive analysis, it was found that the normalized maximum lateral movement values, $\delta_{h,max}$, are mostly between 0.05%H and 0.25%H, where H is the excavation depth. In this paper, for soil-nailing data, the maximum lateral movement values range from 0.05%H to 0.35%H with an average value of 0.20%H, and for anchored wall data, the maximum lateral movement values range from 0.043%H to 0.32%H with an average value of 0.155%H. The maximum lateral values presented by Long [21] and the maximum lateral values presented in this study differ only slightly from one another.

Tomlinson [40] reviewed 34 case histories of deep excavations conducted with different methods. The results were grouped into three major categories of ground condition. For soft-to-firm NC clays, $\delta_{h,max}$ ranges from 0.08%H to 0.58%H with an average value of 0.30%H, for stiff-to-hard OC clays, $\delta_{h,max}$ ranges from 0.06%H to 0.30%H with an average value of 0.16%H and for sands and gravels, $\delta_{h,max}$ ranges from 0.04%H to 0.46%H with an average value of 0.19%H. Projects 1, 10, and 14 were conducted in hard clay. For these projects, $\delta_{h,max}$ ranges from 0.04%H to 0.23%H with an average value of 0.12%H, which are close to the values reported by Tomlinson [40] for hard clays.

A total of 536 case histories were collected and analysed by Moorman [23]. These case histories were classified into five categories in terms of the ground condition. For stiff clays in Moorman's database, the upper limit of the maximum lateral movement is 1%H and most of the data are under the 0.5%H limit. These values are higher than the values obtained from projects 1, 10 and 14 in this study. For very limited data from a deep excavation conducted in rock, the upper limit of the maximum lateral movement is 0.5%H and most of the data are under the 0.25%H limit. In this study, most of the data for the maximum lateral movement obtained from projects conducted in a rock formation are under 0.20%H, which is very close to the value for a deep excavation conducted in a rock formation presented by Moorman [23].

4.2.1 Influence of embedded depth ratio

The embedded depth ratio can be expressed as follows,

$$R_{emb} = H_{emb} / H \qquad (2)$$

where H_{emb} is the embedded depth of the wall and H is the excavation depth (m). This ratio is an important factor that reflects the economy of the wall [36]. Figure 8 shows the relationship between the maximum wall displacement and the embedded depth ratio of the wall.

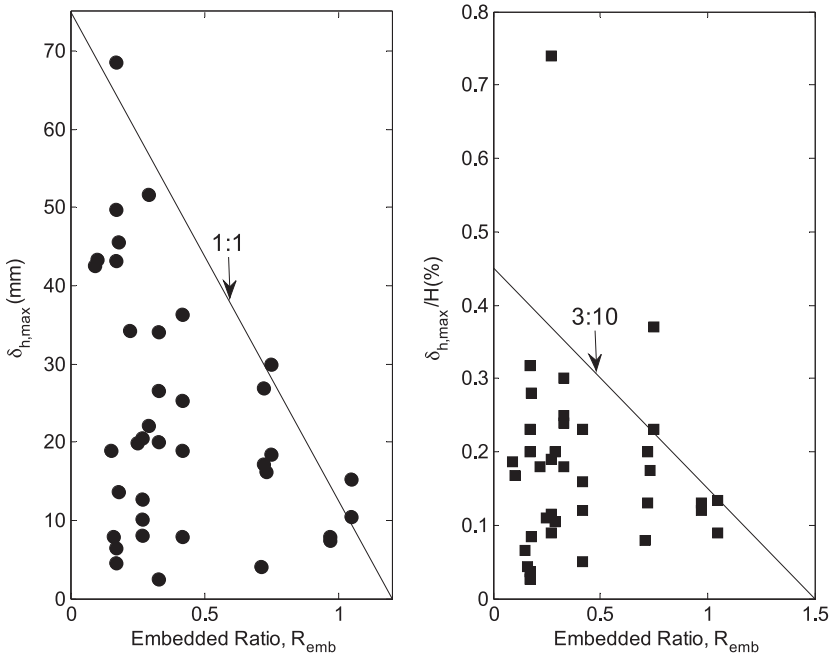

Figure 8. Relationship between maximum wall displacement and the embedded depth ratio of the wall.

The dimensions of the maximum wall displacement are shown in mm units in Fig. 8(a), while they are shown as a percentage of $\delta_{h,max}/H$ in Fig. 8(b). Although the dimensions of the maximum wall displacement were expressed in two different ways, it can be seen that there is a clear trend that the embedded ratio increases while the lateral displacement, or $\delta_{h,max}/H$ ratio, decreases in accordance with the inclination line (Fig.8 (a) and (b)).

Projects 2 and 22 have a higher embedded ratio. Project 2 was conducted in very soft clay soil conditions. There was a risk that the anchors would not work because of the soft soil conditions. Therefore, the embedded ratio selected was very high. Similarly, project 22 was conducted in clay soil that had a landslide risk. Thus, the embedded ratio selected was more than 1. According to the displacement value of the wall, it can be said that a

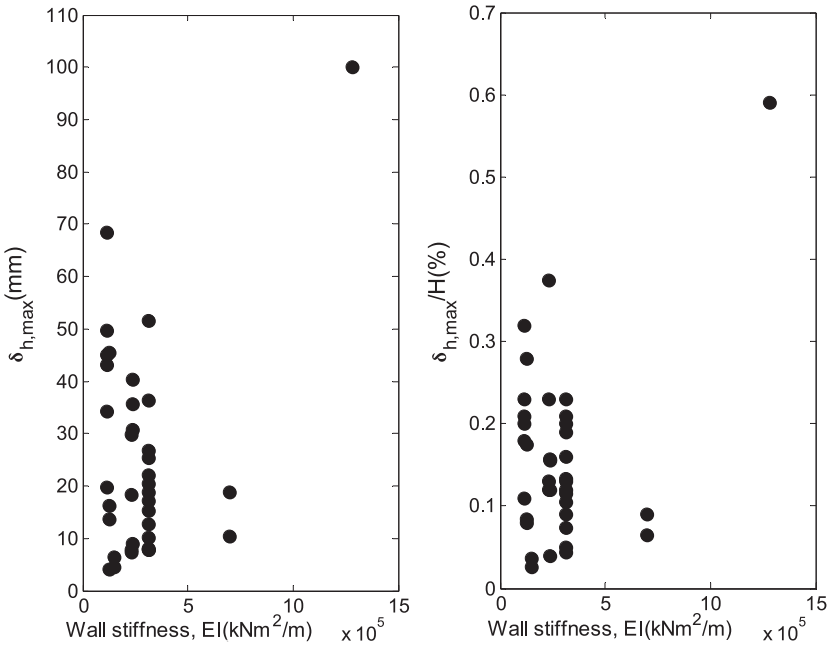

Figure 9. Relationship between maximum wall displacement and wall stiffness.

high embedded ratio is a strong parameter to prevent excessive displacements provided that selection of high wall stiffness in soft soil conditions.

4.2.2 Influence of wall stiffness

Wall stiffness can be expressed as *EI*, where *E* is the elasticity modulus of the concrete and I is the moment of inertia of the wall. Figure 9 shows the relationship between the maximum wall displacement and the wall stiffness.

There is no definite information about the thickness of the shotcrete walls. The wall stiffness of the anchored walls was considered in this analysis. Figure 9 shows the data obtained from projects with large-diameter pile walls. Except for projects 9 and 26, the wall stiffness of the anchored pile walls is less than 500,000 kNm^2/m and the data from anchored pile walls vary from 0.05%*H* to 0.45%*H*. There is a large scatter in the data. It can be said that there is no direct or no linear relationship between the wall stiffness and the movements. Hence, it can be interpreted that the wall movements are mainly independent of the wall stiffness. This result is consistent with those reported by Moormann [23], Moormann [39] and Long [21].

This study is the first attempt to prepare a deep-excavation database for Istanbul. Although there are limited data for some analyses, this database provides a good idea about the dimensions of wall movement. This database can be improved by collecting additional data in the future.

4.2.3 Influence of soil type

All the anchored wall data were plotted in Figure 10 in terms of the main soil type in which the projects were conducted.

The data for the Gungoren formation are around the average line up to an excavation depth of 20 m, after which the data are between the maximum and average lines. For the alluvium data, although the excavation depths are low, the data are between the maximum and average lines. The data for the Gurpinar formation are around the average line. The data from the Trakya formation are far from the maximum line even though the excavation depths are greater than 20 m. Because the data for the fill overlying Trakya formation and the Trakya-Bakirkoy formation are very limited, no interpretation can be made. However, it can be said that the data for the Trakya formation are the best results, regardless of soil type, wall type and support type.

5. CONCLUSIONS

On the basis of the results from this study, the following conclusions can be drawn:

- The results obtained show that successful wall performance can be obtained under a wide variety of soil conditions provided that suitable wall and/or support systems are chosen in the design phase.

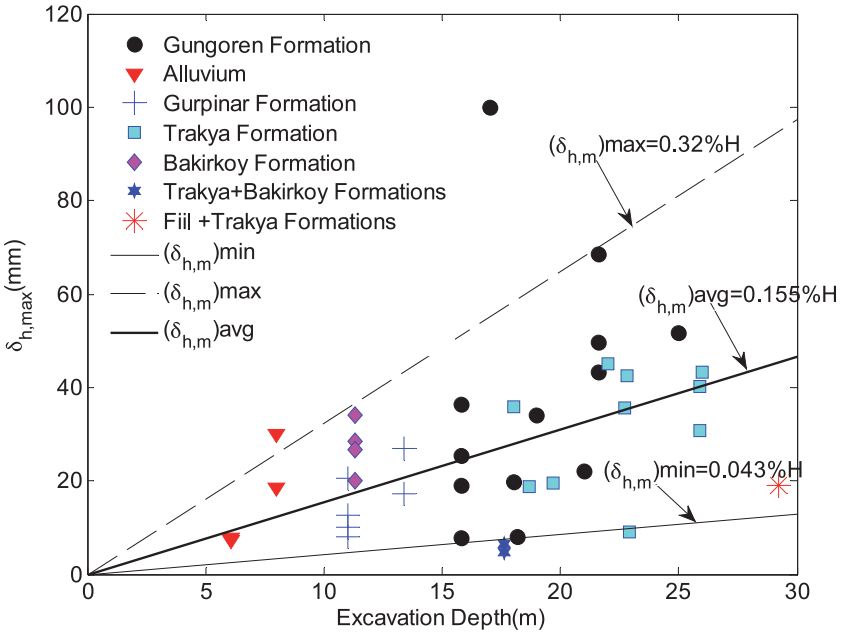

Figure 10. Relationship between maximum wall displacement and excavation depth depending on soil type.

- The maximum lateral displacement of the wall increases with an increasing excavation depth for all types of walls. The data for the SCWs and DWs are close to or over the max line. These limited data show that the underground water level should be taken into account very carefully in the design stage. The data for the MPWs and MPWs + CWs show that these types of walls perform well. The data for CPWs are generally between the max line and min line up to a H=20 m excavation depth. However, for an excavation depth over H=20 m, the data are above the average line and between the average and maximum lines. An excavation depth of H=20 m can be considered as a critical excavation depth for CPWs.
- The data for $\delta_{h,max}$ generally range from 0.05%H to 0.35%H with an average value of 0.20%H in soil--nailed projects. The data for $\delta_{h,max}$ generally range from 0.043%H to 0.32%H with an average value of 0.155%H in anchored pile wall projects
- The nail density increases with the height of soil--nailed walls. It should average 2.2 m/m^2 for H=10 m, 3.5 m/m^2 for H=20 m and 4.8 m/m^2 for H=30 m, according to the data obtained from projects conducted in Istanbul.
- With regard to soil-nailing shotcrete wall systems, it can be said that a soil-nailed shotcrete wall system is a very suitable system in rock conditions if there is no adjacent structure or infrastructure.
- Wall inclination to the vertical is an important factor to be able to obtain good performance for soil--nailing projects.
- In light of the analysis, there is a clear trend that the maximum wall displacement decreases with an increasing embedded ratio. Especially in soft soil conditions, a high ratio should be chosen to be able to prevent excessive soil and wall movements. However, this ratio is also related to the economics of the project. Therefore, this ratio should provide both safety and economy at the same time.
- There is no linear relationship between the wall stiffness (EI) and the wall movements ($\delta_{h,max}$). A number of different $\delta_{h,max}$ values can be seen for the same EI values. In this case, the excavation depth is a more important parameter than the embedded ratio.
- Soil type has an important influence on the dimensions of wall movement. The project conducted in the Trakya formation had the best results in terms of wall movement. Down to an excavation depth of 20 m, the wall movements for the projects conducted in the Gungoren formation are around the average line. However, beyond an excavation depth of 20 m designers should be careful in the design process for projects in the Gungoren formation.

Acknowledgements

The author would like to thank C.E. Mahmut Candan and Geoform Engineering and Consultancy Company for their help with the data collection.

REFERENCES

[1] Keskin, B. 2008. Analysis of the performance of retaining systems in deep excavations in graywackes. Ph.D. Thesis, Bogazici University, Istanbul, Turkey.

[2] Hashash, Y.M.A., Song, H., Osouli, A. 2011. Three-dimensional inverse analyses of a deep excavation in Chicago clays. Journal for Numerical and Analytical Methods In Geomechanics 35, 1059-1075.

[3] Ma, J., Berggren, B., Bengtsson, P.E., Stille, H., Hintze, S. 2008. Behavior of anchored walls in soils overlying rock in Stockholm. International Journal of Geoengineering Case Histories, 2(1), 1-23.

[4] Yoo, C., Lee, D. 2008. Deep excavation-induced ground surface movement characteristics – A Numerical Investigation. Computers and Geotechnics 35, 231–252.

[5] Peck, R.B. 1969. Deep excavations and tunneling in soft ground state-of-the-art report. Proceedings of 7th International Conference on Soil Mechanics and Foundation Engineering, Mexico.

[6] Hwang, R.N., Moh, Z.C. 2007. Deflection paths and reference envelopes for diaphragm walls in Taipei Basin. Journal of GeoEngineering 2(1), 1-12.

[7] Cheng, M.Y., Wu, Y.W. 2009. Prediction of diaphragm wall deflection in deep excavations using evolutionary support vector machine inference model (ESIM). 26th International Symposium on Automation and Robotics in Construction, Austin, Texas, 176-182.

[8] Finno, R.J., Bryson, S. 2002. Response of building adjacent to stiff excavation support system in soft clay. Journal of Performance of Constructed Facilities 16(1), 10-20.

[9] Ou, C.Y., Teng, F.C., Wang, I.W. 2008. Analysis and design of partial ground improvement in deep excavations. Computers and Geotechnics 35, 576–584.

[10] Hou, Y.M., Wang, J.H., Zhang, L.L. 2009. Finite-element modeling of a complex deep excavation in Shanghai. Acta Geotechnica 4, 7–16.

[11] Wong, I., Chou, T.S.H. 1998. Ground movements due to pile driving in an excavation in soft soil. Canadian Geotechnical Journal 36(1), 152-160.

[12] Goldberg, D.T., Jaworski, W.E., Gordon, M.D.

1976. Lateral support systems and underpinning. Rep. FHWA-RD-75-128, Federal Highway Administration, Washington D.C.
[13] Mana, A.I., Clough, G.W. 1981. Prediction of movements for braced cuts in clay. Journal of Geotechical Engineering 107(6), 759-777.
[14] Clough, G.W., O'Rourke, T.D. 1990. Construction induced movements of in situ walls. Proc., ASCE Conf. on Des. and Perf. Of Earth Retaining Struct Geotech. Spec. Publ., ASCE, 25, 439–470.
[15] Ou, C.Y., Hsieh, P.G., Chiou, D.C. 1993. Characteristics of ground surface settlement during excavation. Canadian Geotechnical Journal 30, 758–767.
[16] Wong, L.W., Patron, B.C. 1993. Settlements induced by deep excavation in Taipei. Proc., 11th South Asian Geotechnical Conference, Singapore, 787-791.
[17] Carder, D.R. 1995. Ground movements caused by different embedded retaining wall construction techniques. Transport Res. Lab. Rep. 172, Berkshire, U.K.
[18] Fernie, R., Suckling, T. 1996. Simplified approach for estimating lateral movement of embedded walls in U.K. ground. Proc., Int. Symp. on Geo Aspects of Underground Construction in Soft Ground, London, England.
[19] Wong, I.H., Poh, T.Y., Chuah, H.L. 1997. Performance of excavations for depressed expressway in Singapore. Journal of Geotechnical and Geoenvinromental Engineering 123(7), 617–625.
[20] Hsieh, P.G., Ou, C.Y. 1998. Shape of ground surface settlement profiles caused by excavation. Canadian Geotechnical Journal 35(6), 1004–1017.
[21] Long, M. 2001. Database for retaining wall and ground movements due to deep excavations. Journal of Geotechnical and Geoenvinromental Engineering 127(3), 203-224.
[22] Yoo, C. 2001. Behavior of braced and anchored walls in soils overlying rock. Journal of Geotechnical and Geoenvironmental Engineering 127(3), 225–233.
[23] Moormann, C. 2004. Analysis of wall and ground movement due to deep excavation in soft soil based on a new worldwide database. Soils and Foundations 44(1), 87-98.
[24] Leung, E.H.Y., Charles, W.W.Ng. 2007. Wall and ground movements associated with deep excavations supported by cast in situ wall in mixed ground conditions. Journal of Geotechnical and Geoenvironmental Engineering 133(2), 129-143.
[25] Istanbul Metropolitan Municipality (IBB) 2007. Microzonation work for the southern European side of Istanbul.
[26] Istanbul Metropolitan Municipality (IBB) 2009. The second stage of microzonation work for the Asian side of Istanbul.
[27] Terzaghi, K., Peck, R.B. 1967. Soil mechanics in engineering practice, 2nd Edition, Wiley, NewYork.
[28] Stark, T.D., Choi, H. 2008. Slope inclinometers for landslides. Lanslides 5, 339-350.
[29] Cetin, E., Bayrakli, Y., Güler, E. 2004. An example of a deep excavation pit's project. Journal of Turkey Engineering News (Türkiye Mühendislik Haberleri Dergisi) 431(3), 27-32.
[30] Yilmaz, S., Kulac, H.F., Durgunoglu, H.T. 2000. Behavior of the soil nailed wall in different soil condition. 8th National Congress of Soil Mechanics and Foundation Engineering, Istanbul, Turkey.
[31] Olgun, C.G., Durgunoglu, H.T. 1996. Soil nail practice in Istanbul. 10th European Young Geotechnical Engineers Conference, Izmir, Turkey, 274-283.
[32] Durgunoglu, H.T., Kulac, F., Ikiz, S., Gunay, Akcakal, O. 2012. Selecting of displacement controlled deep excavation retaining system in soft clay. 14th National Congress of Soil Mechanics and Foundation Engineering, Isparta, Turkey.
[33] Adatepe, S., Gokalp, A., Duzceer, R. 2012. Performance of the different retaining systems in a deep excavation project carried out in Istanbul graywacke. 14th National Congress of SoilMechanics and Foundation Engineering, Isparta, Turkey.
[34] Mittal, S. 2006. Soil nailing application in erosion control-an experimental study. Geotechnical and Geological Engineering 24, 675-688.
[35] Phear, A., Dew, C., Ozsoy, B., Wharmby, N.J., Judge, K., Barley, A.D. 2005. Soil Nailing - Best Practice Guidance, CIRIA C637, London.
[36] Wang, J.H., Xu, Z.H., Wang, W.D. 2010. Wall and ground movements due to deep excavations in Shanghai soft soils. Journal of Geotechnical and Geoenvinromental Engineering 136(73), 985-994.
[37] Bentler, D.J. 1998. Finite element analysis of deep excavations. Faculty of Viriginia Polytechnic İnstitute and State University Blacksburg, Virginia.
[38] Kung, G.T.C., Juang, C.H., Hsiao, E.C., Hashash, Y.M.A. 2010. Simplified model for wall deflection and ground-surface settlement caused by braced excavation in clays. Journal of Geotechnical and Geoenvinromental Engineering 133(6), 731-747.
[39] Moormann, C. 2002. Trag-und verformungsverhalten tiefer Baugruben in bingigen Böden unter besonder Berücksichtigung der Baugrund-Tragwerk und der Baugrund-Grundwasser-Interaktion(in German), Ph.D. Thesis, Technical University Darmstadt, Germany.
[40] Tomlinson, M.J. 1995. Foundation design and construction. 6th Edition, Longman, Harlow.

METODA NAPOVEDOVANJA DEFORMACIJ NABREKLJIVIH GLINENIH ZEMLJIN IN OBLIKOVANJE PLITVIH TEMELJEV, KI SO PODVRŽENI DVIGANJU

Baheddi Mohamed
University of Batna,
Department of Civil Engineering, laboratory L.R.N.A.T.
05000, Alžirija
E-pošta: baheddi_md@yahoo.fr

Djafarov Mekhti
Azerbaijan Civil Engineering University,
Laboratory of Soil Mechanics,
A. Sultanova st 5, Baku 370073, Azerbajdžan
E-pošta: md13djafarov@gmail.com

Charif Abdelhamid
King Saud University,
College of Engineering
P. O. Box 800, Riyadh 11421, Savdska Arabija
E-pošta: abdelhamid_charif@caramail.com

Ključne besede

nabrekljiva zemljina, velikost nabrekanja, pritisk nabrekanja, prosti edometrski preizkus nabrekanja, obremenitveni edometrski preizkus nabrekanja, plitvi temelji

Izvleček

Nabrekljive zemljine je mogoče najti v mnogih delih sveta. Stanje prakse na tem področju se spreminja v zadnjih desetletjih. Projektiranje temeljev v nabrekljivih tleh predstavlja pomemben izziv za inženirje. Pretirana škoda nastane deloma zaradi pomanjkanja ustreznega načrtovanja, zaradi česar je potreba po boljših orodij za projektante, da bi se ocenil vpliv nabrekljivih tal v tipičnih projektnih situacijah. Za natančno napovedovanje dvigovanja tal je potrebno pravilno merjenje tlaka nabrekanja.

Predlagan je teoretični model, s katerim je opisan potencial nabrekljivih glinenih tal, karakteristike glin so pridobljene iz edometrskih preizkusov. Prispevek opisuje analizo obnašanja nabrekljive zemljine pri povečani vlažnosti pod zgradbami in objekti. Metode in načela, ki se trenutno uporabljajo za oblikovanje konstrukcij temeljev na nabrekljivih zemljinah, so zaradi neenakomerne deformacije teh zemljin pri obremenitvah, problematična. Pričujoča študija je bila izvedena za izračun dviganja plitvih temeljev na nabrekljivih tleh, z upoštevanjem spremembe vlažnosti zemljine, kot tudi porazdelitve kontaktnih tlakov pod temelji.

A METHOD FOR PREDICTING THE DEFORMATION OF SWELLING CLAY SOILS AND DESIGNING SHALLOW FOUNDATIONS THAT ARE SUBJECTED TO UPLIFTING

Baheddi Mohamed
University of Batna,
Department of Civil Engineering, laboratory L.R.N.A.T.
05000, Algeria
E-mail: baheddi_md@yahoo.fr

Djafarov Mekhti
Azerbaijan Civil Engineering University,
Laboratory of Soil Mechanics,
A. Sultanova st 5, Baku 370073, Azerbaijan
E-mail: md13djafarov@gmail.com

Charif Abdelhamid
King Saud University,
College of Engineering
P. O. Box 800, Riyadh 11421, Saudi Arabia
E-mail: abdelhamid_charif@caramail.com

Keywords

swelling soil, swelling magnitude, swelling pressure, free-swell oedometer test, loaded-swell oedometer test, shallow foundations

Abstract

Swelling soils can be found in many parts of the world. The state of practice in this area has been changing over recent decades. The design of foundations for expansive soils is an impo rtant challenge facing engineers. The excessive damage is, in part, due to the lack of proper design, resulting in the need for better tools for practitioners in order to assess the impact of swelling soils in typical design applications. A correct measurement of the swelling pressure is required for an accurate prediction of the heave. A theoretical model is proposed to describe the swelling potential of clay soils on the basis of their characteristics obtained from oedometer tests. This paper describes analysis of the behavior of swelling soils when moistened under buildings and structures. The methods and principles currently used for the design of structure foundations on swelling soils involve important problems due to the non-uniform deformations of these soils when subjected to structural loads. The current study was conducted to compute the uplifting of shallow foundations on swelling soils considering the water-content change as well as the contact-pressure distribution under the footing.

1 INTRODUCTION

In any geotechnical study relative to a construction project, the swelling of a soil is as important as the settlement. The dimensional variations that, result from this phenomenon, constitute a permanent challenge for design and geotechnical engineers. The durability of a structure constructed on swelling soils depends on an appropriate appreciation of the phenomenon.

The swelling of clay soils, containing smectites or illites in different quantities, is the origin of numerous problems in buildings and large structures. These disturbances are frequent in regions with a dry climate like some parts of the Caucasus parts, in Kazakhstan, Algeria, Morocco, etc.

The swelling of soils can provoke important material damages, or even partial to total rupture of the structure, when it is not considered in the design process. It is therefore important to foresee correctly the possible distortions of swelling soils, in terms of amplitude and the speed of evolution, and to analyze its influence on the serviceability and stability of the structure.

Swelling soils have been a major concern for designers over many years. Some construction procedures have been developed to limit the effects of inflation on the constructions and can be found in the classic works, of., Lancelot L et al., Mouroux et al. (in French) [19] [22],

Sorochan E.A., Mustafaev A.A. (in Russian) [27] [23], and Chen F.H. (in English) [7].

Currently, an abundance of documentation explains the mechanisms for the swelling of clays, either at the microscopic level as in test tubes tested in the laboratory or in-situ soil. Nevertheless, a survey of the behavior of the structures in contact with swelling soils constitutes a complex task and the existing methods contain some insufficiencies. Most of the research carried out, is limited to the amplitudes of the inflation of the clay soils in nature, under loads of spread foundations. Little attention has been given the propagation of the inflation phenomena in the mass of the swelling soils as a function of time.

2 IDENTIFICATION OF THE MATERIAL.

The studied swelling clay comes from the Urban District of Baku (Azerbaijan) where it has provoked many disturbances in the structures of a concrete channel. The tests were carried out on samples of undisturbed clay soil, of the Pliocenes era, collected from the Shamour channel "Apcheron", (Baku) in the soil mechanics laboratory of the Civil Engineering Institute of Baku (Figures 1 to 3).

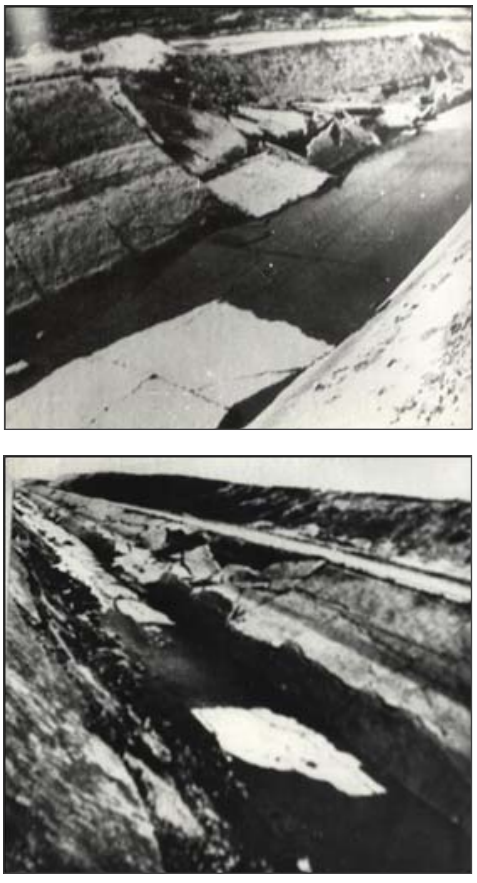

Figure 1. Example of disorders in the construction of the " Samour –Apcheron " concrete channel.

2.1 Mineralogical analysis

A diffractometry analysis using X-rays was performed to determine the mineralogy of the studied soils. The physical and mechanical properties are given in Table 1.

A chemical analysis of the samples of inflating clays gave the following compositions:

Table 1. Physical and mechanical characteristics of the studied clay soils.

Soil characteristics	Symbols	Unit	Values
Natural water content	W	%	10–16
Degree of saturation	S_r	%	83–91
Wet Unit Weight	γ_h	kN/m^3	21.6–22.5
Dry Unit Weight	γ_d	kN/m^3	17.7–18.3
Specific Unit Weight	γ_s	kN/m^3	27.3–27.4
Voids Ratio	e	%	49.6–54.2
Porosity	n	%	33–35
Liquid Limit	W_L	%	46–51
Plastic Limit	W_P	%	24–32
Plasticity Index	I_P	%	19–22
Liquidity Index	I_L	%	-41.0 to -74.0
Coefficient of compressibility	a_v	1/MPa	0.08
Modulus of distortion between 0.1– 0.2MPa	E	MPa	
- At natural water content			7.0–7.8
- After saturation			6.0–7.2
Cohesion	C	MPa	
- At natural water content			0.2–0.58
- After saturation			0.08–0.14
Internal friction angle	φ	Degree	
- At natural water content			25–31
- After saturation			17–23
Grain size distribution			
- 0.5 - 0.25 mm	%		–
- 0.25 - 0.1 mm	%		–
- 0.1 - 0.05 mm	%		18.26
- 0.05 - 0.01 mm	%		23.58
- 0.01 - 0.005 mm	%		11.79
- 0.005 - 0.001 mm	%		46.37

Table 2. Chemical composition of the studied clays.

N° of the sample	Units	Denomination							
		Na^+K	Ca^{++}	Mg^{++}	Cl	SO_4	HCO_3	CO_3	PH
1	%	13.88	1.49	0.33	7.3	6.59	1.19	0.63	7.5
2	%	12.18	1.69	0.33	7.30	5.42	0.89	0.59	7.8
3	%	13.88	1.29	0.25	7.30	6.84	0.89	0.39	7.8

SiO_2: 52.28 %	Al_2O_3: 15.27 %	Na_2O: 2.73 %
K_2O: 2.59 %	MgO: 2.45 %	CaO: 6.70 %
TiO_2: 0.79 %	MnO_2: 0.10 %	Fe_2O_3: 6.77 %

The chemical analysis by using the method of dosage of the elements composing the swelling clay produced the results in Table 2.

Figure 2. Test of inflation in a free cell oedometer (without piston).

Figure 3. Swelling test in an oedometer under load.

3 EXPERIMENTAL ANALYSIS AND INTERPRETATION OF THE RESULTS

The swelling rate corresponds to the relative variation in volume (%) of a sample either unloaded or subjected to a small load (generally the weight of the piston in the oedometer) when it is put into contact with water without pressure. The pressure of swelling is consists of an "osmotic" component due to the difference in the concentration of salts of the interstitial water and a "matrix" component, governed by the initial negative interstitial pressure of the sample. In most cases "matrix" component plays, a major role.

Numerous methods have been proposed in the literature to evaluate the inflation potential of a soil from measures of the plasticity parameters and grain-size distribution, for example, Delage P. et al [10]., Bigot G., Zerhouni M.I., [6], Zerhouni, M.I., et al. [31], Cokca E., [8], Djedid, A., et al., [12], Cuisinier O. [9], Marcial, et al. [20], Bekkouch et al., [4] [5], Erzin Y.[14], Kariuki PC. [17], Yilmaz I. [30], Nelson, J.D. et al. [24], Tomas PJ., et al. [29]. For these authors, a very high inflation potential corresponds to a free inflation (expressed in percentage) greater than 25%, a high potential to an inflation between 5 and 20%, a medium potential to an inflation between 1.5 and 5%, and a low potential to an inflation lower than 1.5%. Johnson L.D., [16], Komine H. Ogota N [18], Miao L. et al., [21], the corresponding pressures of inflation are, respectively, superior to 300 kPa (very high potential), varying between 200 and 300 kPa (high), between 100 and 200 kPa (medium) and lower than 100 kPa (low).

Several methods exist to measure the pressure of inflation in oedometers, among which we note:

- Method of Huder and Amberg (1970).
- Method of inflation with constant volume, according to ASTM norm D 2487-06.[1].
- Method of inflation or settlement under constant load, which requires several identical samples.
- Free-swelling method followed by reloading.

The experimental studies show that the percentage of soil expansion increases proportionally with its density, its liquid limit, its clay contents, its plasticity and shrinkage indexes, as well as its pressure of pre-consolidation Rao B.H. et al., [25], Thakur VKS, et al., [28], Derriche, Z., et al., [11], Ejjaouani, H., et al. [14], and Fleurau J.M., et al., [15]. A method using the slope of the line connecting the percentage swell for various values of inundation stress was described in Nelson et al. [24]. These same studies report that the pressure of the expanding soil is

inversely proportional to its natural water content.

The analysis of the experimental results [3], allowed us to draw the curves giving the variation of the swelling potential in function of time for different values the compression stresses (Fig 4). It also allowed us to establish various other relations:

Variation of the water content after expansion as a function of the different values of the compression stresses, (Fig 5),

Variation of the expansion potential as a function of the different compression stresses, (Fig.6),

Variation of the inflation potential with the water content in oedometer tests (Fig 7).

The following section is relative to the mathematical model describing the expansion mechanism, established from the oedometric tests.

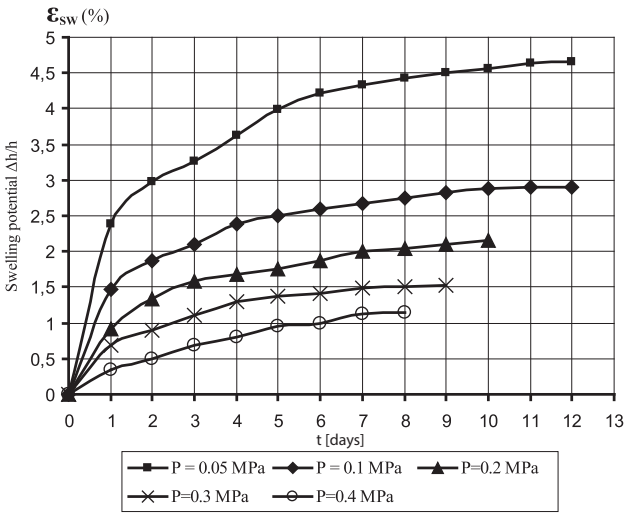

Figure 4. Variation of the swelling potential with time.

The dependence of the water content of an expansive soil, on the compression stresses (after swelling has taken place) can be expressed using an exponential function:

$$W_{sw} = W_{sw}^{0} e^{(-\bar{\gamma}P)} \qquad (1)$$

with: W_{SW}^{0} : Water content without loading ($P = 0$)

and

$$\bar{\gamma} = \left(\frac{1}{P}\right) \ln\left(\frac{W_{sw}^{0}}{W_{sw}}\right) \qquad (2)$$

For the interval of stresses, generally between 50 and 400 kPa in civil and industrial constructions, the dependence between the water content of the expansive soil and the compression stresses can be approximated using the relation.

$$W_{sw} = \overline{W}_{sw} - \chi P \qquad (3)$$

with:

$\overline{W}_{sw}$: Initial value of the water content given by the straight line in Figure 5.
χ : Slope of the curve in Figure 5.

The obtained values are: $\overline{W}_{sw} = 0.24 \quad \chi = 0.2 MPa^{-1}$

In this part, five models for the prediction of the clay expansion according to the geotechnical properties are used. Their formulations are given in Table 3.

Some of these models (Seed et al. and the first model of Vijayvergiya and Ghazzaly) ignore the natural water content.

These models are valid in the range of the expansion amplitude varying from the lower limit of 5 % (the point at which a soil is considered to be expansive) to the upper limit of 60% (the maximum observed expansion). This allows us to determine, from these models, minimum

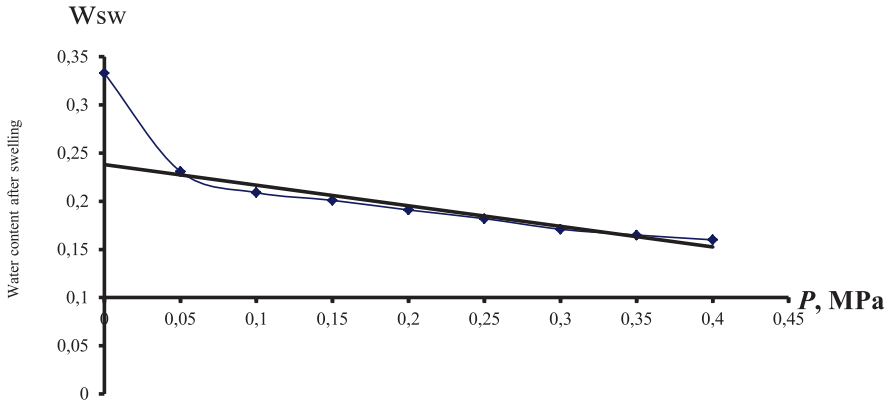

Figure 5. Variation of the water content with different load levels.

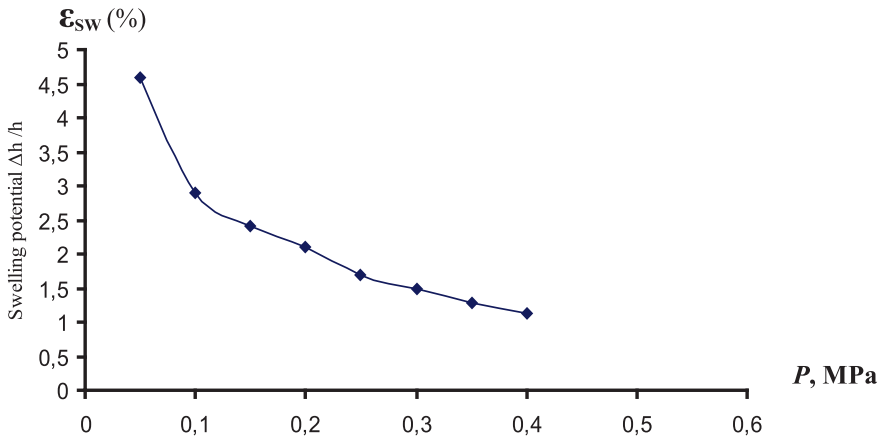

Figure 6. Variation of the inflation potential function of the different loads.

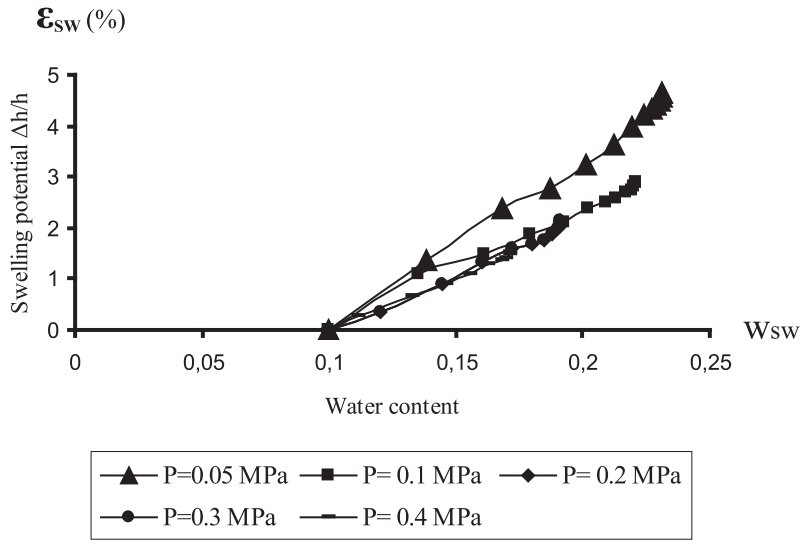

Figure 7. Variation of the swelling potential as a function of the water content.

Table 3. Tested models for predicting the inflation of the clays.

Model	Reference	Mathematical expression
Seed and al.	Seed et al. (1962)	$\varepsilon_{sw} = 2.16.10^{-5} I_P^{2.44}$
Nayak and Christensen	Nayak and Christensen (1971)	$\varepsilon_{sw} = 2.29.10^{-2} I_P^{1.45} \frac{C_2}{W_0} + 6.38$
Vijayvergiya and Ghazaly-1	Vijayvergiya and Ghazzaly (1973)	$\lg(\varepsilon_{sw}) = \frac{62.42\gamma_d + 0{,}65W_L - 130.5}{19.5}$
Vijayvergiya and Ghazaly-2	Vijayvergiya and Ghazzaly (1973)	$\lg(\varepsilon_{sw}) = \frac{0.4W_L - W_0 + 5.5}{12}$
Johnson	Johnson (1978)	Pour I_P<40 $\varepsilon_{sw} = -9.18 + 1.5546 I_P + 0.08424 Z +$ $+ 0.1 W_0 - 0.0432 W_0 I_P - 0.01215 Z I_P$

water content comparable to the shrinkage limit, and maximum water content comparable to the liquid limit.

Mathematically, the prediction models should constitute functional relations between a dependent variable, the percentage of the expansion, and some independent explicative variables.

4 PROPOSITION OF A MODEL FOR THE EXPANSION POTENTIAL OF THE STUDIED CLAYS

The analytical results obtained show that, the variation of the expansion potential is dependent on the value of the compression stresses and the variations of the water content during the swelling process, and is governed by:

$$\varepsilon_{sw} = \varepsilon_{sw}^{0}\left(1-\frac{P}{P_{sw}}\right)\left[\left(\overline{W}_{sw}-W_{0}\right)-\chi P\right] \qquad (4)$$

This analytical expression (4) gives, with good precision, the value of the swelling potential of clay soils on the basis of their properties obtained from oedometer tests. This formula contains the specific features of the expansive soils:

ε_{sw} : Expansion potential.
ε_{sw}^{0} : Expansion potential without loading.
P_{sw} : Expansion pressure.
W_0 : Initial water content.
$\overline{W}_{sw}$: Initial value of water content given by the graph W_{sw}=f(P) (Fig 5).
χ : Slope of the curve in Figure 5.

This expression for the expansion potential is different from that found in the literature, by including a good approximation of its nonlinear relation with loading. The power of the load P in equation (4) does not exceed 2.

5 DESIGN SHALLOW FOUNDATIONS ON EXPANSIVE SOILS

The stress state of the soil foundation is determined by computations calculations based on rules that consider the effect of the pressure of the weight of soil $\sigma_{z,g}$, the weight of the structure $\sigma_{z,p}$ and the supplementary vertical pressure due to the influence of the weight of the non-wetted soil at the boundaries of the wet surfaces.

In determining the value of the uplift of the foundations after swelling the soil depending on the swelling pressure and the stress state of the sub grade, it is necessary to find the position of the boundaries of the swelling zones (II) (Fig. 6).

The main method for determining the boundaries of the areas of the swelling soil is as follows: In general the depth is determined, as the sum of the stresses due to the action of the weight of the soil, the live load and the additional vertical stress due to the non-wetted portion of the soil mass balancing the swelling pressure.

The probable swelling zone of the soil can be between the obtained depths.

Taking this into account, the boundaries of the areas of the swelling soil are determined from the following equations:

$$\sigma_{z,tot} = \sigma_{z,p} + \sigma_{z,g} + \sigma_{z,ad} \prec p_{sw} \qquad (5)$$

Under the conditions of the in-situ pressure, the deformation due to swelling is taken through dimensional compression conditions within the swelling soil layer, where the condition $\sigma_{z,g} \leq P$ is satisfied.

From the top of the soil layer, we divide the wet soil layer of thickness d_z into elementary slices.

The relative deformation of the swelling soils takes the following form:

$$\varepsilon_{sw} = \frac{\Delta d_z}{d_z} = \varepsilon_{sw}^{\circ}\left(1-\frac{p}{p_{sw}}\right)\left[(\overline{w}_{sw}-w_n)-\chi p\right] \qquad (6)$$

Based on the results of experimental research [3], the relation (6) can be simplified as follows:

$$\varepsilon_{sw} = b_{\circ} - b_1 p + b_2 p^2 \qquad (7)$$

where:

$$b_{\circ} = \varepsilon_{sw}^{\circ}\left(\overline{w}_{sw}-w_n\right)$$

$$b_1 = \left(\frac{\varepsilon_{sw}^{\circ}}{p_{sw}}\right)\left[(\overline{w}_{sw}-w_n)+\chi p_{sw}\right]$$

$$b_2 = \frac{\varepsilon_{sw}^{\circ}}{p_{sw}}\chi$$

Note that the relation (7), which incorporates the coefficients b_0, b_1 and b_2, includes important properties of the swelling soils.

Under the conditions of natural tension, changes to the compressive stresses can be determined using the classic formulas of soil mechanics $\sigma_{z,g} = \gamma_{sw} \times z$. Then, from (4) we will have:

$$\varepsilon_{sw} = b_{\circ} - b_1 \gamma_{sw} z + b_2 \gamma_{sw}^2 z^2 \qquad (8)$$

where: γ_{sw} : is the: unit weight of the swelling soils.

The final value of the absolute swelling strain of the soil under conditions of natural tension is determined using the following expression:

$$S_{sw,g} = \int_{Z_B}^{Z_H} \varepsilon_{sw}(p)dz \qquad (9)$$

where: Z_B et Z_H : Represent the lower and upper limits of the swelling soil, respectively.

Substituting (8) into (9) and integrating, we obtain:

$$S_{sw,g} = b_\circ\left(Z_H - Z_B\right) - \frac{1}{2}b_1\gamma_{sw}\left(Z_H^2 - Z_B^2\right) + \frac{1}{3}b_2\gamma_{sw}^2\left(Z_H^3 - Z_B^3\right) \qquad (10)$$

In the particular case, when the stress due to the self weight of the soil, does not exceed the value of the swelling pressure across the entire thickness of the swelling soil mass and with, $(\sigma_{z,g} < p_{sw})$ along with $\left(0 < Z \le H_{sw}\right)$:

For: $Z_B = 0$; $Z_H = H_{sw}$, expression (10) determines the deformation due to swelling in conditions of natural tension becomes:

$$S_{sw,g} = b_\circ H_{sw} - \frac{1}{2}b_1\gamma_{sw}H_{sw}^2 + \frac{1}{3}b_2\gamma_{sw}^2H_{sw}^3 \qquad (11)$$

where : H_{sw} : Thickness of the layer of swelling soil.

5.1 Computations of the uplift of the foundation of a building or structure, founded on swelling clay soils.

The general case must take into account the action of the three normal stress components. But to simplify the problem, as supported by the standards of literature, swelling deformation is determined in relation to the conditions of uniform compression.

As noted is above, the deformation due to swelling in the foundations of buildings and structures occurs in the area of swelling, where it meets the following condition:

$$\sigma_{z,tot} \le p_{sw}$$

Hence, the equations for determining the formulas, for the uplift of the soil mass, are the transformation of expression (4) into a polynomial.

The compressive stress to the depth of the foundation is taken by Sadjin V.S. [26] as.

$$\sigma_{z,p} = \sigma_\circ e^{-\frac{1}{2}Z\left(\frac{1}{b}+\frac{1}{a}\right)}$$

where $\sigma_o = \sigma_{moy} - \gamma_{sw} D_f$ (12)

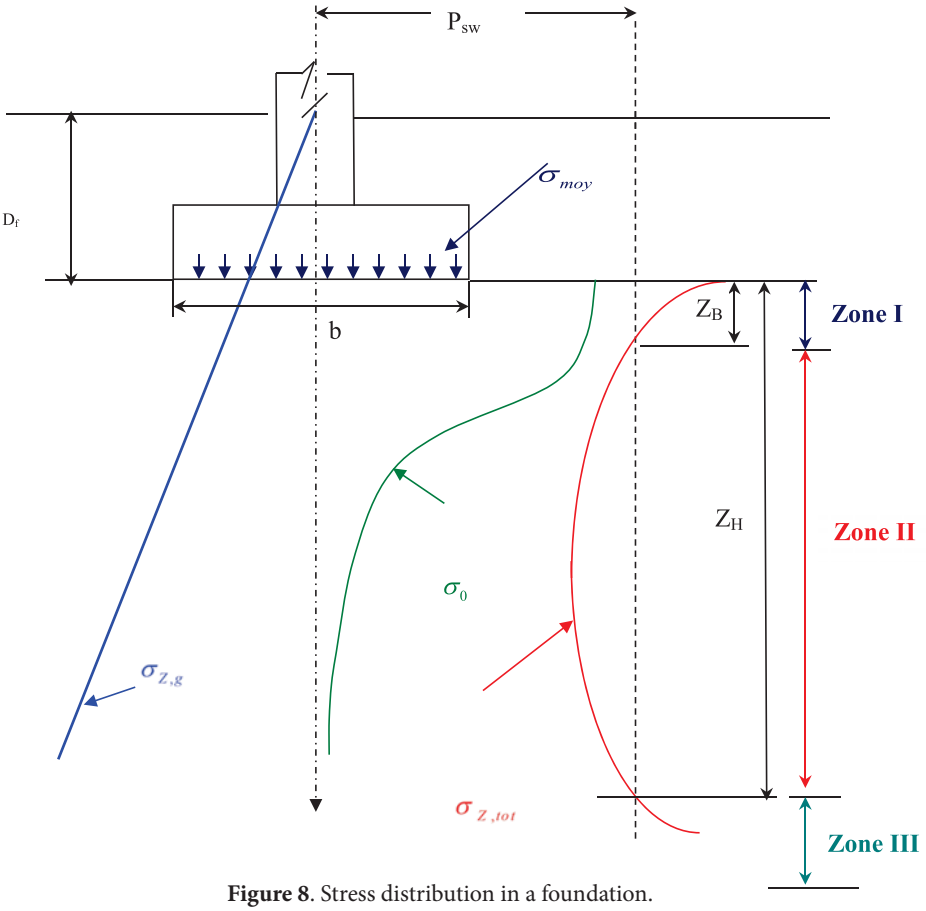

Figure 8. Stress distribution in a foundation.

σ_{moy} : Mean stress at the bottom of the foundation.
D_f : Depth at the bottom of the foundation.
b, a : Dimensions of the bottom of the foundation.

Thus the sum of the pressure within the studied depth of the foundation takes the following form:

$$\sigma_{z,tot} = \rho = \gamma_{sw}\left(Z + D_f\right) + \sigma_{\circ} e^{-\frac{1}{2}Z\left(\frac{1}{b}+\frac{1}{a}\right)} \qquad (13)$$

Taking into account (13), the expression (4) takes the following form:

$$\varepsilon_{sw} = b_{\circ} - b_1(Z + D_f) - b_1\sigma_{\circ} e^{-\frac{1}{2}Z\left(\frac{1}{b}+\frac{1}{a}\right)} + b_2\left[\gamma_{sw}(Z + D_f) + \sigma_{\circ} e^{-\frac{1}{2}Z\left(\frac{1}{b}+\frac{1}{a}\right)}\right]^2 \qquad (14)$$

The final value of the deformation due to the uplift of the foundations of buildings and structures is determined using formula (9).

Substituting (14) into (9), we obtain:

$$S_{sw,p} = \int_{Z_B}^{Z_H}\left\{b_0 - b_1\gamma_{sw}(Z + D_f) - b_1\sigma_{\circ} e^{-\frac{1}{2}Z\left(\frac{1}{b}+\frac{1}{a}\right)} + b_2\left[\gamma_{sw}(Z + D_f) + \sigma_{\circ} e^{-\frac{1}{2}Z\left(\frac{1}{b}+\frac{1}{a}\right)}\right]^2\right\} dz$$

After necessary transformations, we obtain the relation for the uplift of rectangular foundation bearing on the swelling soil:

$$\begin{aligned} S_{sw,p} &= \left(b_{\circ} - b_1\gamma_{sw}D_f + b_2\gamma_{sw}^2 D_f\right)\left(Z_H - Z_B\right) \\ &- \frac{1}{2}\gamma_{sw}\left(b_1 - 2\,b_2\gamma_{sw}D_f\right)\left(Z_H^2 - Z_B^2\right) + \frac{1}{3}\gamma_{sw}^2 b_2\left(Z_H^3 - Z_B^3\right) \\ &+ \frac{2\sigma_{\circ}\left(b_1 - 2\,b_2\gamma_{sw}D_f\right)}{\frac{1}{b}+\frac{1}{a}}\left[e^{-\frac{1}{2}\left(\frac{1}{b}+\frac{1}{a}\right)Z_H} - e^{-\frac{1}{2}\left(\frac{1}{b}+\frac{1}{a}\right)Z_B}\right] \\ &+ \frac{b_2\sigma_{\circ}^2}{\frac{1}{b}+\frac{1}{a}}\left[e^{-\left(\frac{1}{b}+\frac{1}{a}\right)Z_B} - e^{-\left(\frac{1}{b}+\frac{1}{a}\right)Z_H}\right] \\ &+ 4\,b_2\gamma_{sw}\sigma_{\circ}\left\{\left[\frac{Z_B}{\frac{1}{b}+\frac{1}{a}} + \frac{2}{\left(\frac{1}{b}+\frac{1}{a}\right)^2}\right]e^{-\frac{1}{2}\left(\frac{1}{b}+\frac{1}{a}\right)Z_B} - \left[\frac{Z_H}{\frac{1}{b}+\frac{1}{a}} + \frac{2}{\left(\frac{1}{b}+\frac{1}{a}\right)^2}\right]e^{-\frac{1}{2}\left(\frac{1}{b}+\frac{1}{a}\right)Z_H}\right\} \end{aligned} \qquad (15)$$

In the particular case, when all the soil layer is a swelling clay, $\sigma_{z,tot} \le p_{sw}$ and in accordance with Z_B=0 and Z_H=H_{sw}, formula (15) takes the form:

$$\begin{aligned} S_{sw,p} &= \left(b_0 - b_1\gamma_{sw}D_f + b_2\gamma_{sw}^2 D_f^2\right)H_{sw} \\ &- \frac{1}{2}\gamma_{sw}\left(b_1 - 2b_2\gamma_{sw}D_f\right)H_{sw}^2 + \frac{1}{3}b_2\gamma_{sw}^2 H_{sw}^3 \\ &+ \frac{2\sigma_0\left(b_1 - 2\,b_2\gamma_{sw}D_f\right)}{\frac{1}{b}+\frac{1}{a}}\left[e^{-\frac{1}{2}\left(\frac{1}{b}+\frac{1}{a}\right)H_{sw}} - 1\right] \\ &+ \frac{b_2\sigma_0^2}{\frac{1}{b}+\frac{1}{a}}\left[1 - e^{-\left(\frac{1}{b}+\frac{1}{a}\right)H_{sw}}\right] \\ &+ 4\,b_2\gamma_{sw}\sigma_0\left\{\frac{2}{\left(\frac{1}{b}+\frac{1}{a}\right)^2} - \left[\frac{H_{sw}}{\left(\frac{1}{b}+\frac{1}{a}\right)} + \frac{2}{\left(\frac{1}{b}+\frac{1}{a}\right)^2}\right]e^{-\frac{1}{2}\left(\frac{1}{b}+\frac{1}{a}\right)H_{sw}}\right\} \end{aligned} \qquad (16)$$

Case of a square foundation

For a square foundation $a = b$, and in accordance with the formula (15) we have:

$$\begin{aligned} S_{sw,p} &= \left(b_{\circ} - b_1\gamma_{sw}D_f + b_2\gamma_{sw}^2 D_f^2\right)\left(Z_H - Z_B\right) \\ &- \frac{1}{2}\gamma_{sw}\left(b_1 - 2\,b_2\gamma_{sw}D_f\right)\left(Z_H^2 - Z_B^2\right) \\ &+ \frac{1}{3}b_2\gamma_{sw}^2\left(Z_H^3 - Z_B^3\right) + b\sigma_{\circ}\left(b_1 - 2\,b_2\gamma_{sw}D_f\right)\left(e^{-\frac{Z_H}{b}} - e^{-\frac{Z_B}{b}}\right) \\ &+ \frac{1}{2}bb_2\sigma_{\circ}^2\left(e^{-\frac{2Z_B}{b}} - e^{-\frac{2Z_H}{b}}\right) \\ &+ 2\,bb_2\gamma_{sw}\sigma_{\circ}\left[\left(Z_B + b\right)e^{-\frac{Z_B}{b}} - \left(Z_H + b\right)e^{-\frac{Z_H}{b}}\right] \end{aligned} \qquad (17)$$

In the particular case, when the entire thickness of the soil layer is a swelling clay, $\sigma_{z,tot} \le p_{sw}$; and Z_B=0, Z_H=H_{sw}; and formula (17) takes the form:

$$\begin{aligned} S_{sw,p} &= \left(b_{\circ} - b_1\gamma_{sw}D_f + b_2\gamma_{sw}^2 D_f^2\right)H_{sw} \\ &- \frac{1}{2}\gamma_{sw}\left(b_1 - 2\,b_2\gamma_{sw}D_f\right)H_{sw}^2 + \frac{1}{3}b_2\gamma_{sw}^2 H_{sw}^3 \\ &+ b\sigma_{\circ}\left(b_1 - 2\,b_2\gamma_{sw}D_f\right)\left(e^{-\frac{H_{sw}}{b}} - 1\right) + \frac{1}{2}bb_2\sigma_{\circ}^2\left(1 - e^{-\frac{2H_{sw}}{b}}\right) \\ &+ 2\,bb_2\gamma_{sw}\sigma_{\circ}\left[b - \left(H_{sw} + b\right)e^{-\frac{H_{sw}}{b}}\right] \end{aligned} \qquad (18)$$

Case of continuous footing

For a continuous footing $(a \to \infty)$ formula (15) takes the form:

$$S_{sw,p} = \left(b_\circ - b_1\gamma_{sw}D_f + b_2\gamma_{sw}^2 D_f^2\right)\left(Z_H - Z_B\right) - \frac{1}{2}\gamma_{sw}\left(b_1 - 2\,b_2\gamma_{sw}D_f\right)\left(Z_H^2 - Z_B^2\right) + \frac{1}{3}b_2\gamma_{sw}^2\left(Z_H^3 - Z_B^3\right) + 2\,b\sigma_\circ\left(b_1 - 2\,b_2\gamma_{sw}D_f\right)\left(e^{-\frac{Z_H}{2\,b}} - e^{-\frac{Z_B}{2\,b}}\right) + bb_2\sigma_\circ^2\left(e^{-\frac{Z_B}{b}} - e^{-\frac{Z_H}{b}}\right) + 4\,bb_2\gamma_{sw}\sigma_\circ\left[\left(Z_B + 2\,b\right)e^{-\frac{Z_B}{2\,b}} - \left(Z_H + 2b\right)e^{-\frac{Z_H}{2\,b}}\right] \quad (19)$$

In the particular case, when the entire thickness of the soil layer is a swelling clay. $\sigma_{z,tot} \le p_{sw}$; Formula (19) takes the form:

$$S_{sw,p} = \left(b_\circ - b_1\gamma_{sw}D_f + b_2\gamma_{sw}^2 D_f^2\right)H_{sw} - \frac{1}{2}\gamma_{sw}\left(b_1 - 2\,b_2\gamma_{sw}D_f\right)H_{sw}^2 + \frac{1}{3}b_2\gamma_{sw}^2 H_{sw}^3 + 2\,b\sigma_\circ\left(b_1 - 2\,b_2\gamma_{sw}D_f\right)\left(e^{-\frac{H_{sw}}{2\,b}} - 1\right) + bb_2\sigma_\circ^2\left(1 - e^{-\frac{H_{sw}}{b}}\right) + 4\,bb_2\gamma_{sw}\sigma_\circ\left[2\,b - \left(H_{sw} + 2b\right)e^{-\frac{H_{sw}}{2\,b}}\right] \quad (20)$$

Case of a circular foundation

For circular foundations with diameter d, ($b = a = 0.886\,d$), formula (15) takes the form:

$$S_{sw,p} = \left(b_\circ - b_1\gamma_{sw}D_f + b_2\gamma_{sw}^2 D_f^2\right)\left(Z_H - Z_B\right) - \frac{1}{2}\gamma_{sw}\left(b_1 - 2b_2\gamma_{sw}D_f\right)\left(Z_H^2 - Z_B^2\right) + \frac{1}{3}b_2\gamma_{sw}^2\left(Z_H^3 - Z_B^3\right) + 0.886\,d\sigma_\circ\left(b_1 - 2\,b_2\gamma_{sw}D_f\right)\left(e^{-\frac{1.129\,Z_H}{d}} - e^{-\frac{1.129\,Z_B}{d}}\right) + 0.443\,d\sigma_\circ^2\left(e^{-\frac{2.257\,Z_B}{d}} - e^{-\frac{2.257\,Z_H}{d}}\right) + 1.772\,b_2\gamma_{sw}\sigma_\circ\left[\left(Z_B + 0.886\,d\right)e^{-\frac{1.129\,Z_B}{d}} - \left(Z_H + 0.886\,d\right)e^{-\frac{1.129\,Z_H}{d}}\right] \quad (21)$$

In the particular case, when the entire thickness of the soil layer is a swelling clay. $\sigma_{z,tot} \le p_{sw}$; formula (21) takes the form:

$$S_{sw,p} = \left(b_\circ - b_1\gamma_{sw}D_f + b_2\gamma_{sw}^2 D_f^2\right)H_{sw} - \frac{1}{2}\gamma_{sw}\left(b_1 - 2b_2\gamma_{sw}D_f\right)H_{sw}^2 + \frac{1}{3}b_2\gamma_{sw}^2 H_{sw}^3 + 0.886\,d\sigma_\circ\left(b_1 - 2\,b_2\gamma_{sw}D_f\right)\left(e^{-\frac{1.129\,H_{sw}}{d}} - 1\right) + 0.443\,d\,b_2\sigma_\circ^2\left(1 - e^{-\frac{2.257\,H_{sw}}{d}}\right) + 1.772\,d\,b_2\gamma_{sw}\sigma_\circ\left[0.886\,d - \left(H_{sw} + 0.886\,d\right)e^{-\frac{1.129\,H_{sw}}{d}}\right] \quad (22)$$

6 APPLICATION

For a continuous footing

Data:

$\gamma_{sw} = 2.125\ t/m^3$; $D_f = 1\ m$; $b = 1\ m$; $H_{sw} = 12\ m$; $\sigma_\circ = 10\ t/m^2$; $w_n = 14.1\%$; $\varepsilon_{sw}^\circ = 22\%$

Computations of the coefficients: b_0 , b_1 and b_2 :

$$b_\circ = \varepsilon_{sw}^\circ\left(\overline{w}_{sw} - w_n\right) = 0.22\ \left(0.212 - 0.141\right) = 0.01562$$

$$b_1 = \left(\frac{\varepsilon_{sw}^\circ}{p_{sw}}\right)\left[\left(\overline{w}_{sw} - w_n\right) + \chi p_{sw}\right] = \left(\frac{0.22}{2.18}\right)\left[\left(0.212 - 0.141\right) + 0.007 \times 2.18\right] = 8.7.10^{-3}\,cm^2/daN = 8.7.10^{-4}\,m^2/t$$

$$With:\ \chi = \frac{0.212 - 0.198}{2 - 0} = 0.007\,cm^2/daN$$

$$b_2 = \frac{\varepsilon_{sw}^\circ}{p_{sw}}\chi = \frac{0.22}{2.18} \times 0.007 = 7.06.10^{-4}\,cm^4/daN^2 = 7.06.10^{-6}\,m^4/t^2$$

By substituting the values of the coefficients b_0 , b_1 and b_2 into formula (17), we will obtain the uplift deformation of the foundation:

$$S_{sw,p} = (0.01562 - 8.7\cdot10^{-4}\times2.125\times1 + 7.06\cdot10^{-6}\times2.125^2\times1^2)12$$
$$-\frac{1}{2}\times2.125\times(8.7\cdot10^{-4} - 2\times7.06\cdot10^{-6}\times2.125\times1)12^2 + \frac{1}{3}\times7.06\cdot10^{-6}$$
$$\times2.125^2\times12^3 + 2\times1\times10(8.7\cdot10^{-4} - 2\times7.06\cdot10^{-6}\times2.125\times1)$$
$$(e^{-\frac{12}{2\times1}} - 1) + 1\times7.06\cdot10^{-6}\times10^2(1 - e^{-\frac{12}{1}}) + 4\times1\times7.06\cdot10^{-6}$$
$$\times2.125\times10\left[2\times1 - (12 + 2\times1)e^{-\frac{12}{2\times1}}\right] = 0.0404m$$

$$\Rightarrow S_{sw,p} = 0.0404 \text{ m} = 4.04 \text{ cm}$$

If we take b = 2m, the value of the uplifting becomes:

$$\Rightarrow S_{sw,p} = 0.028 \text{ m} = 2.80 \text{ cm}$$

Case of a square foundation

Data:

$\gamma_{sw} = 2.125\ t/m^3$; $D_f = 1\ m$; $b = 1\ m$; $H_{sw} = 12\ m$; $\sigma_\circ = 10\ t/m^2$; $w_n = 14.1\%$; $\varepsilon_{sw}^\circ = 22\%$

Computing the coefficients: b_0, b_1 and b_2:

$$b_\circ = \varepsilon_{sw}^\circ\left(\overline{w}_{sw} - w_n\right) = 0.22\ (0.212 - 0.141) = 0.01562$$

$$b_1 = \left(\frac{\varepsilon_{sw}^\circ}{p_{sw}}\right)\left[(\overline{w}_{sw} - w_n) + \chi p_{sw}\right]$$
$$= \left(\frac{0.22}{2.18}\right)\left[(0.212 - 0.141) + 0.007\times2.18\right]$$
$$= 8.7.10^{-3}\ cm^2/daN = 8.7.10^{-4}\ m^2/t$$

$$With:\ \chi = \frac{0.212 - 0.198}{2 - 0} = 0.007\ cm^2/daN$$

$$b_2 = \frac{\varepsilon_{sw}^\circ}{p_{sw}}\chi = \frac{0.22}{2.18}\times0.007 = 7.06.10^{-4}\ cm^4/daN^2$$
$$= 7.06.10^{-6}\ m^4/t^2$$

By substituting the values of the coefficients b_0, b_1 and b_2 into formula (5) we will evaluate the uplift deformation of the foundation.

$$S_{sw,p} = (0.01562 - 8.7\cdot10^{-4}\times2.125\times1 + 7.06\cdot10^{-6}\times2.125^2\times1^2)12$$
$$-\frac{1}{2}\times2.125\times(8.7\cdot10^{-4} - 2\times7.06\cdot10^{-6}\times2.125\times1)12^2 + \frac{1}{3}\times7.06\cdot10^{-6}$$
$$\times2.125^2\times12^3 + 1\times10(8.7\cdot10^{-4} - 2\times7.06\cdot10^{-6}\times2.125\times1)$$
$$(e^{-\frac{12}{1}} - 1) + \frac{1}{2}\times1\times7.06\cdot10^{-6}\times10^2(1 - e^{-\frac{2\times12}{1}}) + 2\times1\times7.06\cdot10^{-6}$$
$$\times2.125\times10\left[1 - (12 + 1)e^{-\frac{12}{1}}\right] = 0.0477m$$

$$\Rightarrow S_{sw,p} = 0.0477 \text{ m} = 4.77 \text{ cm}$$

7 CONCLUSIONS

Based on an analysis of the experimental results presented here, the following conclusions are can drawn. A theoretical model was formulated to describe the swelling potential of clay soils on the basis of their features obtained from oedometer tests. For expansive soils, designers are only interested in the measurable quantities which are generally the pressure and the amplitude of the expansion. A model has been proposed for the expansion potential of the studied clays. On the basis of the non linearity of the physical mechanism of distortion, the method developed in the present work, relates the phenomenon of expansion with the distribution of the contact pressure, the soil properties, as well as the type and the value of the external loading and allows the design of lifting shallow foundations on expansive soils,

On the basis of the nonlinearity of the deformation mechanism of swelling clays, the method developed in the present work permits a calculation of the lifting surface of different types of foundations on expansive soils.

The rise of the foundations, based on expansive soils, depends not only on the expansiveness of the clay soils but also on the magnitude of the external loads transmitted to the ground by the buildings.

The obtained results open up new perspectives for methods to design foundations on expansive clay soils.

REFERENCES

[1] ASTM. 2006. Standard practice for classification of soils for engineering purposes (Unified Soil Classification System). ASTM standard D2487-06. Annual Book of ASTM Standards, Vol. 04.18. American Society for Testing and Materials, West Conshohocken, pp. 395–408.

[2] Baheddi, M., Djafarof, M.D.,Charif, A. 2007. Design method of flexible continuous footings on swelling clay soils. Building Research Journal, Institute of construction and Architecture Slovak Academy of Sciences, 55, 3, 169-184.

[3] Baheddi, M., Mustafaev, A.A., Djafarof, M.D. 1990. Mechanism of clays swelling deformation under the effect of centrifugal forces and the design shallow foundations. Thesis Ph D. Moscow (in Russian).

[4] Bekkouch, A., Aissa Mamoune, S.M., Houmadi, Y. 2003. Variabilité des paramètres de gonflement

sous une fondation superficielle; Symposium international sur les fondations superficielles FONDSUP; (05 – 07 Novembre) Paris, France, pp. 113-122.

[5] Bekkouch, A., Djedid, A., Aissa Mamoune, S.M. 2002. identification et prévision du gonflement des marnes de Tlemcen (Algérie). PARAM, Laboratoire Centrale des Ponts et Chassées de l'école Nationale des Ponts et Chaussées, pp. 125-132.

[6] Bigot, G., Zerhouni, M.I. 2000. Retrait, gonflement et tassement des sols fins Bulletin des laboratoires des Ponts et Chaussées, 229, 105-114.

[7] Chen, F.H. 1988. Foundations on expansive soils. Developments in Geotechnical Engineering, Elsevier Publishing Co., 54, 465 p.

[8] Cokca, E. 2000. Comparison of suction and oedometer methods for the measurement of swelling pressure. Engineering Geology 33, 2, 141-147.

[9] Cuisinier, O., Masrouri, F. 2005. Hydromechanical-behaviour of a compacted swelling soil over a wide suction range. Engineering Geology 81, 3, 204-212.

[10] Delage, P., Howat, M.D., Cui, Y.J. 1998. The relationship between suction and swelling properties in a heavily compacted unsaturated clay. Engineering Geology 50, 1–2, 31-48.

[11] Derriche, Z., Iguechtal, L., Tas, M. 1999. Comportement des ouvrages dans liest argiles expansives d'In-Aménas. Revue Française de Géotechnique, 89, 55-65.

[12] Djedid, A., Bekkouche, A., Aissa Mamoune, S.M. 2001. Identification et prévision du gonflement de quelques sols de la région de Tlemcen (Algérie). Bulletin de liaison des Laboratoires des Ponts et Chaussées 233, 67-75.

[13] Ejjaouani, H., Magnan, J.P., Shakhirev, V. 2000. Calcul des fondations sur sols gonflants, Revue Marocaine de génie civil, 89, 19P.

[14] Erzin, Y., Erol, O. 2007. Swell pressure prediction by suction methods. Engineering Geology 92, 3–4, 133-145.

[15] Fleurau, J.M., Verbrugge, J.C., Huergo, P.J., Correia, A.G., Kheirbek-Saoud, S. 2002. Aspects of the behavior of compacted clayey soils on drying and wetting paths. Canadian Geotechnical Journal 39, 1341-1357.

[16] Johnson, L.D. 1978. Predicting potential heave and heave with time in swelling foundation soils. US Army Engineer Waterways Experiment Station, CE, Vicksburg, Miss. Technical report S-78-7.

[17] Kariuki, P.C., van der Meer, F. 2004. A unified swelling potential index for expansive soils. Engineering Geology 72, 1–2, 1-8.

[18] Komine, H., Ogata, N. 2004. Predicting swelling characteristics of bentonites. Journal of Geotechnical and Geoenvironmental Engineering 130, 8, 818-829.

[19] Lancelot, L.,Shahrour, I., Khaddaj, S. 2002. Etude en laboratoire du gonflement de l'argile des Flandres, PARAM. Laboratoire Centrale des Ponts et Chassées de l'école Nationale des Ponts et Chaussées, 145-151.

[20] Marcial, D., Delage, P., Cul, Y.J. 2001. Compressibility of two swelling clays under high pressure. In Adachi &Fukue (eds), Clay Science for engineering. Rotterdam: Balkerna. ISBN:90-5809-175-9, pp. 571-576.

[21] Miao, L., Houston, S.L., Cui, Y., Yuan, J. 2007. Relationship between soil structure mechanical behavior for an expansive unsaturated clay. Canadian Geotechnical Journal 44, 2, 126-137.

[22] Mouroux, P., Margon, P., Pinte, J.C. 1988. La construction économique sur les sols gonflants, BRGM, Manuels et méthodes, 14, 125 p.

[23] Mustafaev, A.A. 1989. Foundations on collapsible and swelling soils (In Russian) Vysshayashkola, Moscow, 592 p.

[24] Nelson, J.D., Chao, K.C., Overton, D.D. 2007. Definition of Expansion Potential for Expansive Soil. Proceedings of the 3rd Asian Conference on Unsaturated Soils, Nanjing, China. April.

[25] Rao, B.H.,Venkataramana, K., Singh, D.N. 2011. Studies on Determination of Swelling properties of soils from suction measurements, CanadianGeotechnical Journal 48, 3, 375-387.

[26] Sadjin, V.S. 1971. About the model of swilling soils. Foundations and underground structures on swelling soils 61. Strojizdat, Moscow (in Russian).

[27] Sorochan, E.A. 1989. Construction of works on the inflating soils. Strojizdat, Moscow, 312 p. (in Russian).

[28] Thakur, V.K.S., Singh, D.N. 2005. Rapid determination of swelling pressure of clay minerals. ASTM Journal of Testing and Evaluation 33, 4, 239-245.

[29] Thomas, P.J., Baker, J.C., Zelazny, L.W. 2000. An expansive soil index for predicting shrink–swell potential. Soil Science Society of America Journal 64, 1, 268-274.

[30] Yilmaz, I. 2006. Indirect estimation of the swelling percent and a new classification of soils depending on liquid limit and caution exchange capacity. Engineering Geology 85, 34, 295-301.

[31] Zerhouni, M.I., Dhouib, A., Hubert, B. 2002. Paramètres de gonflement et retrait des argiles – essais normalisées en France PARAM, Laboratoire Centrale des Ponts et Chassées de l'école Nationale des Ponts et Chaussées, pp. 125-132.

UPORABA PERTHOVEGA PENETROMETRA ZA PESKE (PSP) ZA DOLOČITEV INŽENIRSKIH PARAMETROV PESKOV

S.D. Mohammadi
Bu-Ali Sina University,
Faculty of Sciences, Department of Geology
Mahdieh Ave., 65175-38695 Hamedan, Iran
E-pošta: d.mohammadi@basu.ac.ir

Ključne besede

dinamični točkovni indeks odpora q_d, inženirski parametri, ponovljivost, statistične metode

Izvleček

Določanje in-situ inženirskih parametrov peščenih zemljin je bil vedno izziv za geotehnične inženirje, zaradi česar je bilo do sedaj razvitih več metod. Preizkus s Perthovim penetrometrom za peske (PSP) je ena od najbolj vsestranskih metod. Je bistveno hitrejše in cenejše orodje kot vrtalna oprema, še posebej, če je globina raziskovanja zmerna. V prikazani raziskavi je obravnavana metodologija za uporabo naprave PSP za ovrednotenje inženirskih parametrov peščenih zemljin v laboratorijskih pogojih in preučevana ponovljivosti rezultatov preizkusa. Najprej so bili izvedeni preizkusi na tipičnih teheranskih mladih naplavinah (slabo granulirana peščena zemljina, SP), na vzorcih petih različnih gostot, navlaženih s pršenjem ali zalivanjem. Dalje so bile proučene običajne in logNormal porazdelitve podatkov o preizkusih z uporabo Kolmogorov-Smirnov testa normalnosti porazdelitve. Nato pa so bile, na podlagi dobljenih rezultatov, določene vrste razmerij med dinamičnim točkovnim indeksom odpora q_d in drugimi parametri, kot so relativna gostota (Dr), modul elastičnosti (E), strižni modul (G) in trenjski kot zemlljine. Rezultati kažejo, da so dobljeni odnosi pol-logaritmični in logaritmični, večina dobljenih eksperimentalnih enačb ima visok koeficient določanja (>90%). Za oceno natančnosti rezultatov je bil uporabljen interval zaupanja meritev pri 95% zanesljivosti. Rezultati kažejo, da so bili vsi dobljeni eksperimentalni odnosi ustrezni. Nazadnje je bila ponovljivost rezultatov testov ocenjena z izračunom koeficienta variacije, ki je bil za vse teste manjši od 30%.

USE OF A PERTH SAND PENETROMETER (PSP) DEVICE TO DETERMINE THE ENGINEERING PARAMETERS OF SANDS

S.D. Mohammadi
Bu-Ali Sina University,
Faculty of Sciences, Department of Geology
Mahdieh Ave., 65175-38695 Hamedan, Iran
E-mail: d.mohammadi@basu.ac.ir

Keywords

dynamic-point resistance index (q_d), engineering parameters, repeatability, statistical methods

Abstract

Determining the in-situ engineering parameters of sandy soils has always been a challenge for geotechnical engineers, resulting in several methods having been developed so far. The Perth Sand Penetrometer (PSP) test is one of the most versatile of these methods. It is a considerably faster and cheaper tool than boring equipment, especially when the depth of the exploration is moderate. In the present research, a methodology for the use of a PSP device to evaluate the engineering parameters of sandy soils in laboratory conditions is discussed and the repeatability of the test results is studied. First of all, the tests were performed on typical Tehran young alluvial deposits (poorly graded sandy soil, SP) consistently prepared to 5 densities using the sand raining or pluviation technique. Next, the normal and logNormal distributions of the test data using the Kolmogorov-Smirnov normality test were examined. After that, based on the obtained results, the relationship types between the dynamic point resistance index (q_d) and other parameters, such as the relative density (Dr), the modulus of elasticity (E), the shear modulus (G) and the friction angle of the soil, were determined. The results show that the obtained relationships were semi-logarithmic and logarithmic, and most of the obtained experimental formulas had a high coefficient of determination (>90%). To evaluate the accuracy of the results, 95% confidence and prediction bands were also used and the results show that all the obtained experimental relationships were appropriate. Finally, the repeatability of the test results was evaluated by calculating the coefficient of variations, which was less than 30% for all the tests.

1 INTRODUCTION

The engineering parameters of sandy soil at an earthwork, such as a foundation design on sandy soils, are commonly assessed using penetrometer testing. The most commonly employed dynamic method is the Standard Penetrometer Test (SPT), which involves the driving of a split-spoon sampler using a 63.5 kg drop weight [1]. While such devices are useful tools for larger-scale site investigations, their applicability for large-scale projects is limited by the scale of the apparatus and its relative insensitivity for shallow depths. Dynamic probing is a continuous soil investigation technique and is assumed to be one of the simplest soil penetration tests. It basically consists of repeatedly driving a metaltipped probe into the ground using a drop weight with a fixed mass and travel. Testing is carried out continuously from ground level to the final penetration depth. The continuous sounding profiles enable the easy recognition of

Table 1. Some of the dynamic probing devices and their specifications.

Penetrometer specifications	Mackintosh	Dynamic Cone Penetrometer (DCP)	Perth Sand Penetrometer (PSP)	Dynamic Probing Light (DPL)	Dynamic Probing Medium (DPM)	Dynamic Probing High (DPH)	Dynamic Probing Super High (DPSH)
Hammer weight (kg)	4.5	8	9	10	30	50	63.5
Fall height (m)	0.3	0.575	0.6	0.5	0.5	0.5	0.75
Cone diameter (mm)	27.94	20	-	35.7	35.7	43.7	50.5
Area at the base of cone (cm^2)	6.13	3.15	-	10	10	15	20
Diameter of rod (mm)	12.7	16	16	22	32	32	32
Tip angle (deg)	30	60	-	60	60	60	60
Standard range for number of blows	3-50 (for 10cm of penetration)	<20 (for 5cm of penetration)	<20 (for 5cm of penetration)	3-50 (for 10cm of penetration)	3-50 (for 10cm of penetration)	3-50 (for 10cm of penetration)	5-100 (for 20cm of penetration)
References	[5]	[7]	[2]	[2]	[11]	[11]	[11]

dissimilar layers and even thin strata using the observed variation in the penetration resistance.

There are many dynamic probe devices in the world, such as Dynamic Cone Penetrometer (DCP), Mackintosh probe, Dynamic Probing Light (DPL), Dynamic Probing Medium (DPM), Dynamic Probing High (DPH), Dynamic Probing Super High (DPSH), Perth Sand Penetrometer (PSP), etc. Table 1 shows some of the dynamic probing devices and their specifications.

The Perth Sand Penetrometer (PSP) is a lightweight dynamic penetrometer, a tool that is considerably faster and cheaper than boring, particularly when the depth of exploration is low and the soils being investigated are not coarse gravel [2, 3].

Most of the larger cities in parts of the world such as in Southern Australia, Northern Iran and Central UAE are situated on the coast or desert and many have extensive coastal deposits of clean, aeolian and alluvial sands. In earthwork projects like the construction of roads, dwellings and lightweight commercial and industrial structures, a determination of the engineering parameters of sandy deposits is important.

The Perth Sand Penetrometer is described in detail in Australian Standard AS1289.F3.2 [4]. Since then, it has been used for the site characterization of pavement layers and foundations in other countries such as Iran [2]. There are some correlations between the dynamic probing devices (except PSP) and the engineering parameters of different soils [e.g. 5, 6, 7, 8], thus the main objectives of this paper are to describe the capability of the PSP to study the engineering parameters of sandy soils.

2. THE PERTH SAND PENETROMETER (PSP)

The Perth Sand Penetrometer is described in detail in Australian Standard AS1289.F3.3 [4]. The physical arrangement of the PSP is summarized in this part, and illustrated in Fig. 1. It consists of a 9kg sliding weight that delivers a measured quantity of energy by falling through a height of 600mm onto an anvil block. This energy is used to push a 16mm blunt ended steel rod into the ground. The steel rod is usually scribed at increments of 50mm and the results are expressed as the number of blows required to drive the rod through a distance of 150mm. The total mass of the device is less than 20 kg, making it relatively portable. Mohammadi et al. [9] explained that the results of dynamic penetrometer tests with a flat tip (e.g., the PSP) are more repeatable and accurate compared to other penetrometers such as the DCP. Thus, it is better to use the PSP device instead of other dynamic penetrometers. Raising and releasing of the weight is achieved by hand, with a certain amount of care required to ensure that

- The weight is lifted through the full 600mm height,
- There is negligible impact on the upper stop at the top of the lift, and
- The weight is released cleanly and allowed to fall without interference.

The sounding rods are configured so that once driven, the hammer can be removed and additional rods added to enable the testing to continue to depths of several meters. In the author's experience, the maximum practical depths are of the order of 5 or 6 m in exceptionally loose conditions. Beyond these depths, difficulties in the

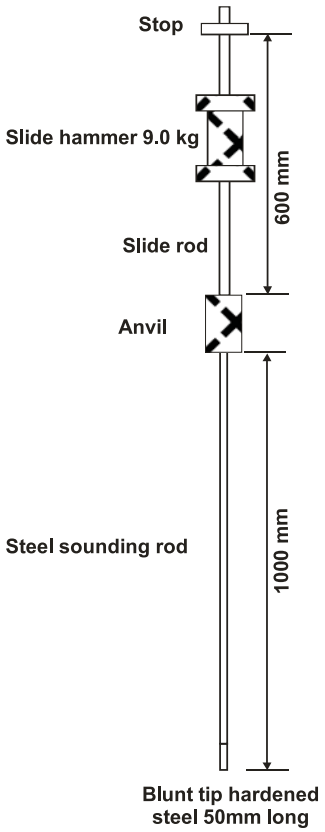

Figure 1. Perth Sand Penetrometer [4].

retrieval of the rods and the risk of lost rods through damage become too great.

The main advantages of the PSP include:

(1) Speed of operation;
(2) Use in difficult terrain where access is poor;
(3) The requirement for minimal equipment and personnel;
(4) Low cost of the equipment;
(5) Simplicity of operation and data recording/analysis;
(6) Use in the interpolation of soil strata and properties between trial pits and boreholes;
(7) Reduction in the number of boreholes required.

3 PROBABILISTIC AND STATISTICAL METHODS

The application of probabilistic and statistical methods in geotechnical engineering has increased remarkably in recent years. In this paper, some probabilistic and statistical methods were used to evaluate the laboratory test results obtained from laboratory tests on studied river sandy soil. One of the methods used is the assessment of the distribution properties of the data. The Normal probability density function (pdf) is an appropriate model to assess the data distribution. The function of the Normal distribution is [10]:

$$f_x(x\left|\mu,\sigma\right.)=\frac{1}{\sigma\sqrt{2\pi}}\exp\left\{-\frac{1}{2}(\frac{x-\mu}{\sigma})^2\right\} \qquad (1)$$

in which μ is the mean and σ^2 the variance. The pdf is symmetrical about a mode at μ, and falls off quickly as x deviates from the mean. The Normal pdf is usually tabulated or calculated numerically using its Standard Normal form, with a mean of zero and a variance of one, N (0,1).

Sometimes probability distributions are chosen simply because they appear to fit the observed data. This rationale has nothing to do with physical law. This is often the case in fitting probability distributions to, say, soil data. One observes that when the frequencies of undrained strength measurements are plotted against the strength value they might exhibit a bell-shaped form characteristic of the Normal pdf, and thus a Normal distribution model is used to approximate them [10].

Various statistical methods can be used to test whether the match between the empirical data frequencies and the theoretical pdf model is close enough to assume that the differences between the observed and the modelled could simply be due to sampling variability [10]. The most common of these tests are the Chi-square goodness of fit and the Kolmogorov-Smirnov maximum deviation test. In many cases, however, the easiest way to assess the quality of the fit of a theoretical distribution to an observed distribution is to plot the observed distribution against the theoretical distribution.

A probability grid is a specialized graph paper with horizontal and vertical scales designed such that the cumulative frequencies of a particular form of pdf (e.g., a Normal distribution) plot as straight lines. Thus, empirical data can be plotted on a probability grid and a visual determination made as to whether they are well approximated. The effect of the Normal probability grid can be achieved by using cumulative frequencies as arguments to an inverse standard Normal cumulative distribution function.

Another graphical tool for comparing data with analytical distributions is the quantile-quantile (Q-Q) graph. A Q-Q graph shows the observed quantile of the data plotted against the theoretical quantile of the best fitting distribution. If the frequency distribution of the sample data is reasonably approximated, the empirical and analytical quantile should be approximately the same, and the data pairs should lie on a 45-degree line [11].

An assessment of the regression line confidence can be checked using confidence and prediction bands. To

achieve that, 99% and 95% confidence bands are useful in geotechnical engineering.

Finally, the correlation coefficient R^2 between two types of data, such as soil parameters, is determined by [10]:

$$R^2 = \left(\frac{\sum(x-\overline{x})(y-\overline{y})}{\sqrt{\left[\sum(x-\overline{x})^2\sum(y-\overline{y})^2\right]}}\right)^2 \qquad (2)$$

Where:

x: the value of the obtained data
y: the value of the measured data

4 MATERIALS AND METHODS

In order to achieve the main objectives of this paper it was necessary to select a suitable sample. First of all, the appropriate sampling area was selected and the sampling was done. Then, the selected sample was prepared in the laboratory.

4.1 Sampling area

The materials used in this research included typical Tehran young alluvial deposits (a poorly graded sandy soil) taken from the west of Tehran. Geologically, the Tehran young deposits comprise subrounded sand grains with 5% gravel. The X-ray analysis results show that it is comprised of quartz, feldspar, pyroxene and calcite.

4.2 Sample preparation

The data used in this paper was obtained from laboratory tests undertaken by the author at the Geotechnical Engineering Laboratory of Bu-Ali Sina University, Hamedan, Iran.

To prepare the soil sample for testing, alluvial deposits were oven dried and passed through sieve No. 4. Fig. 2 shows the gradation curves of the original soil and the sample after passing sieve No. 4, which is classified as poorly graded sand (SP) according to the Unified Soil Classification System. The index properties of the soil are shown in Table 2.

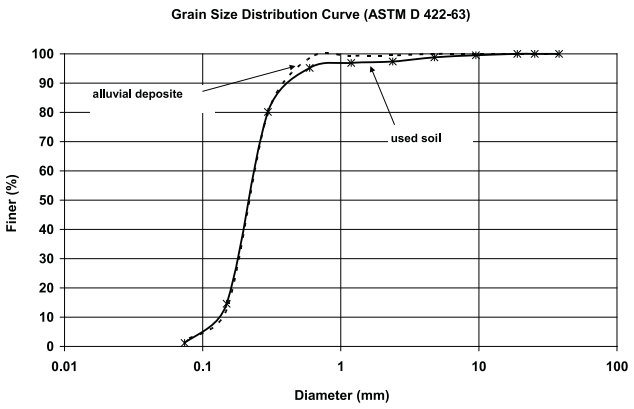

Figure 2. Gradation curves of alluvial deposit and used soil.

Table 2. The index properties of used soil.

Parameter	value
e_{max} (-)	0.97
e_{min} (-)	0.46
Gs (-)	2.66
γ_d *(max)* (KN/m^3)	17.85
γ_d *(min)* (KN/m^3)	13.24
Cu (-)	1.16
Cc (-)	1
value of clay (%)	0
value of silt (%)	2
USCS soil classification	SP

To achieve a uniform sample, the sample in the testing mould was remoulded using a sand pluviation set that was designed and constructed at Bu-Ali Sina University. It has a height and diameter, both of 1m. The experimental arrangement used to generate a suitable sample for this study is schematically shown in Fig. 3. The sand was rained from the hopper, through holes ranging in size from 6mm to 15mm diameter, at a spacing (S) ranging from 20 to 100mm, with the holes arranged in a triangular pattern.

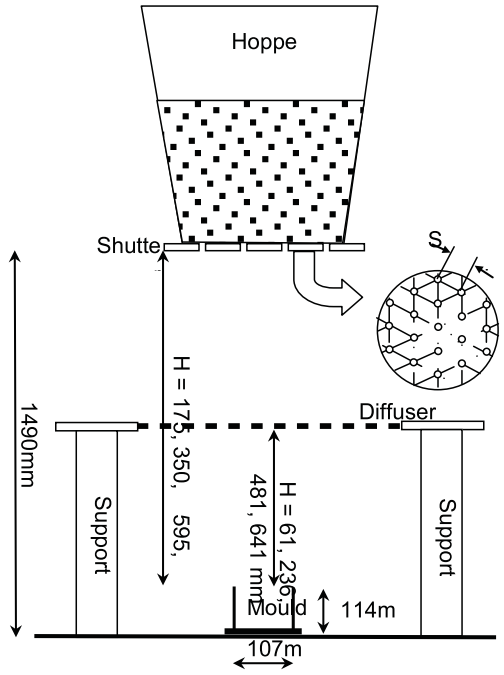

Figure 3. Experimental arrangement used in this study.

Table 3. The index properties of used soil.

Dr(%)*	Mean of Water content (%)	Dry unit weight (gr/cm^3)
25	0.04	1.44
35	0.04	1.48
50	0.04	1.55
60	0.04	1.60
75	0.04	1.67

* Relative density

In all cases, a single diffuser screen with an aperture size of 2.36mm was employed (except where the pluviation rate was so great that sand accumulated on the screen, at which point, the diffuser was removed). The fall heights (free fall distance travelled by the sand from the diffuser to the top of mould) considered were 61mm, 236mm, 481mm, and 641mm. A 1 liter mould (107mm in diameter and 114mm in height) was used to catch the sand for the density control. Details of the tests on samples having different densities are indicated in Table 3.

To prepare the soil sample for the direct shear test, a circular shear box with 60 mm diameter and 25 mm height was used. To achieve a uniform compaction in the circular shear mould of the direct shear machine, tamping by a small circular steel plate with a 60 mm diameter was used. All the direct shear tests were also carried out in dry conditions.

4.3 Testing procedures

Several tests including the Perth Sand Pentrometer (PSP) test, the Plate Load (PLT) and direct shear tests were undertaken on the compacted materials as described in the following sections.

4.3.1 The Perth Sand Pentrometer tests and its repeatability

As previously mentioned, the PSP tests were used to determine the engineering parameters of sandy soil in laboratory conditions. To achieve some relation between the PSP results and the engineering parameters of sandy soils, several tests according to the ASTM standard were undertaken. Table 4 shows the program of laboratory tests.

The result of the PSP tests is shown by the q_d index, where q_d is the dynamic point resistance (Pa), which is determined using [12]:

$$q_d = \frac{W}{W + W'} \cdot r_d \qquad (3)$$

Where:

q_d is the unit point resistance value (Pa)
W is the mass of the hammer (kg)
h is the height (m)

Table 4. Testing program for laboratory investigations.

Dr (%) of sand samples	PSP (number of tests)	PLT* (number of tests)	Direct shear (number of tests)
25	3	3	7
35	3	3	7
50	3	3	7
60	3	3	7
75	3	3	7
Total -	15	15	35

* Plate Load Test

g is the acceleration due to gravity (m/sec2)
A is the area at the base of the cone (m2)
e is the average penetration per blow
W' is the total mass of the extension rods, the anvil and the guiding rods (kg)

Fig. 4 shows the q_d index values obtained from the laboratory PSP tests that were undertaken on sandy soil at the testing mould.

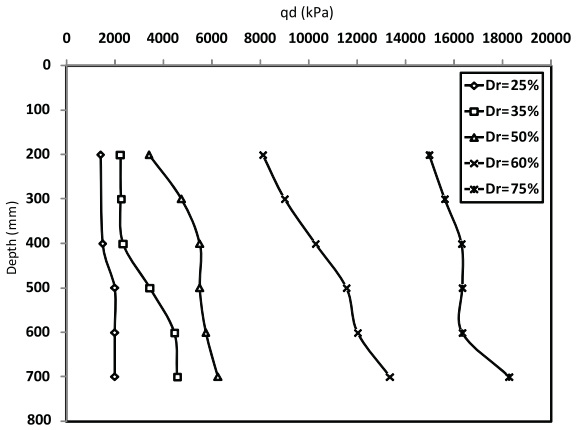

Figure 4. Average of q_d index versus depth for studied soil at the testing mould.

The repeatability of the PSP test results is an important consideration. To evaluate the repeatability, several tests were carried out. Each testing series included three PSP tests on studied soil with different relative densities (Loose, Medium and Dense). In order to study the repeatability of the results, it was important to choose a suitable parameter that represented the repeatability. The use of the standard deviation value, *s*, was not appropriate for this purpose because it is large for large values of NPSP [5]. However, the coefficient of variation (*COV*) can be considered as an indicative parameter because it represents a Normalized standard deviation. The *COV* parameter is calculated using Eq. (4):

$$COV = s / \overline{X} \qquad (4)$$

Where:

$\overline{X}$: the average of NPSP at each depth
s : the standard deviation of NPSP at each depth

Table 5 shows the coefficient of variation (*COV*) for the results obtained from some of the dynamic probe devices reported by various researchers.

Table 5. Coefficient of variation for results obtained from some dynamic probe devices.

Dynamic probe devices	Range of *COV* (%)	Mean of *COV* (%)	References
Standard penetration test (SPT)	27–85	30	[12]
Dynamic Cone Penetrometer (DCP)	3-58	17	[7]
Mackintosh probe	0-39	11	[5]
Dynamic Probing Light (DPL)	0-23	8	[11]
Dynamic Probing Medium (DPM)	0-17	5	[11]
Dynamic Probing High (DPH)	0-55	16	[11]
Dynamic Probing Super High (DPSH)	0-44	13	[11]

The sources of variability in soil properties differ, and accordingly the coefficients of variation differ for different dynamic devices [5]. It can be seen that the variation of the *COV* for the results of the Standard Penetration Test (N), which is basically a super heavy dynamic probe test, is higher than the other dynamic devices that are reported to be between 27% and 85% with a mean value of 30% [13]. The repeatability of the SPT test results could be used as a measure of the repeatability of the PSP results by comparing the *COV* values of the two methods. In the present research, the values of the *COV* have been determined for each depth in each series of tests.

The average value of the *COV* was about 5.60% and its standard deviation was 9.51. In more than 68.7% of the tests, the value of the *COV* was 0%, and in 12.5% of the tests, this value was 20.28%. In the tests undertaken, the values of the *COV* varied between 0 and 28.3%, and for all cases it was less than 30%. Therefore, the results of the PSP tests for the three relative densities (Loose, Medium and Dense) can be considered as repeatable when compared with the values presented in Table 5.

4.3.2 Plate Load Test (PLT)

The Plate Load Test (PLT) is a useful site investigation tool and has been used for the proof testing of pavement layers in a lot of European countries for many years. Currently, it is used for the evaluation of both rigid and flexible pavements [14]. The PLT, at full or reduced scale, is sometimes considered as the best means of determining the deformation characteristics of soils, but it is only used in exceptional cases because of the costs involved [15]. In the present research, a round plate of 230mm diameter was used. The PLT was used as a reference test to obtain the strength parameters of the soil under investigation. A loading frame was designed to fit the mould and its support. To perform the test, the bearing plate and hydraulic jack were carefully placed at the centre of the samples under the loading frame (Fig. 5). The hydraulic jack and the supporting frame were able to apply 60 tons load. For the measurement of deformations, dial gauges that are capable of recording a maximum deformation of 25.4 mm (1 in.) with an accuracy of 0.001 in. were employed. The ASTM-D1195 [16] standard method was followed to perform the test.

The elastic modulus is always considered as a more important deformeability parameter for a geomaterial. As in the case for other stress-strain tests, different elastic moduli can be obtained from the PLT. The soil elastic moduli can be defined as: (1) the initial tangent modulus; (2) the tangent modulus at a given stress level; (3) reloading and unloading modulus and; (4) the secant modulus at a given stress level [14]. In this study, since the stress--strain curves had a clear peak point, the initial tangent modulus was determined for all the plate load tests. To determine the initial modulus ($E_{PLT(i)}$), a line was drawn at a tangent to the initial segment of the stress-strain curve, then an arbitrary point was chosen on the line and the stress and deflection corresponding to this point

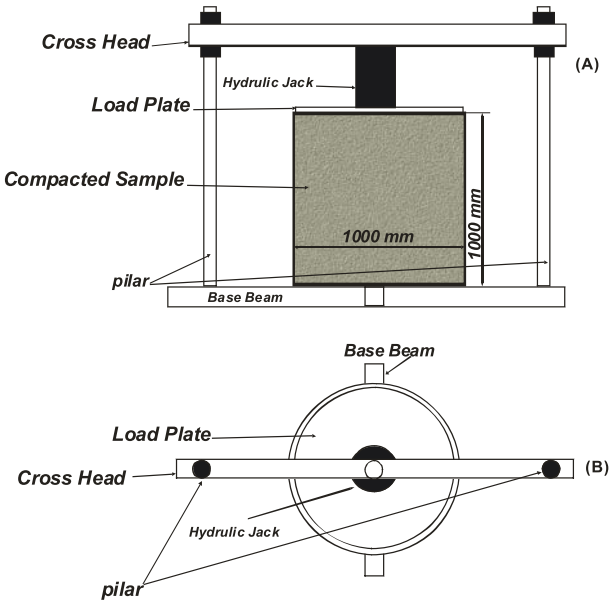

Figure 5. A schematic diagram of the Plate Load Test (PLT) set up (A) side view (B) plan view.

were determined for a calculation of the initial modulus. Fig. 6 describes the deformations and stresses used for determining $E_{PLT(i)}$. A reloading stiffness modulus called $E_{PLT(R2)}$ was also determined for each stress-strain curve.

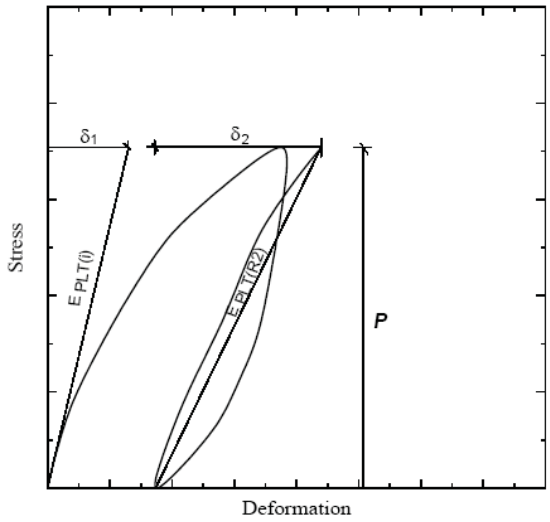

Figure 6. Definition of the modulus from PLT results [13].

The second parameter that can be calculated from the PLT results is the shear modulus (G). The shear modulus is defined as the ratio of the shear stress to the shear strain [15] and is calculated using Eq. (5) [17]:

$$G_{PLT} = \frac{qD}{\rho}\frac{\pi}{8}(1-\nu) \qquad (5)$$

where:

q : bearing pressure
D : diameter of the loading plate
ρ : settlement
ν : Poisson's ratio

4.3.3 Direct shear test

In order to determine the soil friction angle, 35 direct shear tests (Table 4) were undertaken in a circular shear mould with a diameter of 60mm. Due to the nature of the soil samples (non-cohesive), the cohesion parameter (C) was equal to zero and thus, the friction angles were calculated. The ASTM-D 3080-98 [18] standard method was followed to perform the test.

5 RESULTS AND DISCUSSIONS

As mentioned previously, one of objectives of the present research was to obtain the correlations between the q_d index and some engineering parameters of sandy soils. In the following sections, the results of the tests and their correlations with important engineering parameters of the studied soil are discussed.

5.1 q_d index of studied soil

To determine the q_d index, Eq. (3) was used. The values of q_d were changed between 1400 kPa and 18270 kPa for the studied sandy soil. Fig. 7a shows the distribution of Plate Load Test on a logNormal chart. Also, the Kolmogorov-Smirnov Normality test is shown (fig. 7b). The q_d index falls nearly along a line in this plot and the P-Value is more than 0.05, from which one would infer that they are well modelled as a logNormal distribution.

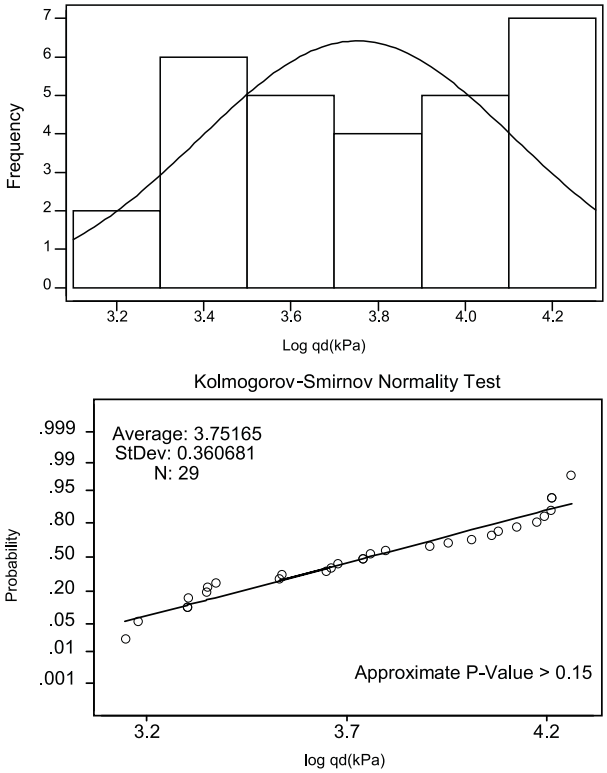

Figure 7. LogNormal distribution of the q_d index shown by (a) histogram of data and (b) the Kolmogorov-Smirnov Normal test.

5.2 q_d versus Dr(%)

The relative density (Dr) is a useful parameter to describe the consistency of sands [19]. To obtain the correlation between the average q_d and Dr, first of all, a statistical distribution of Dr values was investigated. Figs. 8a and 8b show the Normal histogram curve and the Normal probability plot of a Kolmogorov-Smirnov test for relative density, respectively. As shown, the distribution of the Dr values of the studied soil is Normal.

After that, the correlation between the average q_d and Dr was investigated. Because the distribution of Dr is Normal and the distribution of q_d is logNormal, thus the equation for Dr-q_d will be Semi-Logarithmic. Eq. (6) and fig. 9 suggest a good correlation between these two parameters. The determination coefficient (R^2) of Eq. (6) is 0.98.

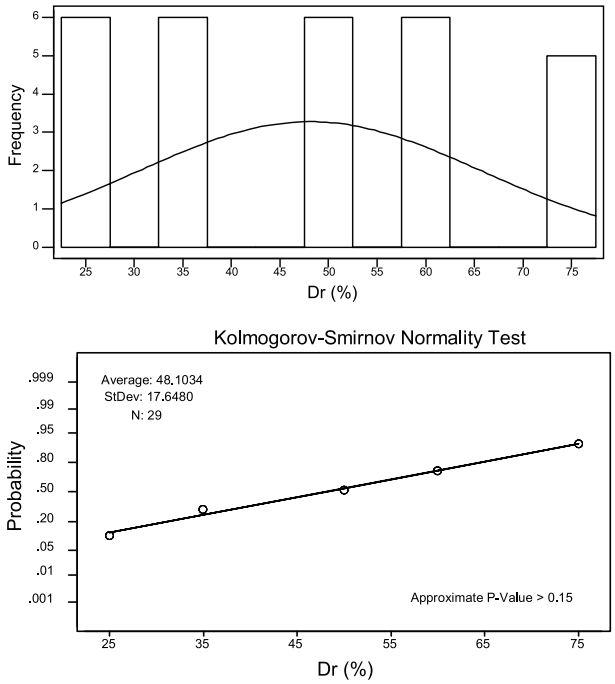

Figure 8. Normal distribution of the *Dr* shown by (a) histogram of data and (b) the Kolmogorov-Smirnov Normal test.

Also, fig. 9 shows the 95% confidence and prediction bands of the line regression. As can be seen, all the data is limited to the prediction band area.

$$Dr(\%) = -181.18 + 406.38(Logq_d) \quad (R^2=0.96) \qquad (6)$$

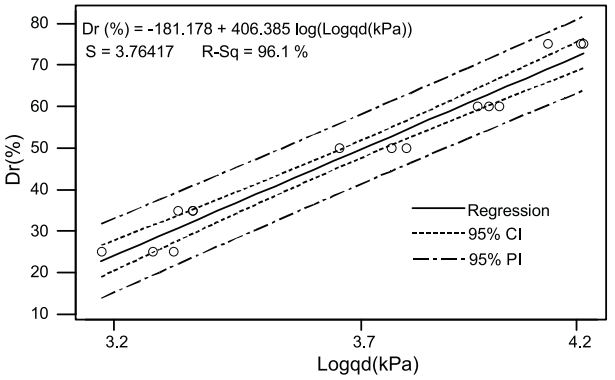

Figure 9. Correlation between q_d index and *Dr*(%).

5.3 q_d versus modulus of elasticity (*E*)

As mentioned previously, the modulus of elasticity (*E*) is a useful parameter in earthworks. To evaluate the Normality of the modulus of elasticity, all the data obtained from the PLTs such as $E_{PLT(i)}$ and $E_{PLT(R2)}$ were tested using the Normal histogram curve and the Normal probability plot of the Kolmogorov-Smirnov test (figs. 10 and12). The results show that $E_{PLT(i)}$ and

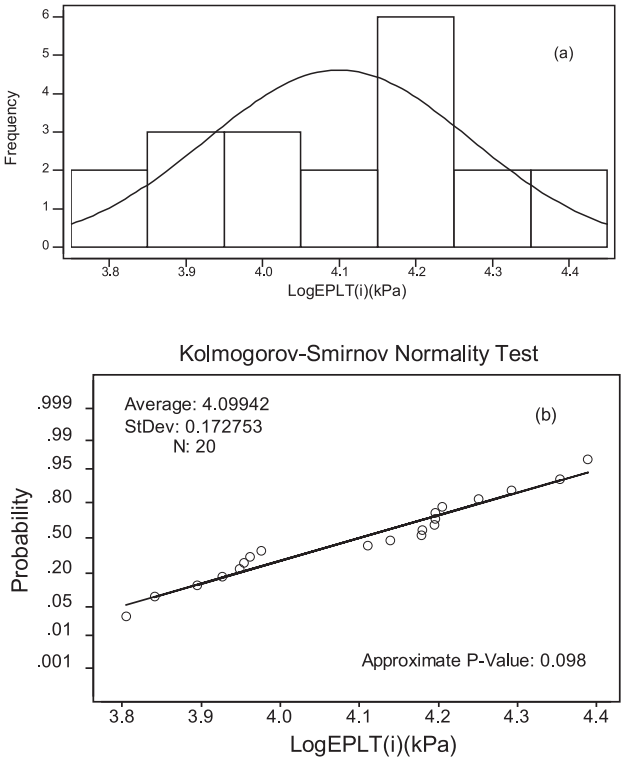

Figure 10. logNormal distribution of the $E_{PLT(i)}$ shown by (a) histogram of data and (b) the Kolmogorov-Smirnov Normal test.

$E_{PLT(R2)}$ are according to the logNormal and Normal functions, respectively. For the data obtained in this study, the best correlations between the average q_d, $E_{PLT(i)}$ and $E_{PLT(R2)}$ are presented in fig. 11 and 13 (Eqs. 7 and 8). However, there is a better correlation (Eq.8) between the average q_d index and the PLT reloading modulus ($E_{PLT(R2)}$) compared to the correlation with $E_{PLT(i)}$. Also, all the data and the regression lines are limited at the 95% confidence and prediction limits, respectively.

$$LogE_{PLT(i)}(kPa) = 2.50 + 0.43Logq_d \quad (R^2=0.90) \qquad (7)$$

$$E_{PLT(R2)}(kPa) = -33870.5 + 11407.1Logq_d \quad (R^2=0.96) \quad (8)$$

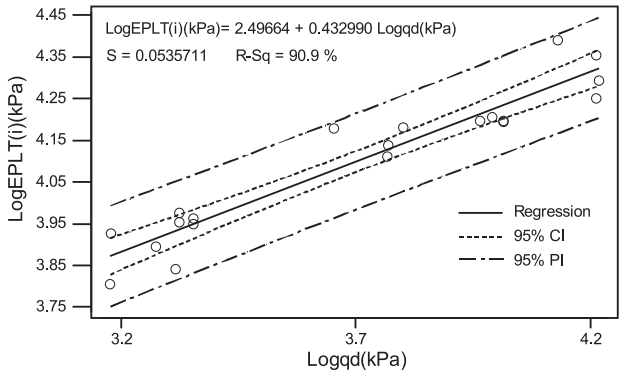

Figure 11. Correlation between q_d and $E_{PLT(i)}$.

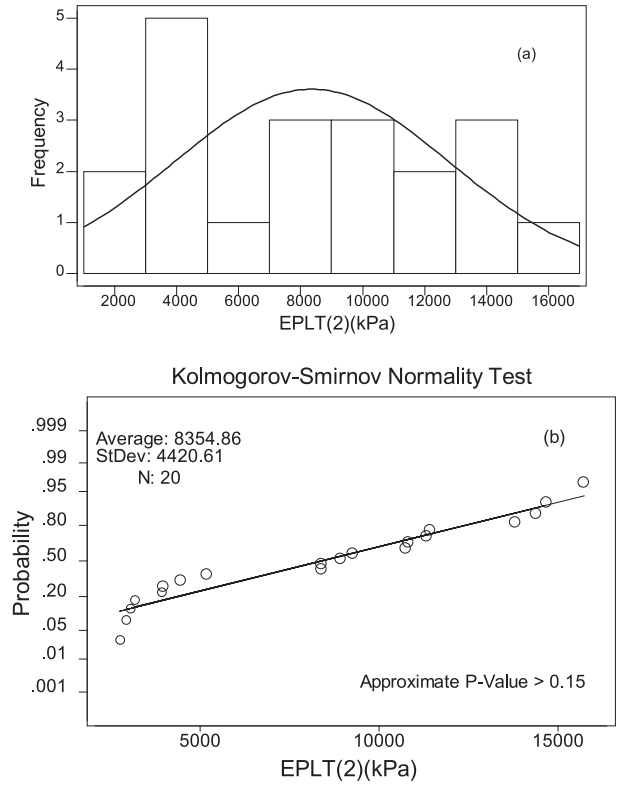

Figure 12. Normal distribution of the $E_{PLT(R2)}$ shown by (a) histogram of data and (b) the Kolmogorov-Smirnov Normal test.

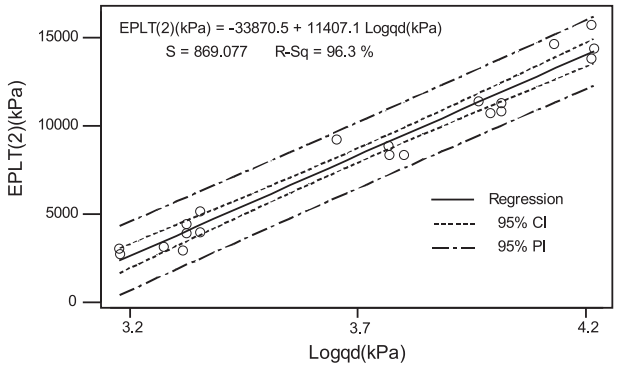

Figure 13. Correlation between q_d index and $E_{PLT(R2)}$.

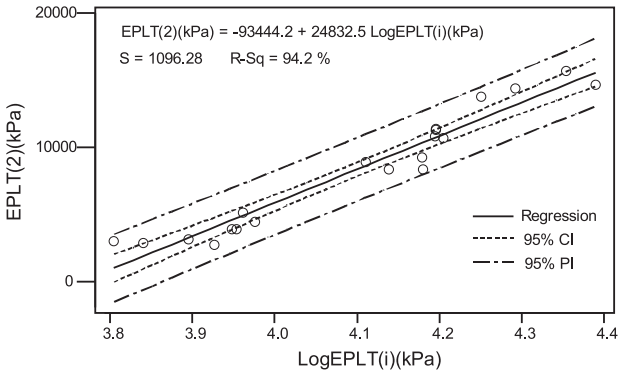

Figure 14. Correlation between $E_{PLT(i)}$ and $E_{PLT(R2)}$.

Fig. 14 and Eq. (9) show the correlation between $E_{PLT(i)}$ and $E_{PLT(R2)}$, which has a linear trend.

$$E_{PLT(R_2)}(kPa) = -93444.2 + 24832.5 LogE_{PLT(i)}(kPa) \quad (R^2=0.94) \qquad (9)$$

5.4 q_d versus shear modulus (G)

Several methods are available to evaluate the shear modulus of coarse-grained and fine grained soils, such as geophysical methods, the Plate Load Test (PLT), etc., which are all costly. In this research, the PLT shear modulus (G_{PLT}) of the studied sandy soil was determined. Like the sandy soils' modulus of elasticity ($E_{PLT(i)}$) obtained in the present research, the G_{PLT} values were according to the logNormal function (figs 15a and 15b). Several correlations between the average q_d versus G_{PLT} were investigated. The best correlation between the average q_d and (G_{PLT}) is presented in fig. 16 and Eq (10). All the data and regression lines are located at the 95% confidence and prediction limits, respectively. The results show that the shear modulus increases with an increase in the values of q_d. This correlation is linear with a determination coefficient of 0.92.

$$LogG_{PLT}(kPa) = 0.39 + 0.897 Logq_d \quad (R^2=0.92) \qquad (10)$$

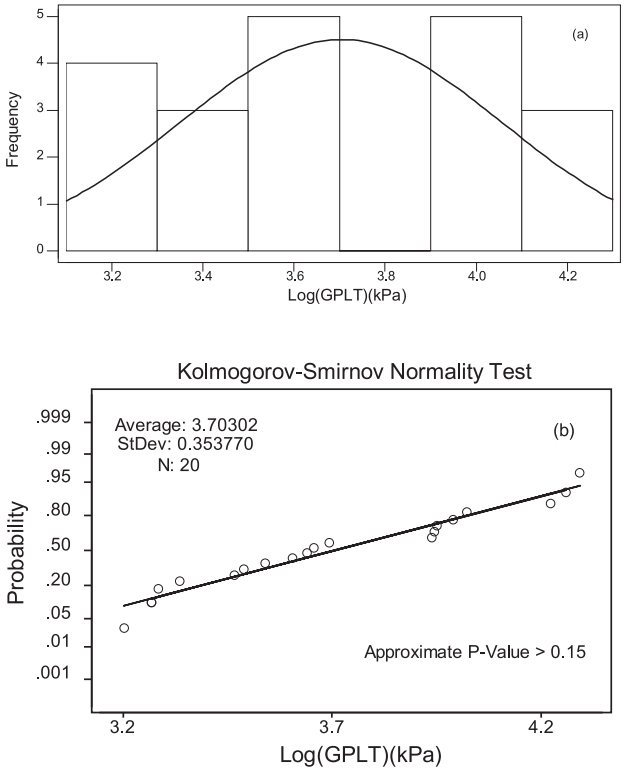

Figure 15. logNormal distribution of the G_{PLT} shown by (a) histogram of data and (b) the Kolmogorov-Smirnov Normal test.

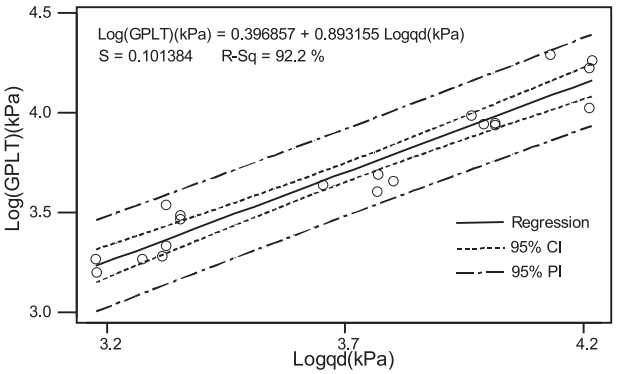

Figure 16. Correlation between q_d index and G_{PLT}.

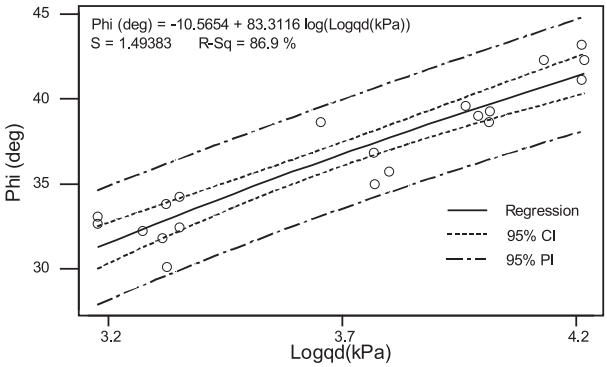

Figure 18. Correlation between q_d index and friction angle (ϕ).

5.5 q_d versus friction angle

The friction angle (ϕ) of sandy soils is an important engineering parameter for the design of the earth structure in earthworks. To assess the Normality of the effective friction angles (ϕ) obtained in the present research, the Normal histogram curve and the Normal probability plot of a Kolmogorov-Smirnov test were used (figs. 17a and17b). The results show that the effective friction angle (ϕ) is according to the Normal function.

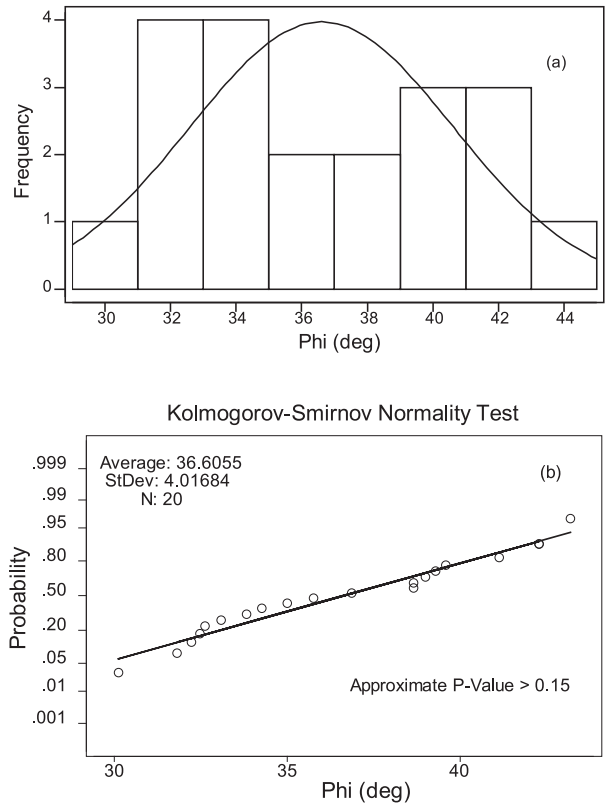

Figure 17. Normal distribution of the friction angle (ϕ) shown by (a) histogram of data and (b) the Kolmogorov-Smirnov Normal test.

The correlation between the average q_d and effective friction angle (ϕ) is presented in Fig. 18 and Eq. (11):

$$Phi(Deg) = -10.56 + 83.31Log(Logq_d) \quad (R^2=0.87) \quad (11)$$

6 SUMMARY AND CONCLUSIONS

The PSP is a lightweight device that can be conveniently used for soil investigations in shallow depths. The results of PSP testing can be used to assess rapidly the variability of soil conditions, allowing different layers to be identified. Based on the results of the present research, correlations can be established between the q_d index and the engineering parameters of sandy soils. A statistical approach was applied to find the best correlations of the results with a high coefficient of determination (R^2). For the results obtained, the determination coefficients (R^2) between q_d and the engineering parameters were mostly greater than 0.90. The statistical methods indicated that the distribution of the data obtained from the PSP was according to logNormal function and the obtained experimental formulas were located in semi-logarithmic and logarithmic classes. Also, all the data and regression lines were located at the 95% confidence and prediction bands, respectively. Table 6 shows the summary of the equations obtained in this study. To control the repeatability of the results of the PSP tests, the values of the coefficient of variation (*COV*) were calculated. This coefficient varied between 0 and 28.3%. Therefore, it can be concluded that the results of the PSP tests for five relative densities (*Dr*) can be considered as repeatable when compared with the values presented by Lee [13].

REFERENCES

[1] Palmer, D.J., Stewart, J.G. 1957. Some observations on the Standard Penetration Test and a correlation of the Test with a new Penetrometer. Proc. 4th Int.

Table 6. Summary of developed equations in this paper.

Parameters	Correlation Type	Equations	Determination Coefficient (R^2)
Dr - q_d	Semi-Logarithmic	$Dr(\%) = -181.18 + 406.38(Logq_d)$	0.96
EPLT(i) - q_d	Logarithmic	$LogE_{PLT(i)}(kPa) = 2.50 + 0.43Logq_d$	0.90
EPLT(R2) - q_d	Semi-Logarithmic	$E_{PLT(R2)}(kPa) = -338705 + 114071Logq_d$	0.96
EPLT(i)-EPLT(R2)	Semi-Logarithmic	$E_{PLT(R_2)}(kPa) = -934442 + 248325LogE_{PLT(I)}(kPa)$	0.94
GPLT - q_d	Logarithmic	$LogG_{PLT}(kPa) = 0.39 + 0.897Logq_d$	0.92
ϕ' - q_d	Semi-Logarithmic	$Phi(Deg) = -10.56 + 83.31Log(Logq_d)$	0.87

Conf. on Soil Mechanics and Foundation Engineering, London, 1, 231–236.

[2] Mohammadi, S.D., Fityus, S.G., Bates, L. 2012. Calibration of the Perth Sand Penetrometer (PSP) for Silica Sands. Iranian journal of Sciences and Technology, Transaction Civil Engineering, 36,13-23.

[3] Sawangsuriya, A., Edil, T.B. 2005. Evaluating stiffness and strength of pavement materials. Geotechnical Engineering, 157, 217-230.

[4] AS1289.F3.3. 1984. Determination of the penetration resistance of a soil with a Perth Sand Penetrometer. Standards Association of Australia.

[5] Fakher, A., Khodaparast, M., Jones, CJFP. 2006. The use of the Mackintosh Probe for site investigation in soft soils. Quarterly Journal Engineering Geology and Hydrology 39, 189–196.

[6] Lee, C., Kim, K.S., Woo, W., Lee, W. 2014. Soil Stiffness Gauge (SSG) and Dynamic Cone Penetrometer (DCP) tests for estimating engineering properties of weathered sandy soils in Korea. Engineering Geology 169, 91–99.

[7] Mohammadi, S.D., Nikudel, M.R., Rahimi, H., Khamehchiyan, M. 2008. Application of the Dynamic Cone Penetrometer (DCP) for determination of the engineering parameters of sandy soils. Engineering Geology 101, 195–203.

[8] Mohammadi, S.D., Nikudel, M.R., Rahimi, H., Khamehchiyan, M. 2012. Unit Skin Friction from the Extended Dynamic Cone Penetrometer (EDCP) Test Supplemented by Measurement of Torque within testing wells. Iranian Journal of Sciences and Technology Transaction Civil Engineering 36, 115-119.

[9] Mohammadi, S.D., Nikudel, M.R., Rahimi, H. 2009. Assesment of the effect of DCP tip angle on its results repeatability. Journal of Iranian Association of Engineering Geology 1, 2, 31-41 (in Persian).

[10] Baecher, B.G., Christian, J.T. 2003. Reliability and statistics in geotechnical engineering. John Wiley & Sons Ltd, England.

[11] Esmailian, M. 2006. SPSS 14 guide book. Tehran Dibagaran, Tehran, Iran (in Persian).

[12] Khodaparast, M. 2006. Expanding of soil geotechnical identification techniques using Dynamic probes. Dissertation, Tehran University, (in Persian).

[13] Lee, I.K., White, W., Ingles, O.G. 1983. Geotechnical Engineering. Copp Clark Pitman; Incorporated.

[14] Abu-farsakh, M., Khalid Alshibi, P.E., Nazzal, M., Seyman, E. 2004. Assessment of in-situ test technology for construction control of base courses and embankments. Report No, FHWA/LA.04/385, Louisiana Transportation Research Center.

[15] Bowles, J.E. 1997. Foundation analysis an design. 5th edition, McGraw-Hill International Editions.

[16] ASTM 1998. Standard test method for repetitive static plate load tests of soils and flexible pavement components, for use in evaluation and design of airport and highway pavements (D1195-93). Annual Book of ASTM Standards 04.08, pp. 110-113.

[17] Timoshenko, S.P., Goodier, J.N. 1970. Theory of Elasticity. 3rd Edition, Mc Graw-Hill Book company, New York.

[18] American Society of Testing and Materials. 2000. Standard test method for direct shear test of under drained conditions (D3080-98). Annual book of ASTM standards 04.08, pp. 894-904.

[19] Coduto, P.D. 2004. Foundation design, principal and practices. Second Edition, Prentice Hall, New Jersey.

NAVODILA AVTORJEM

Vsebina članka

Članek naj bo napisan v naslednji obliki:

- Naslov, ki primerno opisuje vsebino članka in ne presega 80 znakov.
- Izvleček, ki naj bo skrajšana oblika članka in naj ne presega 250 besed. Izvleček mora vsebovati osnove, jedro in cilje raziskave, uporabljeno metodologijo dela, povzetek izidov in osnovne sklepe.
- Največ 6 ključnih besed, ki bi morale biti napisane takoj po izvlečku.
- Uvod, v katerem naj bo pregled novejšega stanja in zadostne informacije za razumevanje ter pregled izidov dela, predstavljenih v članku.
- Teorija.
- Eksperimentalni del, ki naj vsebuje podatke o postavitvi preiskusa in metode, uporabljene pri pridobitvi izidov.
- Izidi, ki naj bodo jasno prikazani, po potrebi v obliki slik in preglednic.
- Razprava, v kateri naj bodo prikazane povezave in posplošitve, uporabljene za pridobitev izidov. Prikazana naj bo tudi pomembnost izidov in primerjava s poprej objavljenimi deli.
- Sklepi, v katerih naj bo prikazan en ali več sklepov, ki izhajajo iz izidov in razprave.
- Vse navedbe v besedilu morajo biti na koncu zbrane v seznamu literature, in obratno.

Dodatne zahteve

- Vrstice morajo biti zaporedno oštevilčene.
- Predložen članek ne sme imeti več kot 18 strani (brez tabel, legend in literature); velikost črk 12, dvojni razmik med vrsticami. V članek je lahko vključenih največ 10 slik. Isti rezultati so lahko prikazani v tabelah ali na slikah, ne pa na oba načina.
- Potrebno je priložiti imena, naslove in elektronske naslove štirih potencialnih recenzentov članka. Urednik ima izključno pravico do odločitve, ali bo te predloge upošteval.

Enote in okrajšave

V besedilu, preglednicah in slikah uporabljajte le standardne označbe in okrajšave SI. Simbole fizikalnih veličin v besedilu pišite poševno (npr. *v*, *T* itn.). Simbole enot, ki so sestavljene iz črk, pa pokončno (npr. Pa, m itn.). Vse okrajšave naj bodo, ko se prvič pojavijo, izpisane v celoti.

Slike

Slike morajo biti zaporedno oštevilčene in označene, v besedilu in podnaslovu, kot sl. 1, sl. 2 itn. Posnete naj bodo v katerem koli od razširjenih formatov, npr. BMP, JPG, GIF. Za pripravo diagramov in risb priporočamo CDR format (CorelDraw), saj so slike v njem vektorske in jih lahko pri končni obdelavi preprosto povečujemo ali pomanjšujemo.

Pri označevanju osi v diagramih, kadar je le mogoče, uporabite označbe veličin (npr. *v*, *T* itn.). V diagramih z več krivuljami mora biti vsaka krivulja označena. Pomen oznake mora biti razložen v podnapisu slike.

Za vse slike po fotografskih posnetkih je treba priložiti izvirne fotografije ali kakovostno narejen posnetek.

Preglednice

Preglednice morajo biti zaporedno oštevilčene in označene, v besedilu in podnaslovu, kot preglednica 1, preglednica 2 itn. V preglednicah ne uporabljajte izpisanih imen veličin, ampak samo ustrezne simbole. K fizikalnim količinam, npr. *t* (pisano poševno), pripišite enote (pisano pokončno) v novo vrsto brez oklepajev. Vse opombe naj bodo označene z uporabo dvignjene številke[1].

Seznam literature

Navedba v besedilu

Vsaka navedba, na katero se sklicujete v besedilu, mora biti v seznamu literature (in obratno). Neobjavljeni rezultati in osebne komunikacije se ne priporočajo v seznamu literature, navedejo pa se lahko v besedilu, če je nujno potrebno.

Oblika navajanja literature

V besedilu: Navedite reference zaporedno po številkah v oglatih oklepajih v skladu z besedilom. Dejanski avtorji so lahko navedeni, vendar mora obvezno biti podana referenčna številka.

Primer: »..... kot je razvidno [1,2]. Brandl and Blovsky [4], sta pridobila drugačen rezultat…«

V seznamu: Literaturni viri so oštevilčeni po vrstnem redu, kakor se pojavijo v članku. Označimo jih s številkami v oglatih oklepajih.

Sklicevanje na objave v revijah:

[1] Jelušič, P., Žlender, B. 2013. Soil-nail wall stability analysis using ANFIS. Acta Geotechnica Slovenica 10(1), 61-73.

Sklicevanje na knjigo:
[2] Šuklje, L. 1969. Rheological aspects of soil mechanics. Wiley-Interscience, London
Sklicevanje na poglavje v monografiji:
[3] Mitchel, J.K. 1992. Characteristics and mechanisms of clay creep and creep rupture, in N. Guven, R.M. Pollastro (eds.), Clay-Water Interface and Its Rheological Implications, CMS Workshop Lectures, Vol. 4, The clay minerals Society, USA, pp. 212-244..
Sklicevanje na objave v zbornikih konferenc:
[4] Brandl, H., Blovsky, S. 2005. Slope stabilization with socket walls using the observational method. Proc. Int. conf. on Soil Mechanics and Geotechnical Engineering, Bratislava, pp. 2485-2488.
Sklicevanje na spletne objave:
[5] Kot najmanj, je potrebno podati celoten URL. Če so poznani drugi podatki (DOI, imena avtorjev, datumi, sklicevanje na izvorno literaturo), se naj prav tako dodajo.

Podatki o avtorjih

Članku priložite tudi podatke o avtorjih: imena, nazive, popolne poštne naslove, številke telefona in faksa, naslove elektronske pošte. Navedite kontaktno osebo.

Sprejem člankov in avtorske pravlce

Uredništvo si pridržuje pravico do odločanja o sprejemu članka za objavo, strokovno oceno mednarodnih recenzentov in morebitnem predlogu za krajšanje ali izpopolnitev ter terminološke in jezikovne korekture. Z objavo preidejo avtorske pravice na revijo ACTA GEOTECHNICA SLOVENICA. Pri morebitnih kasnejših objavah mora biti AGS navedena kot vir.

Vsa nadaljnja pojasnila daje:

Uredništvo
ACTA GEOTECHNICA SLOVENICA
Univerza v Mariboru,
Fakulteta za gradbeništvo, prometno inženirstvo in arhitekturo
Smetanova ulica 17, 2000 Maribor, Slovenija
E-pošta: ags@uni-mb.si

INSTRUCTIONS FOR AUTHORS

Format of the paper

The paper should have the following structure:

- A Title, which adequately describes the content of the paper and should not exceed 80 characters;
- An Abstract, which should be viewed as a mini version of the paper and should not exceed 250 words. The Abstract should state the principal objectives and the scope of the investigation and the methodology employed; it should also summarise the results and state the principal conclusions;
- Immediately after the abstract, provide a maximum of 6 keywords;
- An Introduction, which should provide a review of recent literature and sufficient background information to allow the results of the paper to be understood and evaluated;
- A Theoretical section;
- An Experimental section, which should provide details of the experimental set-up and the methods used to obtain the results;
- A Results section, which should clearly and concisely present the data, using figures and tables where appropriate;
- A Discussion section, which should describe the relationships shown and the generalisations made possible by the results and discuss the significance of the results, making comparisons with previously published work;
- Conclusions, which should present one or more conclusions that have been drawn from the results and subsequent discussion;
- A list of References, which comprises all the references cited in the text, and vice versa.

Additional Requirements for Manuscripts

- Use double line-spacing.
- Insert continuous line numbering.
- The submitted text of Research Papers should cover no more than 18 pages (without Tables, Legends, and References, style: font size 12, double line spacing). The number of illustrations should not exceed 10. Results may be shown in tables or figures, but not in both of them.
- Please submit, with the manuscript, the names, addresses and e-mail addresses of four potential referees. Note that the editor retains the sole right to decide whether or not the suggested reviewers are used.

Units and abbreviations

Only standard SI symbols and abbreviations should be used in the text, tables and figures. Symbols for physical quantities in the text should be written in Italics (e.g. *v*, *T*, etc.). Symbols for units that consist of letters should

be in plain text (e.g. Pa, m, etc.).
All abbreviations should be spelt out in full on first appearance.

Figures

Figures must be cited in consecutive numerical order in the text and referred to in both the text and the caption as Fig. 1, Fig. 2, etc. Figures may be saved in any common format, e.g. BMP, JPG, GIF. However, the use of CDR format (CorelDraw) is recommended for graphs and line drawings, since vector images can be easily reduced or enlarged during final processing of the paper.

When labelling axes, physical quantities (e.g. *v*, *T*, etc.) should be used whenever possible. Multi-curve graphs should have individual curves marked with a symbol; the meaning of the symbol should be explained in the figure caption. Good quality black-and-white photographs or scanned images should be supplied for the illustrations.

Tables

Tables must be cited in consecutive numerical order in the text and referred to in both the text and the caption as Table 1, Table 2, etc. The use of names for quantities in tables should be avoided if possible: corresponding symbols are preferred. In addition to the physical quantity, e.g. *t* (in Italics), units (normal text), should be added on a new line without brackets.
Any footnotes should be indicated by the use of the superscript[1].

LIST OF references

Citation in text

Please ensure that every reference cited in the text is also present in the reference list (and vice versa). Any references cited in the abstract must be given in full. Unpublished results and personal communications are not recommended in the reference list, but may be mentioned in the text, if necessary.

Reference style

Text: Indicate references by number(s) in square brackets consecutively in line with the text. The actual authors can be referred to, but the reference number(s) must always be given:

Example: "... as demonstrated [1,2]. Brandl and Blovsky [4] obtained a different result ..."

List: Number the references (numbers in square brackets) in the list in the order in which they appear in the text.

Reference to a journal publication:
[1] Jelušič, P., Žlender, B. 2013. Soil-nail wall stability analysis using ANFIS. Acta Geotechnica Slovenica 10(1), 61-73.

Reference to a book:
[2] Šuklje, L. 1969. Rheological aspects of soil mechanics. Wiley-Interscience, London

Reference to a chapter in an edited book:
[3] Mitchel, J.K. 1992. Characteristics and mechanisms of clay creep and creep rupture, in N. Guven, R.M. Pollastro (eds.), Clay-Water Interface and Its Rheological Implications, CMS Workshop Lectures, Vol. 4, The clay minerals Society, USA, pp. 212-244.

Conference proceedings:
[4] Brandl, H., Blovsky, S. 2005. Slope stabilization with socket walls using the observational method. Proc. Int. conf. on Soil Mechanics and Geotechnical Engineering, Bratislava, pp. 2485-2488.

Web references:
[5] As a minimum, the full URL should be given and the date when the reference was last accessed. Any further information, if known (DOI, author names, dates, reference to a source publication, etc.), should also be given.

Author information

The following information about the authors should be enclosed with the paper: names, complete postal addresses, telephone and fax numbers and E-mail addresses. Indicate the name of the corresponding author.

Acceptance of papers and copyright

The Editorial Committee of the Slovenian Geotechnical Review reserves the right to decide whether a paper is acceptable for publication, to obtain peer reviews for the submitted papers, and if necessary, to require changes in the content, length or language.
On publication, copyright for the paper shall pass to the ACTA GEOTECHNICA SLOVENICA. The AGS must be stated as a source in all later publication.

For further information contact:

Editorial Board
ACTA GEOTECHNICA SLOVENICA
University of Maribor,
Faculty of Civil Engineering, Transportation Engineering and Architecture
Smetanova ulica 17, 2000 Maribor, Slovenia
E-mail: ags@uni-mb.si

NAMEN REVIJE

Namen revije ACTA GEOTECHNICA SLOVENICA je objavljanje kakovostnih teoretičnih člankov z novih pomembnih področij geomehanike in geotehnike, ki bodo dolgoročno vplivali na temeljne in praktične vidike teh področij.

ACTA GEOTECHNICA SLOVENICA objavlja članke s področij: mehanika zemljin in kamnin, inženirska geologija, okoljska geotehnika, geosintetika, geotehnične konstrukcije, numerične in analitične metode, računalniško modeliranje, optimizacija geotehničnih konstrukcij, terenske in laboratorijske preiskave.

Revija redno izhaja dvakrat letno.

AIMS AND SCOPE

ACTA GEOTECHNICA SLOVENICA aims to play an important role in publishing high-quality, theoretical papers from important and emerging areas that will have a lasting impact on fundamental and practical aspects of geomechanics and geotechnical engineering.

ACTA GEOTECHNICA SLOVENICA publishes papers from the following areas: soil and rock mechanics, engineering geology, environmental geotechnics, geosynthetic, geotechnical structures, numerical and analytical methods, computer modelling, optimization of geotechnical structures, field and laboratory testing.

The journal is published twice a year.

AVTORSKE PRAVICE

COPYRIGHT

ODGOVORNOST

RESPONSIBILITY

www.fg.um.si

www.sloged.si

Univerza v Ljubljani

Fakulteta za gradbeništvo in geodezijo

Naravoslovnotehniška Fakulteta

www.fgg.uni-lj.si
www.ntf.uni-lj.si

www.ita-slovenia.si